

Transport variability-driving mechanisms in Flemish Pass at the western boundary of the Subpolar North Atlantic

Eirini Varotsou

Dissertation with the aim of achieving a doctoral degree at the Faculty of
Mathematics, Informatics and Natural Sciences
Department of Earth Science
University of Hamburg

January, 2016

Dissertation accepted by
the Department of Earth Science, University of Hamburg
under the Exam committee of:
Prof. Dr. Detlef Quadfasel
Dr. Kerstin Jochumsen

Hamburg, 29 April 2016

Final version

I hereby declare, on oath, that I have written the present dissertation on my own and have not used other than the acknowledged resources and aids.

Hamburg, 27.01.16

Eirini Varotsou

Acknowledgements

This thesis is the result of a series of interactions with different people, each of whom has played an important role in its development. Therefore, I would like to devote this page to sincerely thank these individuals for their assistance.

Firstly, I would like to express my sincere gratitude to my supervisor Dr. Kerstin Jochumsen for the continuous and unreserved support at my PhD study. Her guidance helped me throughout the research and writing of this thesis especially during the writing process she was always there to support me and help me adjust to the new circumstances.

Besides my supervisor I would like to sincerely thank Prof. Dr. Detlef Quadfasel for his support and confidence in my efforts.

My sincere thanks also goes to Dr. Nuno Serra for his support and guidance at my PhD study.

I also thank Dr. Dagmar Kieke and Linn Schneider from the University of Bremen for the excellent cooperation we have had.

I also thank Dr. Stavroula Biri for her contribution both at scientific and friendly assistance.

Moreover, I have to mention how grateful I feel to my colleagues in the department and to my new and old friends.

Last but not least, I would like to thank my family: Vasili, Alexandra, Kosta, Maria, and Alexandra who, in spite of being away, support me spiritually throughout this thesis and my life in general.

This research was funded by the German DFG project FLEPVAR (GZ JO809/2-1 and KI 1655/1-1).

Abstract

The aim of this study is to analyse the Upper Labrador Sea Water (ULSW) volume transport variability at Flemish Pass and in the Deep Western Boundary Current (DWBC) at 47°N and at 53°N along the topographic slope of the Continental Shelf at the Grand Banks of Newfoundland. In the focus of this study are the physical mechanisms governing the transport variability of ULSW at various timescales using monthly (from 1960-2009) and daily (from 2003-2009) model data from an 8-km resolution numerical ocean model (MITgcm).

In order to quantify the southward ULSW volume transport, the modeled monthly outputs were used. The average model transport of ULSW decreases southwards from 6.7 Sv at 53°N to 4.5 Sv at 45°N due to interior pathways in the Labrador Sea and in the Newfoundland Basin. The largest fraction of the total ULSW volume transport goes around Flemish Cap within the Deep Western Boundary Current (70%) but a significant part goes through Flemish Pass (20%). At seasonal and interannual timescales, the temporal evolution of the ULSW volume transport variability at Flemish Pass presents a distinct behavior when compared to the variability in the DWBC at 47°N and to the upstream fluctuations at 53°N . Other physical parameters are taken into consideration for the examination of the behavior of the transport variability at Flemish Pass. These parameters include the North Atlantic Oscillation (NAO) index, the local Ekman transport, the rate of ULSW formation in the Labrador Sea, the position of the North Atlantic Current (NAC) relative to the slope and the averaged transport in the subpolar gyre. The relationship between these physical processes and the ULSW transports at each section is tested using a running correlation method. Weakened or strengthened transport of ULSW through Flemish Pass coincides with the effect either of the local atmospheric forcing or of changes of the NAC's position. The transport variability in the DWBC at 47°N is caused by upstream flow fluctuations and changes in the rate of

ULSW formation.

At high frequencies for periods of $T \leq 25$ days, the behavior of the ULSW volume transport along the topographic slope between 53°N and 47°N is examined by using the daily model outputs. The presence of the dominant peaks of energy at 24 and 11 days in the Flemish Pass transport of ULSW is likely due to a propagating signal of coastal trapped waves along the topographic slope. The perturbation of the ULSW volume transport signal appears strong close to the topographic slope and decays offshore.

Zusammenfassung

Das Ziel dieser Arbeit ist es, die Variabilität des Volumentransports von Oberem Labradorseewasser (ULSW) in der Flämischen Passage und im tiefen westlichen Randstrom (DWBC) bei 47°N und 53°N am Kontinentalabhang entlang der Grand Banks von Neufundland zu untersuchen. Im Fokus dieser Arbeit sind die physikalischen Mechanismen, die verantwortlich sind für die Transportvariabilität von ULSW auf verschiedenen Zeitskalen. Diese werden mit monatlichen (1960-2009) und täglichen (2003-2009) Modelldaten aus einem 8 km Ozeanmodell (MITgcm) untersucht.

Um den südwärtigen ULSW Volumentransport zu quantifizieren, wurden die modellierten monatlichen Modellfelder verwendet. Der durchschnittliche Modelltransport von ULSW verringert sich von 6,7 Sv bei 53°N auf 4,5 Sv bei 45°N durch interne Ausbreitungspfade in der Labradorsee und im Neufundland Becken. Der größte Anteil des gesamten ULSW Volumentransports geht um die Flämische Kappe im tiefen westlichen Randstrom (70%), aber ein erheblicher Teil strömt auch durch die Flämische Passage (20%). Auf saisonalen und jährlichen Zeitskalen zeigt der ULSW Volumentransport in der Flämischen Passage eine andere Variabilität im Vergleich zur Variabilität im DWBC bei 47°N und zu den stromaufwärts beobachteten Schwankungen bei 53°N . Andere physikalische Parameter werden in Betracht gezogen, um das Verhalten der Transportvariabilität in der Flämischen Passage zu erklären. Diese Parameter umfassen die Nordatlantische Oszillation (NAO Index), den lokalen Ekman Transport, die Rate der ULSW Bildung in der Labradorsee, die Position des Nordatlantikstroms (NAC) in Bezug auf den Kontinentalabhang und den gemittelten Transport im Subpolarwirbel. Die Beziehung zwischen diesen physikalischen Prozessen und den ULSW Transporten in jedem untersuchten Schnitt wird unter Verwendung eines Korrelationsverfahrens (running correlation coefficient method) getestet. Schwacher oder starker Transport von ULSW durch die Flämische Passage decken sich mit der Wirkung entweder des lokalen atmosphärischen Antriebs oder Veränderungen der Lage des NAC. Die Transportvariabilität im DWBC bei 47°N wird durch stromaufwärts erzeugte Schwankungen und Änderungen in der Rate der ULSW Bildung verursacht.

Hohen Frequenzen für Perioden von $T \leq 25$ Tagen, die den ULSW Volumentransport entlang des Kontinentalabhangs zwischen 53°N und 47°N

beeinflussen, werden anhand von täglichen Modelldaten untersucht. Die Hauptspitzen von Energie bei 24 und 11 Tagen in der Flämischen Passage im Transport von ULSW entstehen wahrscheinlich durch ein sich ausbreitendes Signal von Küstenwellen (coastal trapped waves) entlang des Kontinentalabhangs . Die Störung des ULSW Volumetransports ist ausgeprägt nahe des Kontinentalabhangs und verschwindet mit grösserem Abstand zum Hang.

Contents

Contents	vii
List of Figures	ix
List of Tables	xvii
1 Introduction	1
1.1 Ocean- a part of the Earth system	1
1.2 Topographic setting of the North Atlantic	5
1.3 Circulation in the Subpolar North Atlantic region and water mass formation	6
1.3.1 Surface circulation	6
1.3.2 Water masses of the Subpolar North Atlantic	9
1.3.3 Deep circulation in the Subpolar North Atlantic region	11
1.4 Scientific background of the circulation around the Flemish Cap region .	12
1.5 Outline of the thesis	14
2 Data and Methodology	17
2.1 MITgcm model	17
2.2 Model validation	18
2.3 Methodology and Outputs	23
2.3.1 Parameters representing forcing mechanisms	23
2.4 Statistical analysis	26
2.4.1 Power spectral density and statistical significance	26
2.4.2 Running correlation coefficient and statistical significance	26
3 General circulation of the study region	29
3.1 Circulation of the ULSW transport in the study region	29

CONTENTS

3.2	Transport variability of the volume transport and its spectral analysis	33
3.3	Seasonal cycle	36
4	Changes of the transport variability in the surface layer and in the layer thickness variability	43
4.1	Volume transport variability in the surface layer at interannual timescale	44
4.2	Relationship between the ULSW layer thickness variability and the ULSW volume transport variability at interannual timescale	50
5	Estimation of the ULSW volume transport	57
5.1	ULSW volume transport variability	57
5.2	Causes of the temporal variability of the ULSW transports at 47°N	60
5.3	Processes responsible for ULSW transport variability at Flemish Pass	67
5.4	Processes responsible for ULSW transport variability in the DWBC at 47°N	68
5.5	Residual ULSW transport variability at 47°N	68
6	High frequency variability	73
6.1	Power spectral density of the studied parameters	73
6.2	Basic Characteristics of the coastal trapped waves	77
6.2.1	Investigating the propagating signal at the topographic slope of the Continental shelf at the Grand Banks	78
7	Conclusions	87
7.1	Summary and discussion	87
7.2	Further investigation	91
	Bibliography	93

List of Figures

1.1	Map showing an overview of the circulation in the Nordic Seas and subpolar basins. The flow of the surface currents (solid curves) and deep currents (dashed curves) is presented. Colors of curves follow the temperatures. Source: R. Curry, Woods Hole Oceanographic Institution/Science/ USGRP.	3
1.2	Estimates of AMOC transport at various latitudes in the North Atlantic from observations and model assimilations [Bullister et al., 2013]	5
1.3	Circulation of main water masses in the subpolar North Atlantic. White: LSW, White hatched areas named C: Convection areas where formation of UNADW (LSW) could occur, blue: ISOW and DSOW, red North Atlantic Current NAC (upper 500m). The NAC is included since its strong currents could reach down to the bottom and carry deep and bottom water [Bullister et al., 2013].	8
1.4	a) Evaluation of LSW in the Labrador Sea: a volumetric σ_2 - time plot showing the average thickness (meters) $\Delta\sigma_2 = 0.01kg/m^3$ layers in the Labrador Sea σ_2 is potential density anomaly referenced to 2000 db) ,b) temporal volumetric changes: 1994, 2004 and 2004, volumetric potential temperature (θ)-salinity (S) censuses of the Labrador Sea.c)Spatial distribution of the volumetric changes 1995, volumetric (θ)-(S) censuses of the Labrador, Irminger and Iceland basins. Each value in (b)and (c) represents the average thickness (in meters)of a $0.1^\circ \times 0.01 \Delta\theta \times \Delta\sigma$ layer. The solid and dashed lines are isolines of σ_2 (kg/m^3) defined by θ and S [Yashayaev et al., 2008].	10

LIST OF FIGURES

1.5	Map showing the schematic spreading pathways of Labrador Sea Water (LSW) in the studied region (blue arrows). Red arrows indicate the path of the North Atlantic Current (NAC). Flemish Pass is the passage between Flemish Cap (FC) and the Grand Banks. The convection area in the Labrador Sea is north of the shown region. Isobaths are given every 100 m between 400 m and 1000 m and every 500 m from 1000 m to 3500 m [Varotsou et al., 2015].	12
2.1	Monthly time series of de-seasoned (15-months low pass filtered) net ULSW transport (positive to the south) across 47°N within the DWBC (red) and through Flemish Pass (black) from monthly averaged model results (solid line) and from snapshots observed with lowered Acoustic Doppler Current Profiles (LADCP) (dots). Observational estimates are based on snapshots provided by Schneider et al., [2015].	19
2.2	Time series of ULSW hydrographic properties in Flemish Pass at 47°N based on CTD measurements (red, seasonal cycle removed) and derived from the MITgcm model (black, 15 months low pass filtered). (a) Median potential temperature anomaly ($^{\circ}\text{C}$) and (b) median salinity anomaly relative to the mean of the period 1994 – 2009. Dashed lines indicate trends during the overlapping period 1994 – 2009 of both time series [Schneider et al., 2015].	20
2.3	Vertical section of simulated 1960-2009 time-averaged meridional velocity at 47°N , showing the surface-intensified Labrador Current in the western Flemish Pass (FP), as well as the DWBC east of Flemish Cap. The limits of velocity integration for the ULSW transport computation are illustrated by the mean position of the density interfaces $\sigma_{\theta} = 27.68 \text{ kg/m}^3$ and $\sigma_{\theta} = 27.74 \text{ kg/m}^3$ and the position of the average zero mean velocity above Flemish Cap and east of Flemish Cap (thick black lines) [Varotsou et al., 2015].	21
2.4	Anomalies of temperature observed at mooring K9 from [Fischer et al., 2010](blue line) and the long term simulated temperature anomaly from 1948 to 2012 (red line) at the position $53^{\circ}\text{W}, 53^{\circ}\text{N}$ and at 1500 m depth. The anomalies were calculated relative to the period August 1997-April 2012. Observations were low-passed filtered (cut-off 60 days) and are shown as monthly means.	22

2.5	Monthly de-seasoned time series (low-pass filtered with 15 months cut-off) of parameters corresponding to potential agents responsible for the variability of ULSW transport over the study region: (A) the NAO index; (B) the Ekman transport at 53°N over the slope, at 47°N east of Flemish Cap and at Flemish Pass (an offset of +0.1 Sv was added to the red line for clarity of the subfigure; positive values correspond to southward transport); (C) the rate of the ULSW formation in the sub-polar gyre; (D) the NAC position relative to Flemish Cap; and (E) the subpolar gyre averaged transport. See text for a detailed description of the computation of parameters [Varotsou et al., 2015].	25
3.1	Map showing the magnitude of the vertically integrated volume fluxes in the model ULSW layer (color) and the average downstream volume transports across the shown sections (A-F, white). Isobaths are given from 0 to 4000 m in 400 m intervals as thin black lines in the background [Varotsou et al., 2015].	31
3.2	Sketch showing the inflow and outflow of the ULSW volume transport from the 47°N to 45°N.	32
3.3	Unfiltered volume transport variability A) on the surface layer and B) in the ULSW density layer at the three examined sections	34
3.4	Variance preserving power spectra of monthly transports (unfiltered) in Flemish Pass (A) and at 47°N (B) and at 53°N (C) in surface layer ($\sigma_\theta < 27.68 \text{ kg/m}^3$) obtained by a multi-taper method following Ghil et al. [2002]. The significant peak of energy at the three year period is pointed out by the black arrow and the significance level at 95% by the dotted line.	35
3.5	Same as Figure 3.4 but for the case of the ULSW transport variability (in the density layer $\sigma_\theta = 27.68 - 27.74 \text{ kg/m}^3$).	36
3.6	Average seasonal cycle of the surface layer volume transports (positive to the south) for each section of the three model sections highlighted in Figure 3.1 and computed over the period 1960-2009.	37
3.7	Average seasonal cycle of the model's Ekman transport (positive to the south) for each of the three sections over the period 1960-2009.	38
3.8	Same as Figure 3.6 but for the case of the ULSW transport variability in the density layer ($\sigma_\theta = 27.68 - 27.74 \text{ kg/m}^3$).	39

LIST OF FIGURES

3.9 Average seasonal cycle of the ULSW volume transports (positive to the south) (A) with constant layer thickness and (B) with constant velocity for each section over the period 1960-2009. 41

4.1 Band-pass filtered (from 18 to 54 months) ULSW transport anomalies at the three selected sections A) at Flemish Pass (black) , B) at 47°N (red) and C) at 53°N (cyan) at the DWBC and the transport anomalies in the surface layer (gray lines) at the same sections. 45

4.2 Coefficients of the running correlation (Cor; black lines) between the band-pass filtered time series of the NAO index, the Ekman transport at Flemish Pass, the subpolar averaged transport and volume transport in surface layer ($\sigma_\theta < 27.68 \text{ kg/m}^3$) at Flemish Pass. Gray lines correspond to running correlations obtained from the bootstrap method (repeated 20 times). The blue ticks are the significance limits of the correlation according to the p-value ($r=0.5$, 95% confidence level) and red boxes mark periods of significant correlations between the tested parameters. 47

4.3 Same as Figure 3.4 but for the case of the volume transport in the surface layer at 47°N. 48

4.4 Band-pass filtered (from 18 to 54 months) ULSW layer thickness anomalies for the sections A, B, C shown in Figure 3.1: at 53°N (cyan), at the DWBC at 47°N (red) and at Flemish Pass (black). 51

4.5 Unfiltered ULSW Volume transports for the Sections A, B, C at 53°N (cyan), in the DWBC at 47°N (red) and at Flemish Pass (black) using only the negative velocity. A) (top of the figure) the volume transport ($T_{vel.}$) using constant layer (from the mean depth of the upper boundary to the mean depth of the low boundary of the ULSW density layer) at each section, B) (in the middle of the figure) the volume transport (T_ρ) using the average velocity and C) (the bottom of the figure) the sum of A+B at each section over the study period. 54

4.6	Band-pass filtered (from 18 to 54 months) of the volume transport anomalies at 53°N (cyan), at 47°N (red) at the DWBC and at Flemish Pass (black). A) (top of the figure) the volume transport ($T_{vel.}$) using constant layer (from the mean depth of the upper boundary to the mean depth of the low boundary of the ULSW density layer) at each section, B) (in the middle of the figure) the volume transport (T_{ρ}) using the average velocity and C) (the bottom of the figure) the sum of A+B at each section over the study period.	55
5.1	Band-pass filtered (from 18 to 54 months) ULSW transport anomalies for the Sections from 53°N (cyan) to 47°N (red) (an offset of +1 Sv, +2 Sv, +3 Sv and +4 Sv was added to the transport anomalies from 53°N to 47°N, respectively) in the DWBC every 2° and at Flemish Pass (black, without adding an offset to the transport anomaly at Flemish Pass). Dashed black lines are the virtual zero line after adding an offset.	58
5.2	Band-pass filtered (from 18 to 54 months) ULSW volume transport anomalies for the Sections A, B, C of Figure 3.1: at 53°N (cyan), in the DWBC at 47°N (red) and at Flemish Pass (black) [Varotsou et al., 2015].	60
5.3	Band-pass filtered time series (18-54 months) of the same parameters shown in Figure 2.5: (A) the NAO index; (B) the Ekman transport at 53°N over the slope, at 47°N east of Flemish Cap and at Flemish Pass (an offset of +0.1 Sv and +0.2 Sv was added to the latter two for clarity of the subfigure; positive values correspond to southward transport); (C) the rate of the ULSW formation in the Labrador Sea; (D) the NAC position relative to Flemish Cap; and (E) the subpolar gyre averaged transport [Varotsou et al., 2015].	61
5.4	Coefficients of the running correlation (Cor; black thick line) between (A) the DWBC band-pass filtered ULSW volume transports at 47°N and at 53°N (the latter lagged by 3 months) and (B) the ULSW transport difference at 47°N minus that at 53°N (the “residual”) and the ULSW transport at Flemish Pass. The grey lines show correlation results from the bootstrap method and the clusters of these depict the areas of non-significant correlation. Blue ticks are the significant correlation limits according to the p-value ($r=0.5$, 95 % confidence level) [Varotsou et al., 2015].	62

LIST OF FIGURES

5.5 Coefficients of the running correlation (Cor; black lines) between the band-pass filtered time series of ULSW volume transport at Flemish Pass and (A) the NAO index, (B) the Ekman transport at Flemish Pass, (C) the rate of ULSW formation in the Labrador Sea (with 5 months lag applied), (D) the NAC’s position relative to the Flemish Cap and (E) the subpolar gyre strength index. Gray lines correspond to running correlations obtained from the bootstrap method (20 times repeated). The blue ticks are the significance limits of the correlation according to the p value ($r=0.5$, 95 % confidence level). Red boxes mark periods of significant correlations between the ULSW transport at Flemish Pass and the tested parameter [Varotsou et al., 2015]. 64

5.6 Same as Figure 5.5 but for the case of the ULSW transport within the DWBC at 47°N [Varotsou et al., 2015]. 65

5.7 Same as Figure 5.5 but for the case of the ULSW transport residual (see text for explanation) within the DWBC at 47°N [Varotsou et al., 2015]. 66

5.8 Difference in the mean eddy kinetic energy between the periods 1983-1995 and 1969-1979 averaged in the layer 200 m – 500 m, showing stronger variability close to the Flemish Cap (FC) in the latter period associated with the North Atlantic Current path closer to the western margin and featuring a more northward penetration. Isobaths are given every 100 m between 400 m and 1000 m and every 500 m from 1000 m to 3500 m [Varotsou et al., 2015]. 70

5.9 Map showing the difference in magnitude of the vertically-integrated volume fluxes in the model ULSW layer between the periods 1983-1995 and 1969-1979. Red colors (positive values) indicate stronger flow in the latter period, while blue colors (negative values) show reduced flow. FC: Flemish Cap [Varotsou et al., 2015]. 71

6.1 Variance preserving power spectra of daily transports (unfiltered) in Flemish Pass (A) and at 47°N (B) and at 53°N (C) in the ULSW density layer obtained by a multi-taper method following Ghil et al. [2002]. The significant peaks of energy at high frequencies are pointed out by the black arrows, the significance level at 95 % by the dotted line. . . . 74

6.2	Variance preserving power spectra of the observed A) V and B) U velocity at the center of the Flemish Pass area ($47^{\circ}12'N/47^{\circ}10'W$ at 908 m depth for one year from July 2012 to May 2013 obtained by a multi-taper method following Ghil et al. [2002]. The significant peaks of energy at the 24 and 11 (considered to V) days and 23 and 10 days (considered to U) are pointed out by the black arrows, the significance level at 95 % by the dotted line.	75
6.3	A computer assisted conception of a shelf wave from Pearche [2011]. The white arrow shows the phase of propagation in the northern hemisphere and the black arrows over the shelf slope indicate the water velocity under the crest.	77
6.4	Exemplary snapshots maps showing the spatial distribution of the filtered ULSW vertically integrated magnitude in the ULSW density layer (using a band-pass filter centred at 24 days) in the DWBC at the topographic slope along the continental shelf at the Grand Banks during the winter period from 16 th to 27 th of January 2006. Isobaths are given from 600 m to 1000 m every 200 m.	79
6.5	Band-pass filtered anomalies (from 22 to 26 days) of the layer thickness (averaged over longitudinal range) in the ULSW density layer latitude vs. time diagram along the topographic slope during the winter period (January-February-March) of each year during the period from 2003 (top) to 2009 (bottom).	81
6.6	Band-pass filtered anomalies (from 22 to 26 days) of the layer thickness (averaged over longitudinal range) in the ULSW density layer latitude vs. time diagram along the topographic slope during the summer period (June-July-August) of each year during the period from 2003 (top) to 2009 (bottom).	82
6.7	a) Velocity (m/s) profile from the shelf to the topographic slope at $52^{\circ}N$ and b) Stratification profile at $52^{\circ}N$	83
6.8	Exemplary snapshot map showing the spatial distribution of the filtered ULSW vertically integrated magnitude in the ULSW density layer (using a band-pass filter centred at 24 days) in the DWBC at the topographic slope at the Grand Banks on January 2005. The wavelength of the propagating signal is the distance difference from the point A to the point B ($53^{\circ}99'N/52^{\circ}15'W$) to ($51^{\circ}78'N/50^{\circ}02'W$).	84

LIST OF FIGURES

6.9	Band-pass filtered anomalies(from 11 to 13 days) of the layer thickness (averaged over longitudinal range) in the ULSW density layer latitude vs. time along the continental shelf slope during the winter period (January-February-March) of each year during he period from 2003(top) to 2009 (bottom).	85
-----	---	----

List of Tables

5.1	Correlation coefficient of the band pass filtered ULSW volume transport anomalies between the selected sections	59
6.1	Mean values and standard deviation of the phase speed along the topographic slope from 53°N to 51°N from the latitude vs. time diagram of the band-pass (centered at 24 days) filtered layer thickness, U velocity and V velocity	83
6.2	Mean (\pm standard deviation) values of the phase speed along the continental slope from 53°N to 51°N from the latitude vs. time diagramm of the filtered (centered at 11 days) layer thickness, U and V velocity. .	86

Chapter 1

Introduction

A scientific interest of this study is focusing on the ocean circulation at the western boundary of the subpolar gyre in the North Atlantic region. The motivation of this study is to show the crucial role of the Flemish Pass region on the circulation at the western subpolar North Atlantic. The goal of the study is to analyse the driving mechanisms of the volume transport variability in the studied region. In the introductory chapter, the role of the ocean as a part of the Earth's system as well as the main components of the ocean circulation in the North Atlantic are presented. A brief description of the topographic features in the North Atlantic and the physical processes and the ocean circulation on the surface and the deep layer in the North Atlantic region is given.

1.1 Ocean- a part of the Earth system

The ocean is an important part in the Earth's climate system due to the large coverage of the planet's surface (approximately 71%) by the ocean water, its high heat capacity (rendering it a large reservoir of heat), and the interaction with the lower boundary of the atmosphere and with the seasonal sea ice cover in high latitudes. During the last decades, the scientific community was mainly focused on the investigation of the ocean circulation using either in situ and remote observations or model simulations on a worldwide scale.

In order to investigate the variability of the climate, the driving mechanisms of the ocean circulation as well as the contribution of the atmosphere to the ocean circulation must be taken into account. Due to the physical processes of deep water formation and deep ocean circulation, the heat and anthropogenic CO_2 are stored in the ocean

1. INTRODUCTION

[Sigman and Boyle, 2000; Russell et al., 2006]. One important region of the world ocean is the North Atlantic, where dense water mass formation takes place. The water mass is a body of the water, which is characterized by specific physiochemical properties. These properties enable us to distinguish each water mass from the surrounding water masses as described for example by Tomczak [1999]. The density of each water mass is defined by its temperature and salinity. The changes of the temperature and salinity are dominated by several physical processes. At the surface layer of the ocean, the changes in temperature are associated with cooling and heating. While sea ice melting, precipitation and river run off reduce salinity, evaporation and sea ice formation increase salinity.

In order to understand the physical processes of deep water formation and the distribution of water masses in the North Atlantic, it's important to mention one of the main components of the circulation in the Atlantic; the Atlantic Meridional Overturning Circulation (AMOC). On a large scale, the water mass spreading is supported by ocean currents. The currents can be classified into the surface currents and the deep currents. These are dominated by several forces. On the surface layer, the currents are mainly forced by the wind (called wind driven currents) and in the deep layers the currents are mainly driven by density changes [Thorpe et al., 2001; Delworth and Dixon 2006]. The AMOC plays a crucial role for the balance of the Earth's climate system, due to the storage and transport of heat from the tropics and the Southern Hemisphere to the North Atlantic (Figure 1.1). Several studies using observations [Talley 2003] or model outputs [Boccaletti et al., 2005; Ferrari and Ferreira, 2011] suggest that 60, % of the northward heat transport in the North Atlantic is caused by the surface component of the AMOC transport.

The AMOC contribution to the heat transport suggests that changes in the global climate system relate to changes in the ocean circulation. The importance and the contribution of the AMOC to the climate have been investigated by several studies. The strength of the AMOC transport is about 18.5 ± 2.5 Sv using observations from the World Ocean Circulation Experiment (WOCE) at 24°N and 16.3 ± 2.7 Sv near to 48°N [Lumpkin and Speer, 2007]. Recently, the AMOC strength and the meridional heat transport at 26°N [McCarthy et al., 2015] have been computed to be about 17.2 Sv and 1.25 PW ($1PW = 10^{15}W$), respectively, by using RAPID observations during the period from April 2004 to October 2012. The heat transport has been estimated at about 0.61 ± 0.13 PW using model outputs at 48°N [Lumpkin and Speer, 2007].

The importance of the AMOC is illustrated by the difference between heat transport in Atlantic and Pacific. The northward heat transport in the Pacific Ocean is about

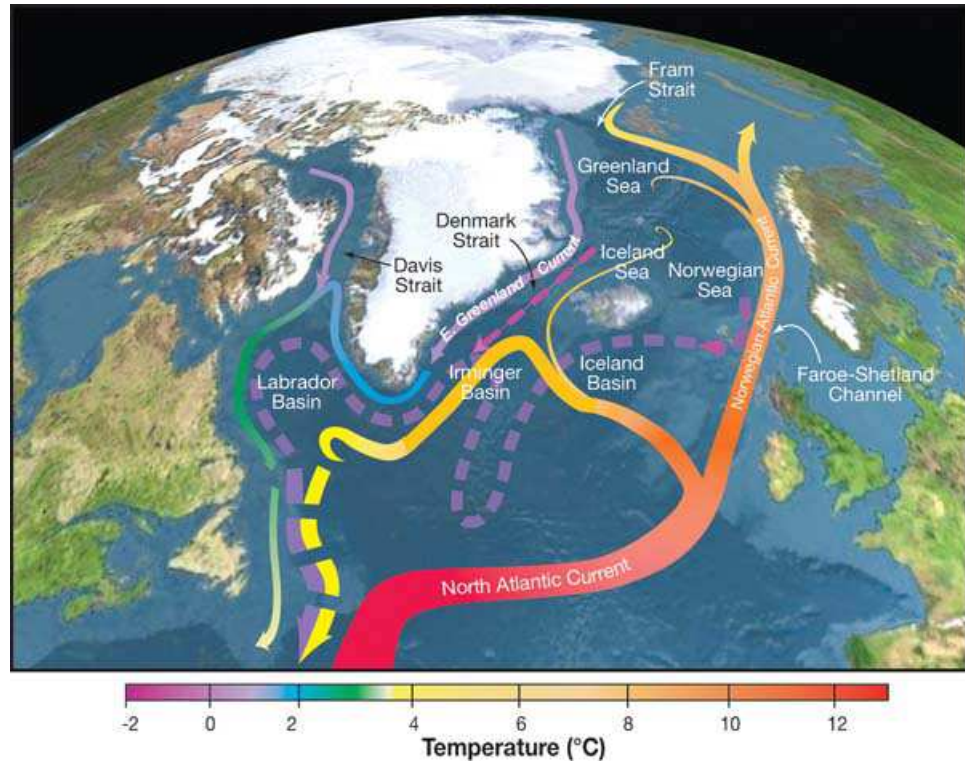


Figure 1.1: Map showing an overview of the circulation in the Nordic Seas and subpolar basins. The flow of the surface currents (solid curves) and deep currents (dashed curves) is presented. Colors of curves follow the temperatures. Source: R. Curry, Woods Hole Oceanographic Institution/Science/ USGRP.

of 0.53 ± 0.16 PW at 20°N during the period 1958-2004 as computed by Zheng and Giese, 2009. This difference could be attributed to the strong overturning cell in the North Atlantic, where the formation of the deep water masses takes place compared to the overturning cell in the Pacific.

Several studies [Dickson et al., 1996; Häkkinen 1999; Eden and Willebrand, 2001] have referred to the connection between the intensity of the deep water formation and the local buoyancy fluxes using the comparison between observations and model outputs. In spite of the uncertain connection between the changes of the formation rate and the AMOC strength [Mauritzen and Häkkinen, 1999], some studies using simulations [Gregory et al., 2005] suggest a connection between the anomalies of the AMOC's strength and the deep water formation rate. Large changes in the formation rate of the Labrador Sea Water (LSW) can be caused by climatic variations [Rhines et al., 2008]. Previous studies using model simulations [Böning et al., 2008; Biastoch et

1. INTRODUCTION

al., 2008] present the correlation between the AMOC strength variability and the LSW formation with a lag of 2-4 years. This lag could be explained by the dominant high frequencies of the local atmospheric forcing and eddy variability, disputing the claims of the AMOC long-term variability changes linked to the deep water formation. This explanation is supported by the comparison of the maximum values between the local surface forcing in the North Atlantic and the AMOC strength at 48°N [Biaostoch et al., 2008].

However, the results by Köhl and Stammer, [2008] suggest that there is no significant connection between the AMOC strength variability and the rate of the LSW formation, as examined at 25°N . Instead, this study shows that the AMOC variability at 25°N is explained by the fluctuations of the Denmark Strait Overflow Water (DSOW) anomalies as described therein. Figure 1.2 shows the anomalies of the AMOC strength with respect to interannual and decadal timescales at different latitudes in the North Atlantic using observations and model simulations during the period from 1950 to 2010. The amplitude of the AMOC anomalies has been estimated at about 2 Sv in several studies. Links between the AMOC strength and the dense water formation rate are vague.

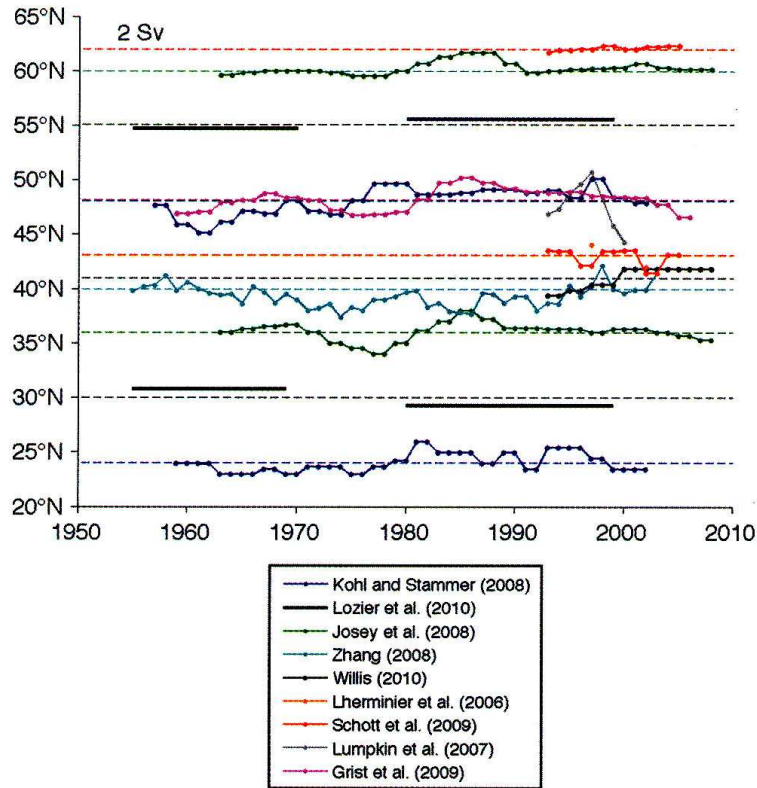


Figure 1.2: Estimates of AMOC transport at various latitudes in the North Atlantic from observations and model assimilations [Bullister et al., 2013]

1.2 Topographic setting of the North Atlantic

The ocean circulation, especially as the deep currents are concerned, is related to the geomorphology of the ocean floor. The Mid-Atlantic Ridge (MAR) is a submarine mountain range, where four tectonic plates meet: the North American, Eurasian, South American and African. The Mid North Atlantic Ridge is in the middle of the European and the American continent across the Atlantic and it divides the ocean floor into two basins the western and eastern basin. The crest of the MAR ranges from 1500 to 2000 m depth. Crossing the MAR, the exchange transport of the surface to deep water masses between the eastern and western basin is associated with several deep passages. One of this passages is the Charlie - Gibbs Fracture Zone (CGFZ), which is the deepest one in the Subpolar North Atlantic (SPNA), near to $52^{\circ}\text{N } 32^{\circ}\text{W}$ with maximum depth of 3000 m. Another zone is the Romanche Fracture Zones at the Equator with a maximum depth of 4500 m. In the North Atlantic region, the Reykjanes Ridge is the extension

1. INTRODUCTION

of the MAR from the CGFZ to Iceland. At the northern part of the ridge, at 57°N , there is the Bight Fracture zone with a depth of about 2500 m.

Additionally, the Greenland-Scotland Ridge (GSR) is a topographic feature, which extends from northwest to southeast and is an underwater border between the North Atlantic and the Nordic Sea as well as the Arctic Ocean. The overflow of the water masses from the north follows the sill pathways along the GSR through the Denmark Strait (between Iceland and East Greenland) and the Iceland-Scotland Ridge (between Iceland and the Scotland). Due to the ridges and the MAR, the subpolar North Atlantic is divided into several basins, some of these basins are the Irminger, Iceland, Labrador basin.

1.3 Circulation in the Subpolar North Atlantic region and water mass formation

In this section, the surface and the deep ocean circulation in the Subpolar North Atlantic region (SPNA) and the governing mechanisms of this circulation are described.

1.3.1 Surface circulation

The North Atlantic can be divided into two gyres, the subtropical gyre that extends from 20°N to 50°N and the subpolar gyre from 50°N to the Greenland-Scotland Ridge. The subpolar gyre is divided into two parts, the western and the eastern part. The subpolar gyre is characterized by a cyclonic rotation, including the Labrador Sea and the Irminger Sea. In this section, the circulation in the western part of the subpolar gyre is described. The surface circulation in the subtropical North Atlantic is dominated by the Gulf stream, which is mainly a wind driven current. The Gulf stream crosses into the subpolar region at about 50°W and when it reaches offshore to the Newfoundland basin it becomes a part of the North Atlantic Current (NAC) (Figure 1.3). Due to the subpolar front (interaction of the subpolar and subtropical gyre) at 52°N close to the Charlie-Gibbs Fracture zone [Bubnov, 1994], the NAC flow is turning eastward. Crossing the MAR, the transport of the NAC reaches in the Nordic Seas and Arctic Ocean. In the Irminger Sea in the subpolar region, the Irminger current is divided into two branches. One branch has a northward flow through the Denmark Strait and the other branch recirculates in the Irminger Basin [Pickart et al., 2005] and joins the southward flow of the East Greenland Current (EGC) coming from the Nordic Seas, the northward flow of the West Greenland Current and the southward flow of the Labrador

Current (LC in Figure. 1.1, green color) along the Labrador coast. The surface layer is influenced by atmospheric forcing.

In recent studies investigating the northward flow of the NAC close to the Deep Western Boundary Current (DWBC), the amount of the NAC's volume transport in the whole water column is about 110 Sv at 47°N using observed velocity sections [Mertens et al., 2014]. Further quantification of the NAC's volume transport in the aforementioned study suggests that the volume transport is about 45 Sv on the surface layer and 65 Sv on the deep layer. It should be noticed that a part of the NAC's flow recirculates east of the NAC at 47°N with a total amount of about 80 Sv. Furthermore, the mean transport of the NAC along the pathway from the western to the eastern basin between 47°40'N and 52°30'N is about 27 ± 5 Sv, including 60% warm subtropical water and 40% subpolar water [Roessler et al., 2015]. The changes of the NAC's properties (temperature and salinity) are most likely associated with the heat loss due to the northward flow of the NAC. Due to the transport of the surface warm/saline water masses from the subtropics to the northern region, heat is released into the atmosphere, changing the water mass properties (becoming colder and denser water masses). As a result, the cooled water mass becomes unstable, sinks and is transferred by currents, eddies or meanders from the high latitudes to equatorwards. Due to this physical process, the formation/modification of the North Atlantic Deep water (NADW) takes place at the high latitudes (Labrador Basin and Irminger Sea) in the North Atlantic.

The intense activity of the deep convection event is associated with the variability of the atmospheric forcing, which could be expressed by the North Atlantic Oscillation index (NAO) [Hurrell, 1995]. This association is expressed by the relationship between the NAO and the heat loss. A positive NAO is associated with strong westerlies and subsequently leads to intense deep convection events. It should be mentioned that there is not a perfect correlation between the NAO index and the deep convection, because the precondition process of the water formation determines the depth of the convection and the NAO is related to the atmospheric variability.

1. INTRODUCTION

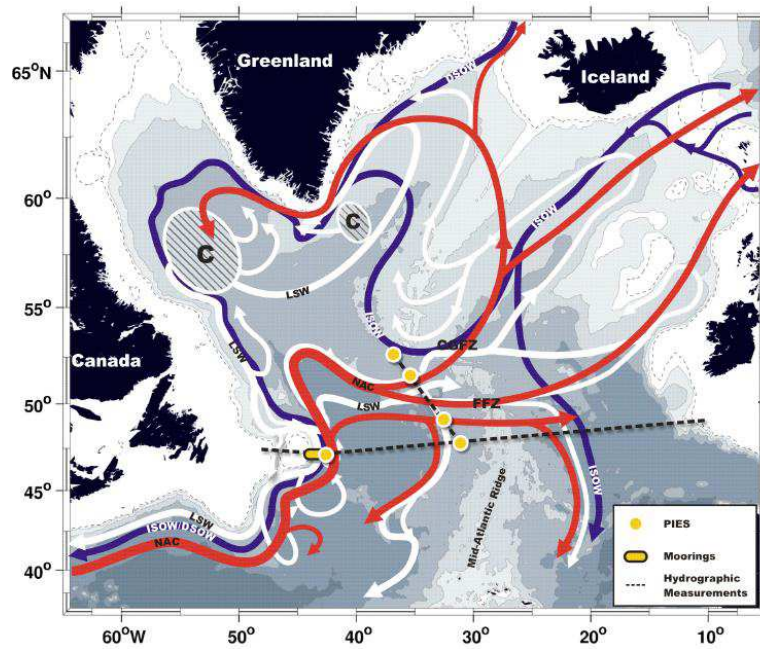


Figure 1.3: Circulation of main water masses in the subpolar North Atlantic. White: LSW, White hatched areas named C: Convection areas where formation of UNADW (LSW) could occur, blue: ISOW and DSOW, red North Atlantic Current NAC (upper 500m). The NAC is included since its strong currents could reach down to the bottom and carry deep and bottom water [Bullister et al., 2013].

1.3.2 Water masses of the Subpolar North Atlantic

The formation of the dense water masses takes place in several regions (e.g in the Labrador Sea in North Atlantic) on the ocean worldwide. The formation of the North Atlantic Deep Water (NADW) takes place in the North Atlantic region. The NADW contains several water masses that are formed not only by deep convection during the winter period in the Labrador Sea but also by the overflow of dense waters across the Greenland-Iceland-Scotland Ridge. The NADW is divided into two parts the Upper NADW (UNADW) and the Lower NADW (LNADW). The major component of UNADW is called Labrador Sea Water (LSW). The formation of these UNADW dense waters is mainly determined by the convection of the buoyancy loss or by the initially stratification of the water mass. The buoyancy loss is caused either by the air-sea fluxes, or sea-ice fluxes.

The LSW is divided into two modes the Upper Labrador Sea water (ULSW) in the density range of $\sigma_\theta = 27.68 - 27.74 \text{ kg/m}^3$ and the deep Labrador Sea Water (DLSW) in the density range of $\sigma_\theta = 27.74 - 27.80 \text{ kg/m}^3$ as described by Stramma et al., [2004] and Kieke et al., [2006; 2007;]. The difference between these two layers is due to differences in the intensity of the deep convection. The depth range of the LSW varies from 200 to 2000 m depending on the magnitude of the buoyancy loss. This connection has been established by Yashayaev and Loder [2009] during the winter period from 1987 to 1994, where a strong buoyancy loss leads to the LSW formation at 2500 m depth, as shown in Figure. 1.4, a. The Figure. 1.4 illustrates the volumetric inventories of the LSW formation in different time periods as well as in the three different basins, Labrador, Irminger and Iceland Basin.

The LNADW is characterized by Greenland-Scotland Overflow Waters with density range larger than $\sigma_\theta = 27.80 \text{ kg/m}^3$, separating into the Denmark Strait Overflow Water (DSOW) and Iceland- Scotland Overflow Water (ISOW). These water masses are originating in the intermediate layers of the Nordic Seas.

1. INTRODUCTION

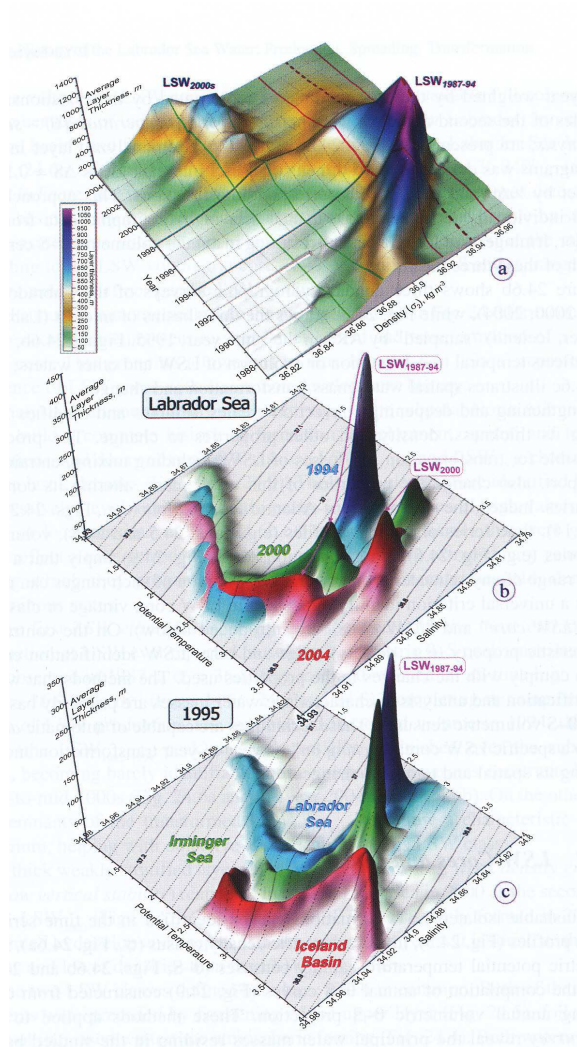


Figure 1.4: a) Evaluation of LSW in the Labrador Sea: a volumetric σ_2 - time plot showing the average thickness (meters) $\Delta\sigma_2 = 0.01\text{kg}/\text{m}^3$ layers in the Labrador Sea σ_2 is potential density anomaly referenced to 2000 db) ,b) temporal volumetric changes: 1994, 2000 and 2004, volumetric potential temperature (θ)-salinity (S) censuses of the Labrador Sea.c)Spatial distribution of the volumetric changes 1995, volumetric (θ)-(S) censuses of the Labrador, Irminger and Iceland basins. Each value in (b)and (c) represents the average thickness (in meters)of a $0.1^\circ \times 0.01 \Delta\theta \times \Delta\sigma$ layer. The solid and dashed lines are isolines of σ_2 (kg/m^3) defined by θ and S [Yashayaev et al., 2008].

1.3.3 Deep circulation in the Subpolar North Atlantic region

The deep currents are mainly density driven currents. They consist of the coldest and denser water masses. These water masses are characterized by Greenland-Scotland Overflow Waters with density range larger than $\sigma_\theta = 27.80 \text{ kg/m}^3$, being separated into the DSOW and ISOW. These water masses are originating in the intermediate layers of the Nordic Sea. DSOW is warmer than ISOW when exiting through the channels (the 640 m deep Denmark Strait and the 840 m deep Faroe-Bank channel, respectively). The downstream entrainment is stronger for ISOW than DSOW. The resulting water mass in the DWBC is therefore warmer/less dense. The total transport of the overflow water (ISOW and DSOW) has been estimated at about 6 Sv, consisting of 3-3.4 Sv in the Denmark strait [Jochumsen et al., 2012; Girton et al., 2001], 1 Sv across the Iceland-Faroe Ridge [Hansen and Østerhus 2000] and 2.2 Sv in the Faroe-Bank Channel [Hansen and Østerhus, 2007].

Although, the LSW southward flow feeds into the lower limb of the AMOC, the direct connection between the LSW formation and the strength of the AMOC variability is uncertain. The potential temperature and salinity of the aforementioned water masses are depicted in Figure 1.4. In recent studies [Bower et al., 2009, 2011; Kieke et al., 2009], the transport of the UNADW masses, which overlays the DSOW from the subpolar to the subtropical regions, occurs in the DWBC along the continental shelf and via interior pathways. The distribution of NADW is characterized not only by the recirculation in the Labrador basin but also by the transport from the north to the south. The NADW follows the topography along the slope of the continental shelf at the Grand Banks of Newfoundland. The DWBC in the subpolar gyre depicts the main export pathway from the subpolar region to the subtropical region of the water masses. At the Grand Banks, links between the DWBC and the NAC are associated with the LSW transport to the interior basin of Newfoundland [Kieke et al., 2009].

The mean values and the standard deviation of the volume transport at each water mass using observations at 53°N is about -6.3 ± 0.2 Sv at the surface layer, -8.9 ± 1.4 Sv in the ULSW density layer and -11.3 ± 1 Sv in the DLSW layer [Fischer et al., 2010], respectively.

1.4 Scientific background of the circulation around the Flemish Cap region

The major equatorward transport pathway of both LSW modes from the Labrador Sea is the DWBC along the continental slope (Figure 1.5). In the western flank of the Labrador Sea the DWBC forms the deep layer of the Labrador Current, which is a surface intensified current more confined on the shelf break [Fischer et al., 2004]. The southward DWBC flow at 47°N was determined to be around 30 Sv by Mertens et al., [2014] from observations, which is 5 Sv less than the transports at 53°N as suggested by Fischer et al., [2010]. Thus, interior pathways can contribute to the LSW export from the subpolar gyre to the subtropics, as described by Bower et al., [2009] from an analysis of RAFOS float tracks. Additionally, Kieke et al., [2009] corroborated the importance of interior pathways using mooring data close to the MidAtlantic Ridge, where the LSW turns to the east.

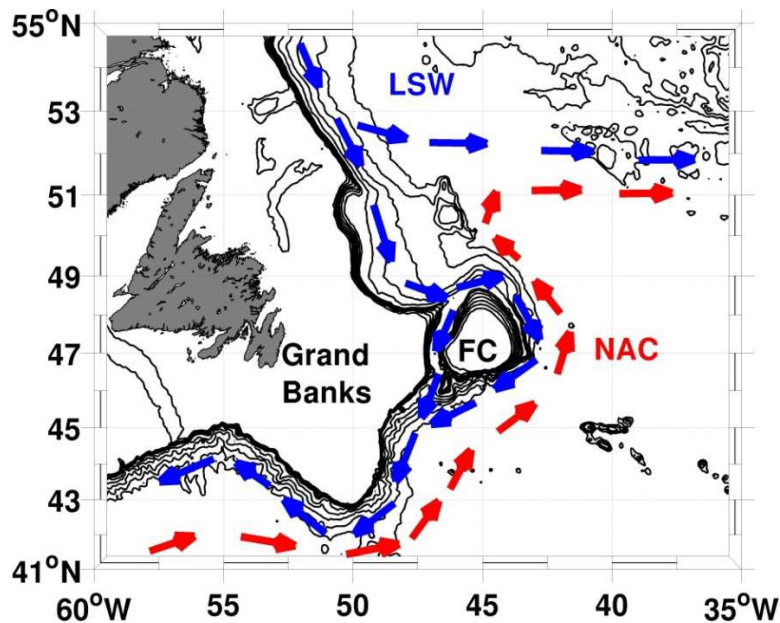


Figure 1.5: Map showing the schematic spreading pathways of Labrador Sea Water (LSW) in the studied region (blue arrows). Red arrows indicate the path of the North Atlantic Current (NAC). Flemish Pass is the passage between Flemish Cap (FC) and the Grand Banks. The convection area in the Labrador Sea is north of the shown region. Isobaths are given every 100 m between 400 m and 1000 m and every 500 m from 1000 m to 3500 m [Varotsou et al., 2015].

The plateau at Flemish Cap, a topographic feature in the study domain (centered at $45^{\circ}\text{W}/47^{\circ}\text{N}$), plays a role in the distribution of the LSW variability. When the DWBC flow reaches the northern part of the Grand Banks at 49°N the ULSW layer is divided into two branches due to the topographic obstacle that the Flemish Cap creates (Figure. 1.5). The inshore ULSW branch goes through Flemish Pass (passage of about 1500 m in depth between the Grand Banks and the Flemish Cap centered at 47°N) and the offshore branch occupies the eastern flank of Flemish Cap, a path which is followed by the DLSW flow. The majority of the current at Flemish Pass are southward, but there is a weak northward flow of warm and saline water at the eastern side of the pass [Stein, 1996; Rhein et al., 2011]. This flow is part of an anticyclonic gyre around Flemish Cap [Gil et al., 2004]. The area around Flemish Cap is a challenging region for the study of the DWBC export not only due to that topographic obstacle but also due to the influence of strong local atmospheric forcing and the interaction with the nearby North Atlantic Current (NAC) as pointed out by [Mertens et al., 2014]. The transport variability of the Labrador Current around the Flemish Cap area was investigated by Han et al., [2008] using a finite element model. A seasonal variation at Flemish Pass (top to bottom transport) of 5.2 Sv and a total transport through Flemish Pass of 7.5 Sv was reported in that modeling study. The transport due to remote wind effects amounts 1 Sv.

The variability of the ULSW southward transport through Flemish Pass and on the east part of Flemish Cap still lacks detailed studies on the seasonal and interannual time scale. Additionally, the impact of NAC position changes on the DWBC, and therefore on the ULSW export around the Flemish Cap, has not received much attention until recently: Mertens et al., [2014] discussed the interaction of the ULSW flow in the DWBC off Flemish Cap with the NAC, which was found to influence the salinity distribution mainly on the west of 42°W , but not close to the slope. Previous studies mainly focused on the quasi-permanent surface anticyclonic gyre above the Cap [Colbourne and Foote, 2000; Ross, 1981]. Using an ocean climatology, Gil et al., [2004] analyzed geostrophic transports in the surface layers (from 10 to 400 m along 47°N) and hypothesized that NAC intrusions may weaken the anticyclonic gyre above the cap.

Several physical mechanisms, which govern the LSW fluctuations, were examined by Dickson et al. [1996]. The authors showed that variations of the LSW formation have been related to the amplitude and phase of the NAO. Dengler et al., [2006] showed that changes of the subpolar gyre strength contribute to the variation of the LSW southward export. Moreover, the equatorward export of LSW from the subpolar gyre

1. INTRODUCTION

is increasingly receiving attention [Bower et al., 2009, Kieke et al., 2009; Lozier et al., 2013] due to its connection with the AMOC and its possible influence on future circulation changes. Changes of the layer thickness are related to the LSW fluctuations as pointed out by Stramma et al., [2004] showing that the weakened layer thickness of the ULSW has been associated with the minimum of the potential vorticity. In addition, the changes of the layer thickness have been estimated by applying the CFC inventory method [Rhein et al., 2002].

The purpose of the present study is to investigate the variability of the southward transport of the ULSW in the Flemish Pass and in the DWBC at 47°N and at 53°N using the output from a high resolution ocean model on a monthly and daily basis. Focus is placed on the physical mechanisms governing the transport variability of the ULSW export on seasonal and interannual timescales using a monthly basis. The results will first indicate the important role of the Flemish Pass region for the ULSW transport, which on average is not negligible. The transport variability at Flemish Pass presents a different behavior from that within the DWBC at 47°N not only on seasonal timescale but also at interannual time scales. In order to examine the importance of driving mechanisms, a running correlation method is applied to several parameters and the importance of either local and/or remote atmospheric forcing and of changes in the NAC's position and upstream current fluctuations is discussed. It should be noted that I focus on the transport variability in the ULSW and how it is intensified by changes to the transport variability in the surface layer. In spite of the southward transport of the DLSW in the DWBC according to the literature, the DLSW transport through Flemish Pass is negligible. By using the model outputs on a daily basis, the propagating signal of ULSW volume transport variability in the DWBC along the slope of the Continental shelf of Newfoundland at the high frequencies in periods $T \leq 25$ days is investigated. In order to analyse the propagating signal along the slope, the phase speed of various parameters (layer thickness in the ULSW density range, the U and V velocity anomalies) is computed by the slope of the examined anomalies. The estimated results have been compared with the predicted results from the Brink-Chapman [1987] software package producing the coastal trapped waves.

1.5 Outline of the thesis

The aim of this thesis is to investigate the relevant processes of the Upper Labrador Sea Water (ULSW) volume transport variability through Flemish Pass and around Flemish Cap with respect to the interannual and seasonal timescale using modeled outputs on

a monthly basis. These processes are the changes of

- (a) the monthly North Atlantic Oscillation (NAO) index,
- (b) the Ekman transport at each of the sections,
- (c) the Upper Labrador Sea Water (LSW) formation rate in the Labrador Sea,
- (d) the North Atlantic Current (NAC) distance to Flemish Cap at 47°N ,
- (e) the averaged transport intensity of the Subpolar Gyre.

Additionally, due to the strong signal of the ULSW volume transport at the high frequencies, the ULSW volume transport variability at high frequencies is investigated by using model outputs on a daily basis. The ULSW volume transports at high frequencies could be attributed to coastal trapped waves along the slope in the Deep Western Boundary current at the Grand Banks. The propagating wave signal is analysed by using a conceptual model [Brink-Chapman, 1987].

Chapter 2 (Data & Methodology) provides information on the configuration of the model, the data and the statistical tools used for the analysis of the data. The data is derived from a high resolution 8 km ocean model on both monthly and daily basis. The first part of this chapter introduces the validation of the model, which is based on the comparison between observations and model outputs using different parameters. Firstly, a comparison of the temperature timeseries at 53°N and then secondly the transport timeseries at Flemish Pass and in the DWBC at 47°N between observations and simulations providing qualitative and quantitative analysis of the outputs is presented.

Chapter 3 presents an overview of the average ULSW transport at the study region. Power spectral density of the volume transport at 53°N , at 47°N in the DWBC and at Flemish Pass either on the surface layer or in the ULSW density layer shows the peak of energy at different frequencies. Due to peaks of energy of the volume transport variability, the analysis is focusing on the long- and short term variation. Furthermore, I investigate the averaged (50 years) seasonal cycle of the volume transport variability at the selected sections in different density layers using the outputs on a monthly basis. The contribution of the volume transport on the surface layer and Ekman transport at the selected sections to the ULSW volume transport on seasonal cycle is depicted. Additionally, the changes of ULSW volume transport at the seasonal cycle with respect to the layer thickness and velocity variance are investigated.

1. INTRODUCTION

Chapter 4 presents the influences of the volume transport in the ULSW density layer from the atmospheric influenced surface layer with respect to interannual timescale. The analysis is based on the running correlation coefficient (rcc) method and it aims to provide the correlation coefficient between the timeseries of the studied parameters relative to time. The significance of this correlation is tested in two independent ways: first with p values and second with a bootstrapping method. The second part of this chapter shows the effects on the ULSW volume transports at interannual timescales of the selected sections relative to the velocity and the layer thickness variations.

In Chapter 5, the focus is the temporal evolution of the ULSW volume transport at the selected sections at interannual timescale. A comparison between the transport variability and the other physical parameters is based on the rcc method on the interannual timescale. The last part of the analysis is already published in Varotsou et al., [2015].

Chapter 6 is concerned with the ULSW volume transport at high frequencies using data on daily basis. In order to investigate the strong propagating signal of the ULSW volume transport along the slope of the Continental shelf corresponding to periods $T \leq 25$ days, a comparison between the estimated results by the model outputs and the predicted results by the used Brink-Chapman [1987] software package producing the coastal trapped waves is presented.

Finally, overall conclusions are presented, together with an outlook for further research aspects and discussion.

Chapter 2

Data and Methodology

This chapter introduces the configuration of the high resolution ocean-model. The comparison of the variability of several parameters in various regions in the North Atlantic shows the realistic response of the model outputs to the observations. The comparison is demonstrated for the validation of the model. The statistical significance and the statistical tools used for the analysis of the outputs are given below.

2.1 MITgcm model

In this thesis, outputs from a high resolution configuration of the coupled sea ice-ocean MIT general circulation model [Marshall et al., 1997] are analyzed. The simulation encompasses the Atlantic Ocean north of 33°S and includes the Mediterranean Sea, the Nordic Seas and the Arctic Ocean, as described by Serra et al., 2010. The model is eddy-resolving with a horizontal resolution of about 8 km in the region of interest (41°N - $54^{\circ}\text{N}/53^{\circ}\text{W}$ - 40°W) and in the vertical it includes 50 levels, with 10 m grid spacing near the surface increasing to 550 m at depth. The bottom topography was derived from the ETOPO2 database. The initial conditions of the model are provided by the annual mean temperature and salinity from WOCE Global Hydrographic Climatology [Gouretski and Koltermann, 2004].

The model is forced at the surface by fluxes of momentum, heat, and freshwater computed using bulk formulae and the 1948-2009 6-hourly atmospheric state from the NCEP RA1 reanalysis [Kalnay et al., 1996]. At the open southern boundary, the model is forced by a 1° resolution global solution of the MITgcm forced by the same NCEP data set. The model's northern open boundary, which balances a corresponding outflow through the southern boundary, is at Bering Strait where the barotropic net inflow is

2. DATA AND METHODOLOGY

0.9 Sv into the Arctic.

The relaxation of the model sea surface temperature is based on the ERSST V3 database on monthly basis from 1948 to 2009 [Smith et al., 2008] and the relaxation of the sea surface salinity is based on the WOA2005 climatology data [Boyer et al., 2005]. The vertical mixing parameterization uses the KPP formulation by Large et al., 1994]. Background coefficients of vertical diffusion and viscosity are both $10^{-5}m^2s^{-1}$. Horizontally, bi-harmonic diffusion and viscosity represent unresolved eddy mixing. Coefficients of horizontal diffusion and viscosity are both $5 \times 10^9m^4s^{-1}$. The model encompasses a dynamic thermodynamic sea ice model [Zhang and Rothrock, 2000] and solves for anthropogenic tracers. An annual averaged river run off [Fekete et al., 2000] is applied.

The present analyses are based on monthly and daily model output for the time period 1960-2009 and 2003-2009, respectively, for the region 41°N to 56°N and 68°W to 28°W , focusing the Flemish Pass and Cap area (at 47°N) and along the topographic slope of the Continental shelf at Grand Banks of Newfoundland (from 53°N to 51°N).

2.2 Model validation

The MITgcm model simulations have been used in several studies in the North Atlantic. More specifically, the model simulation has been used to investigate the variability of the Nordic Seas inflow and outflow [Serra et al., 2010; Johannessen et al., 2014; Dimitrenko et al., 2014], the variability in Arctic freshwater content and export [Köhl and Serra, 2014; Koldunov et al., 2014] and the kinetic energy variability in the Subpolar North Atlantic [Brath et al., 2010]. Comparisons with observations therein have shown a high degree of realism in the model’s simulation. A very good agreement has been found in the comparison between observations and simulations in computations of fluxes at the Davis Strait, in order to estimate the freshwater export from the Arctic through the Canadian Archipelago. The southward volume and freshwater transports using the model outputs amount to 2.0 ± 0.6 Sv and 122 ± 36 mSv (N. Serra, personal communication), respectively, which agree well with the range of the observational estimates presented by Cuny et al. [2005] and Curry et al. [2011], amounting to 2.6 ± 1.0 Sv volume, 92 ± 34 mSv freshwater transports and 2.3 ± 0.7 Sv volume, 116 ± 41 mSv freshwater transports.

The model transports of ULSW through Flemish Pass and within the DWBC at 47°N are compared in Figure 2.1 with the available observational estimates using lowered Acoustic Doppler Current Profiler data for the period 2009-2014 [Mertens et al.,

2014; Schneider et al, 2015]. The observed transport estimates agree with the range of variability from the model run. Additionally, the average net transports are of similar magnitude (Flemish Pass: 1.4 ± 0.5 Sv from the model outputs (1960-2009) and 1.11 ± 0.3 Sv from observations (2009-2013); slope DWBC: 4.9 ± 1.3 Sv from the model and 5.1 ± 1.3 Sv from observations).

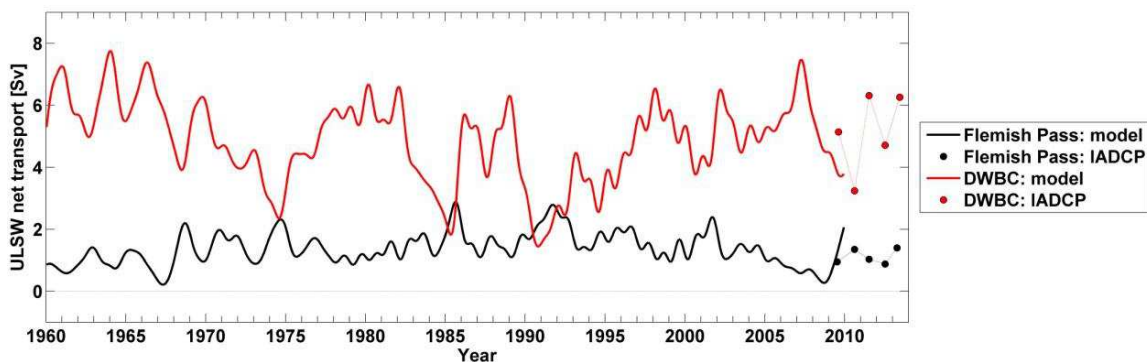


Figure 2.1: Monthly time series of de-seasoned (15-months low pass filtered) net ULSW transport (positive to the south) across 47°N within the DWBC (red) and through Flemish Pass (black) from monthly averaged model results (solid line) and from snapshots observed with lowered Acoustic Doppler Current Profiles (LADCP) (dots). Observational estimates are based on snapshots provided by Schneider et al., [2015].

The model’s output has been validated further using the hydrographic variability of the ULSW in Flemish Pass, showing the long term variability (Figure 2.2). A comparison between observations and model outputs shows a similar trend of temperatures and salinities in Flemish Pass during the period from 1994 to 2009, pointing to a warming ($0.3 \pm 0.1^\circ\text{C}/\text{decade}$) and salinification (0.03 ± 0.01 /decade for the model and 0.03 ± 0.02 PSU/decade for the observations) of ULSW [Schneider et al., 2015].

The definition of ULSW follows the density range of $\sigma_\theta = 27.68 - 27.74 \text{ kg/m}^3$ using the model outputs, as mentioned in Chapter 1. The ULSW transports result from the vertical and zonal integration of the meridional component of velocity depending on the study section in the area defined by 1) the upper and lower ULSW isopycnals and 2) either the continental slope and the Flemish Cap (for the case of the Flemish Pass) or the Flemish Cap and the first offshore position, where the time mean southward velocity is zero (in the case of the DWBC). The definitions are shown in Figure 2.3, presenting the 1960-2009 time averaged meridional velocity in the zonal sections (e.g. at 47°N) with the average upper and lower isopycnals defining the ULSW superimposed. Variations of ULSW layer thickness are taken into account in the computation since

2. DATA AND METHODOLOGY

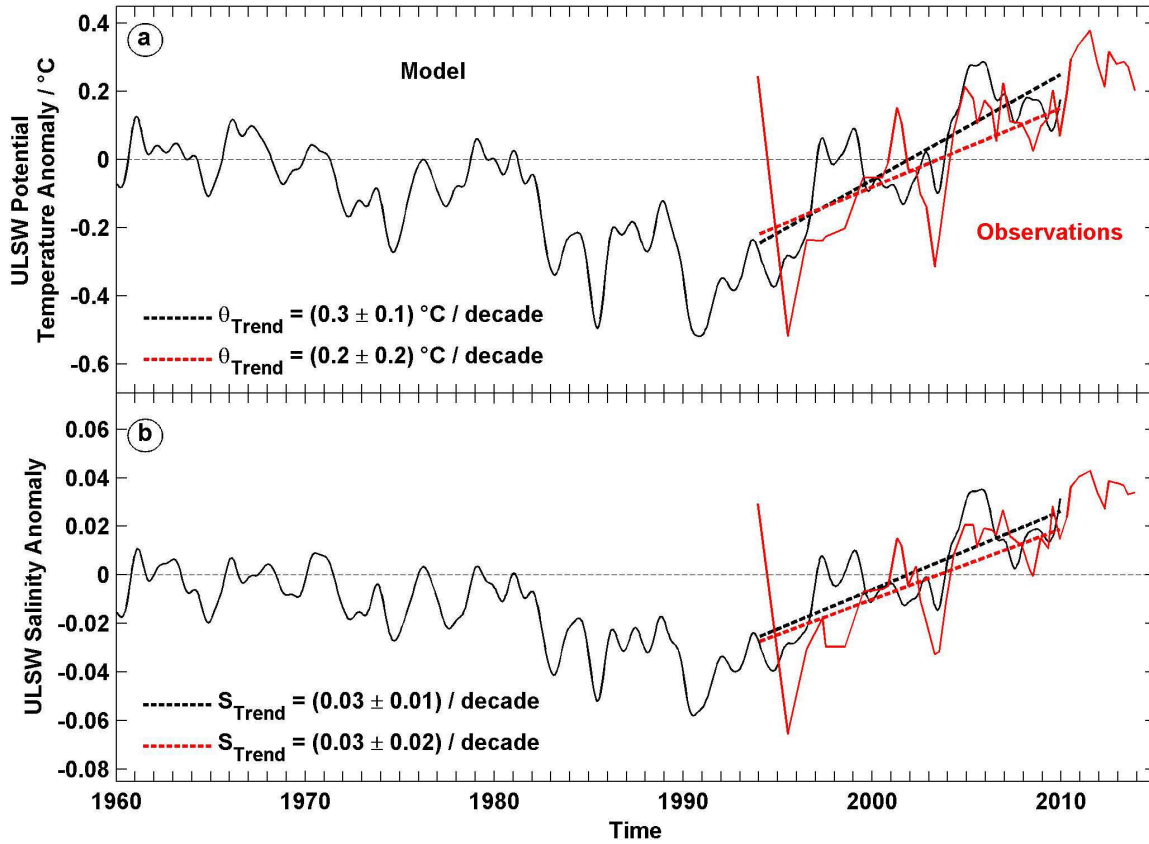


Figure 2.2: Time series of ULSW hydrographic properties in Flemish Pass at 47°N based on CTD measurements (red, seasonal cycle removed) and derived from the MIT-gcm model (black, 15 months low pass filtered). (a) Median potential temperature anomaly ($^\circ\text{C}$) and (b) median salinity anomaly relative to the mean of the period 1994 – 2009. Dashed lines indicate trends during the overlapping period 1994 – 2009 of both time series [Schneider et al., 2015].

monthly variations of the depth of the isopycnals are retained. On the other hand, the lateral transect boundaries are kept constant. The same process was repeated for the computation of the volume transport at other sections (e.g at 53°N or around the Flemish Cap area) but using the time averaged zonal velocity for meridional sections.

In order to gain further insight for the contribution of the layer thickness variability and the velocity’s variance to the volume transport in the ULSW density layer, transport based on the velocity variance T_{vel} . (2.1) and transport based on the layer

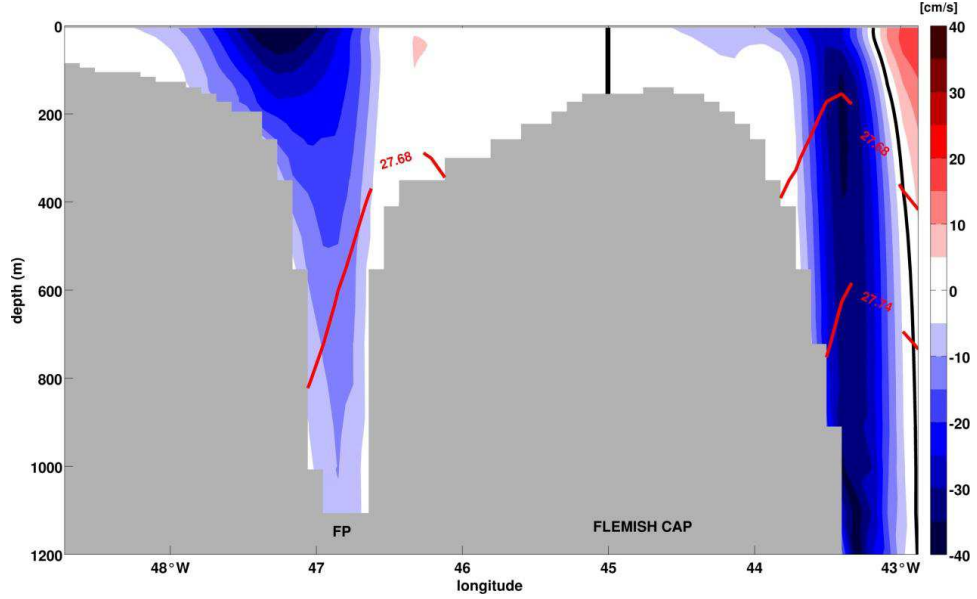


Figure 2.3: Vertical section of simulated 1960-2009 time-averaged meridional velocity at 47°N , showing the surface-intensified Labrador Current in the western Flemish Pass (FP), as well as the DWBC east of Flemish Cap. The limits of velocity integration for the ULSW transport computation are illustrated by the mean position of the density interfaces $\sigma_\theta = 27.68 \text{ kg/m}^3$ and $\sigma_\theta = 27.74 \text{ kg/m}^3$ and the position of the average zero mean velocity above Flemish Cap and east of Flemish Cap (thick black lines) [Varotsou et al., 2015].

thickness changes T_ρ (2.2) are computed.

$$T_{vel.} = \int_{x_0}^{x_n} \int_{z_1}^{z_2} v(x, z, t) dx dz \quad (2.1)$$

and

$$T_\rho = \int_{x_0}^{x_n} \int_{z_3}^{z_4} \bar{v}(x, z(t)) dx dz \quad (2.2)$$

The first component $T_{vel.}$ (2.1) denotes the transport variability, where the velocity varies on time with constant layer boundaries (z_1 and z_2) and constant boundaries on x-axis (x_n, x_0). A constant layer ranges from the mean depth of the upper isopycnal defining the ULSW to the mean depth of the lower boundary of ULSW at each section. The boundaries on x-axis are already described above. The second component T_ρ (2.2) denotes the transport variability, where the \bar{v} is the average velocity and the changes

2. DATA AND METHODOLOGY

of the variability are based on the variance of the layer thickness (z_3 and z_4) at each section. Additionally, the sum of these two components is presented in section 4.2.

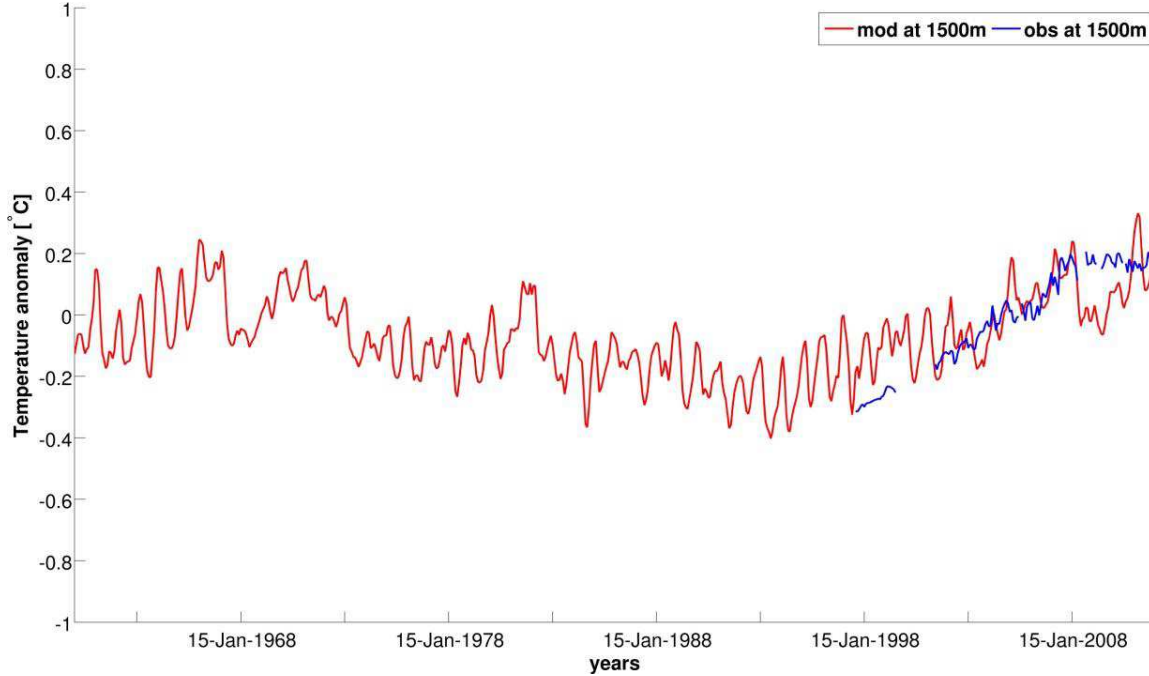


Figure 2.4: Anomalies of temperature observed at mooring K9 from [Fischer et al., 2010] (blue line) and the long term simulated temperature anomaly from 1948 to 2012 (red line) at the position $53^{\circ}\text{W}, 53^{\circ}\text{N}$ and at 1500 m depth. The anomalies were calculated relative to the period August 1997–April 2012. Observations were low-passed filtered (cut-off 60 days) and are shown as monthly means.

Further upstream at 53°N , model temperature anomalies (relative to the 1948–2009 time mean) at 1500 m depth in the Labrador Sea were compared with corresponding observational results from mooring K9 [Fischer et al., 2010]. Despite overestimating the magnitude of the anomalies, the observed warming trend in the Labrador Sea from the late 1990s until 2009 is seen in the model (Figure 2.4), suggesting that the long term variability in temperature is captured by the simulation.

In order to investigate the variability at high frequencies, the daily outputs are used. It should be mentioned that a comparison of the ULSW water mass between the data set of the monthly outputs and the data set of the daily outputs shows that the ULSW mass using the daily outputs is warmer and saltier than the ULSW mass using the monthly data. The difference in the density range of the ULSW water mass could be caused by using a modified viscosity parameter, which determines the diffusion and the

dissipation of the energy in the ocean model. More specifically, the viscosity parameter has been modified running the model for the producing daily outputs. In this case, the transport variability of the ULSW volume transport has been computed in the density range between $\sigma_\theta = 27.67 \text{ kg/m}^3$ and $\sigma_\theta = 27.73 \text{ kg/m}^3$, due to the changes of the viscosity. Therefore, for the computation of the ULSW volume transport using the daily outputs the variability of the layer thickness as well the changes of the velocity's variance is taken into account, while the boundaries on x-axis are the same as described above.

2.3 Methodology and Outputs

In order to quantify and qualify the contribution of the determining physical mechanisms to the ULSW volume transport, a comparison between various parameters and the ULSW volume transport is performed. The variability of the ULSW volume transport is related to variability of several physical parameters, which are described in detail in the following section.

2.3.1 Parameters representing forcing mechanisms

In order to identify the main mechanisms responsible for ULSW transport variations in different time periods, the time series of modeled volume transport were correlated with the transport variability at the surface layer and with five other time series representing selected physical processes generating variability (Figure 2.5): a) the monthly NAO index, b) the Ekman transport at each of the sections, c) the ULSW formation rate in the Labrador Sea, d) the NAC distance to Flemish Cap at 47°N and finally e) the averaged transport intensity of the Subpolar Gyre. The above time series include processes corresponding to remote (a) and local (b) atmospheric forcing and local (d) and basin-wide (c,e) ocean circulation changes.

- (a) The NAO index was retrieved from the NOAA NCEP web site

http://www.cpc.ncep.noaa.gov/products/precip/CWlink/daily_ao_index

while all other time series were extracted from the model.

- (b) For the computation of the Ekman transport at each section, the model surface momentum flux was used, which is computed internally in the model using bulk formulae.

2. DATA AND METHODOLOGY

- (c) The computation of the ULSW formation rate is based on a volume balance of the ULSW layer (defined by the density range $\sigma_\theta = 27.68 \text{ kg/m}^3$ to $\sigma_\theta = 27.74 \text{ kg/m}^3$ as in the observations) in a box extending from the southern tip of Greenland southward to 53°N and then westward to Canada, with Davis Strait and the coast as the northern and western boundaries. The volumetric balance states that: ULSW volume change = - horizontal divergence of ULSW + formation of ULSW, with the divergence being the difference between the north and south plus the difference between east and west area-integrated volume fluxes. In this study, the ULSW production in the Irminger Sea is not directly accounted for, but the eastern inflow into the considered box includes this contribution. Thus, for years of weak or no ULSW formation the obtained formation rate is negative due to export out of the box. The formation rate in the late 1990s to 2009 is 2.5 Sv on average, which is reasonably close to other estimates [Kieke et al., 2006; Myers and Donnelly, 2008].
- (d) The NAC position was computed as the zonal distance from the center of Flemish Cap (47°N and 45°W) to the maximum northward flow east of Flemish Cap at 47°N in the layer 200-500 m.
- (e) The subpolar averaged transport is based on the average over the Labrador Sea of the barotropic stream function, i.e., the top-to-bottom vertically- and zonally-integrated volume fluxes. The index thus represents the integrated transport from the Canadian coast to the minimum of the streamfunction in the subpolar gyre.

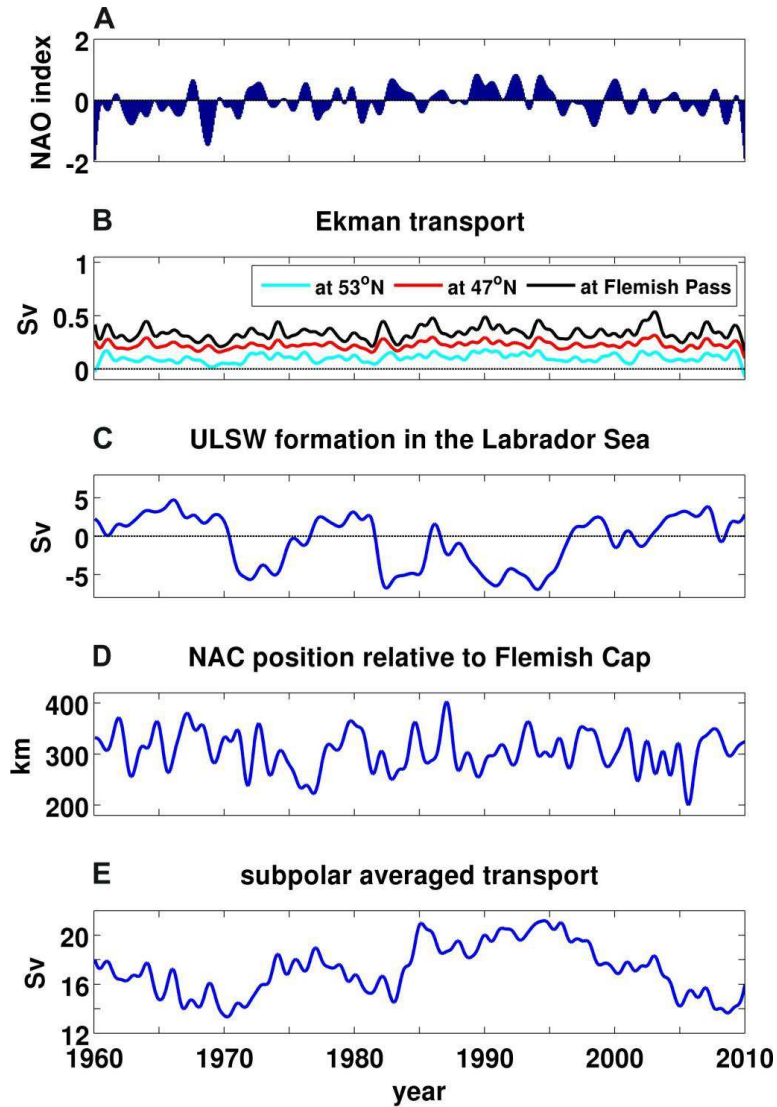


Figure 2.5: Monthly de-seasoned time series (low-pass filtered with 15 months cut-off) of parameters corresponding to potential agents responsible for the variability of ULSW transport over the study region: (A) the NAO index; (B) the Ekman transport at 53°N over the slope, at 47°N east of Flemish Cap and at Flemish Pass (an offset of $+0.1\text{ Sv}$ was added to the red line for clarity of the subfigure; positive values correspond to southward transport); (C) the rate of the ULSW formation in the subpolar gyre; (D) the NAC position relative to Flemish Cap; and (E) the subpolar gyre averaged transport. See text for a detailed description of the computation of parameters [Varotsou et al., 2015].

2.4 Statistical analysis

In order to evaluate the statistical significance of the power spectral density, a multi taper method is used. Additionally, a bootstrap method and the calculation of the p-values are used to provide the statistical significance of the running correlation coefficient method.

2.4.1 Power spectral density and statistical significance

In order to study the characteristics of the transport variability, the spectral analysis is applied. The analysis of the power spectral density is based on the multi taper method [Ghil et al.,2002]. The advantage of this method is the detection and the significance estimation of both harmonic and anharmonic peaks using the estimated background noise. The noise has been estimated depending on the quantiles of the chi-square distribution. The detection of the harmonic peak is derived from either the phase-coherent sinusoidal oscillations or the amplitude-and-phasemodulator. In particular, the applied method shows the dominant frequencies of the variability and it is especially useful for the isolation of the dominant signal of the variability using a band- or low pass filter. Furthermore, statistical significance is tested relative to the null hypothesis of a globally red noise background, which is computed empirically by using the data. The derivation of the red noise background uses an assumption of an AR(1) noise process. The AR noise process is based on an autoregressive (AR) model, which is a representation of a type of random process. The power spectrum of the AR (1) is provided by the following equation:

$$P(f) = \frac{P_o(1 - r^2)}{1 - 2rcos(\frac{\pi f}{f_N}) + r^2} \quad (2.3)$$

where P_o denotes the average value of the power spectrum, with regard to the variance σ is given by : $P_o = \frac{\sigma^2}{1-r^2}$

The r gives the lag-one autocorrelation and $f_N = \frac{0.5}{dt}$, the Nyquist frequency is the highest frequency that can be resolved at an obtained sampling rate dt . The characteristic noise decay time can be provided by $\tau = -\Delta t \log r$. The spectrum behaves as a white spectrum, when the periodicities are larger than τ .

2.4.2 Running correlation coefficient and statistical significance

In order to identify the process most relevant to the ULSW transport variability in Flemish Pass and in the DWBC, running correlations between the time series of the

ULSW transport anomalies and the forcing parameters listed above were calculated on interannual time scales. The advantage of this method is that it allows examining the changing correlation with time between every two time series in specific time windows, and therefore to estimate the consistent and discrepant behavior between the studied parameters at different times. As described by Zhao et al., [2006], the running correlation coefficient is given by the following expression:

$$R_i = \frac{\sum_{k=i-n}^{k=i+n} (X_k - \overline{X_k})(Y_k - \overline{Y_k})}{\sqrt{\sum_{k=i-n}^{k=i+n} (X_k - \overline{X_k})^2} \sqrt{\sum_{k=i-n}^{k=i+n} (Y_k - \overline{Y_k})^2}}, \text{ with } i = 1 + n \dots N - n,$$

where N denotes the total number of data values, X_k the first variable and Y_k the second variable. R_i gives the running correlation between two signals within the time of the used window length. A window length of 120 points (10 years) was chosen in the present work, since the aim is to address interannual variability.

Statistical significance is investigated applying two independent methods of estimation; by calculating the p-values and by random bootstrapping. The p-value represents testing the hypothesis of no correlation. Each p-value is the probability of a correlation as large as the obtained value by random chance, when the true correlation is zero. The calculation of p-values is based on the Pearson correlation coefficients [Cohen et al.,2003], as well as the effective degrees of freedom, which were derived from autocorrelation functions. t-value for a Pearson correlation is defined as:

$$t = \frac{r}{\sqrt{\frac{1-r^2}{n-2}}}$$

where r is the Pearson correlation coefficient and n is the total sample size.

Additionally, a bootstrap method [Efron and Gong, 1983; Varotsos et al., 2013] is used to estimate the confidence levels of the running correlation between any two time series. To that end, the first time series is correlated to synthetic time series composed by reordering the second time series randomly (but preserving seasonality). By re-using the second time series I preserve its autocorrelation function statistics. Then, both time series are band-pass filtered, and the running correlation between the original and the bootstrapped time series within the time of the used window length (10 years) is computed. In order to assess the significance limits of the running correlation method, this processing was repeated 20 times for each of the two time series, giving a range

2. DATA AND METHODOLOGY

of non-significant correlations. That is, all correlations obtained with the bootstrap method correspond to co-variability appearing only by chance.

Chapter 3

General circulation of the study region

In this chapter, an overview of the ocean circulation at the study region is given by the spatial distribution of the magnitude of the model's vertically integrated volume fluxes in the ULSW layer, the average downstream volume transports at the studied sections are computed as well. In order to analyse the volume transport variability in the surface and in the ULSW density layer, the power spectral density at each studied section is computed and presented. The peak of energy of the volume transport in two different density layers indicates where the signal of the volume transport variability is strong. The last part of this chapter provides a detailed description of the results of the analysis at low frequencies, namely the climatological seasonal cycle, in the surface layer and in the ULSW density layer as well as the interaction between these two layers on a seasonal timescale.

3.1 Circulation of the ULSW transport in the study region

Before the detailed analysis of the temporal transport variability around the Flemish Cap area is compared to the upstream fluctuations at 53°N , I am going to show an overview of the ULSW general circulation in the study area using the model outputs at the study sections. The selected sections represent the main pathway of the ULSW transport from the north to the south and the flow around the Flemish Cap area. The first view of the results is depicted in Figure 3.1, which presents the average magnitude of the vertically-integrated velocity in the ULSW layer.

3. GENERAL CIRCULATION OF THE STUDY REGION

As shown in Figure 3.1, the main export pathway of ULSW is southward within the DWBC and the volume transport at each section has been quantified using the model outputs. In Section A, at 53°N , the average ULSW volume transport is $6.7 \pm 1.9 \text{ Sv}$. In the southern Orphan Basin at 49°N , where the ULSW reaches the northern edge of the Grand Banks, the ULSW flow is divided into two branches due to the presence of Flemish Cap and Flemish Pass, following the 800 m isobath. While the majority of the flow goes around (east) that obstacle ($4.9 \pm 1.9 \text{ Sv}$, Section B), forming an offshore branch, some flow into the Flemish Pass occurs, forming an inshore branch ($1.4 \pm 0.8 \text{ Sv}$, Section C). The time-mean distribution of the ULSW volume transport shows that 72 % of the total southward transport (when defining the transport at 53°N as 100 %) goes around Flemish Cap and 20 % goes through Flemish Pass. The remaining part (8 %) diverts to the east into the central basin, following interior pathways.

The loss of volume transport from the DWBC begins downstream from the northern Flemish Cap (east of 45°W , Section D) and increases along the southward DWBC pathway towards the southern Grand Banks. The diversion of ULSW from the boundary flow is probably induced by eddies, which are identified as meandering structures in the averaged volume flux map in Figure 3.1. Nevertheless, the largest fraction of the volume transport of ULSW goes around Flemish Cap within the DWBC but a significant part is present at Flemish Pass. South of 46°N the two current branches merge and form a strong southwestward flow around the topography of the southern Grand Banks. There, the southward transport amounts to $4.5 \pm 1.3 \text{ Sv}$, therefore reduced by about 2 Sv from its value at 53°N .

The average current width in the ULSW layer which derives from the vertically integrated velocity is 170 km at 53°N and 280 km at 49°N , while the widening probably occurs due to a change in topographic slope. The average magnitude of the flux is strong within the DWBC (from 53°N to 46°N) but is weaker at the southern flank of Flemish Cap ($3.3 \pm 1.9 \text{ Sv}$, Section E in Figure 3.1). Here, the mean ULSW transport is reduced from the value at Flemish Caps eastern flank by about 1.5 Sv, which is likely caused by NAC's meanders and/or eddies, which are still seen offshore in the time mean distribution. South of 46°N , the ULSW flow in the boundary current increases again and the width of the average current is 152 km in the ULSW layer.

Further enhancement of the important role of the ULSW transport through Flemish Pass is confirmed by using an isolated box (Figure 3.2) from 47°N to 45°N . By using a closed box (from the shelf to 45°W at Flemish Cap (F.C.) in the zonal direction and from 47°N to 45°N in the meridional direction), the lateral fluxes are isolated and the ULSW volume transport at the 45°N section shows the ULSW southward transport.

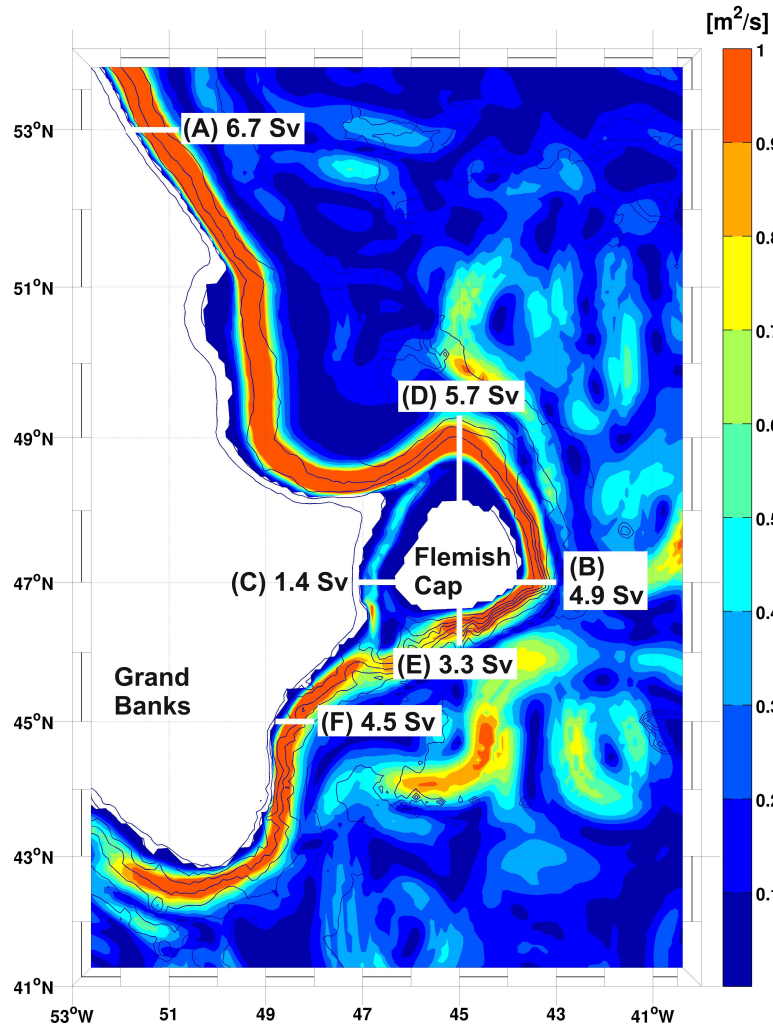


Figure 3.1: Map showing the magnitude of the vertically integrated volume fluxes in the model ULSW layer (color) and the average downstream volume transports across the shown sections (A-F, white). Isobaths are given from 0 to 4000 m in 400 m intervals as thin black lines in the background [Varotsou et al., 2015].

The results of this method show that the contribution of the ULSW volume transport through Flemish Pass (F.P.) to the total amount of the ULSW downstream transport at 45°N is about 10% more than the ULSW volume transport at 47°N through Flemish Pass, as described above.

3. GENERAL CIRCULATION OF THE STUDY REGION

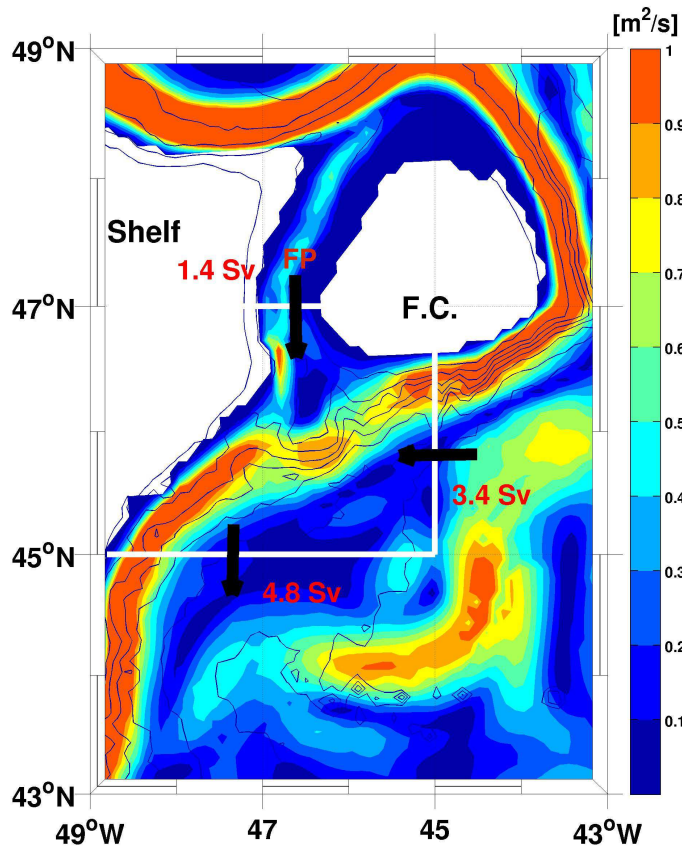


Figure 3.2: Sketch showing the inflow and outflow of the ULSW volume transport from the 47°N to 45°N .

3.2 Transport variability of the volume transport and its spectral analysis

The focus of this section is on the interpretation of the volume transport variability in the surface layer and in the ULSW density layer of three specific sections; at 53°N (A), at 47°N (B) and at Flemish Pass (C), as seen in Figure 3.1. In order to investigate the contribution of the transport variability in the surface layer to the transport variability in the ULSW density layer, the temporal evolution of the transport variability in the two different density layers is examined. An overview of the volume transport variability of the surface layer and in the ULSW volume transport at the examined sections is displayed in Figure 3.3. The estimation of volume transport variability at 47°N and at 53°N in the surface layer over the study period presents a strong variability with a strong seasonal cycle compared to the volume transport variability at Flemish Pass. In addition, the estimation of the ULSW volume transport variability presents a strong seasonal cycle at each section, while the amplitude of the transport in the DWBC at 53°N and at 47°N is stronger than the amplitude of the transport at Flemish Pass. A detailed analysis of the volume transport variability at the selected section in the two different density layers is described in the following sections.

In order to investigate the temporal evolution of the volume transport variability at the different density layers, the power spectral density at each density layer and at each section is computed by using the multi-taper method (MTM), providing an overview of the frequency characteristics of the flow (Figure 3.4 and 3.5). Significant peaks (above the 95% significance level) of energy were noted at high frequencies below the seasonal scale and at the annual frequency (12 months). The semiannual signal appears in both examined density layers but it is stronger in the volume transport variability in the surface layer than in the deeper layer. At all sections the interannual frequencies show a prominent peak at 3 years and additional peaks at five years and at lower frequencies (not significant in Flemish Pass) in the density layer of the ULSW (density range: $\sigma_\theta = 27.68 - 27.74 \text{ kg/m}^3$). However, there is no significant signal at the interannual frequency at 53°N in the surface layer (density layer $\sigma_\theta < 27.68 \text{ kg/m}^3$).

Nevertheless, the signal at interannual timescale (centered at 3 years) is strong not only for the transport variability in the surface layer but also for the transport variability in the ULSW density layer at the Flemish Pass section and at the east part of Flemish Cap. In order to focus on the interannual variability in the three year peak, a band-pass filter (cut off periods at 18 and 54 months, chapters 4 & 5) is applied to all examined time series, thus removing high and very-low frequency variations. It should

3. GENERAL CIRCULATION OF THE STUDY REGION

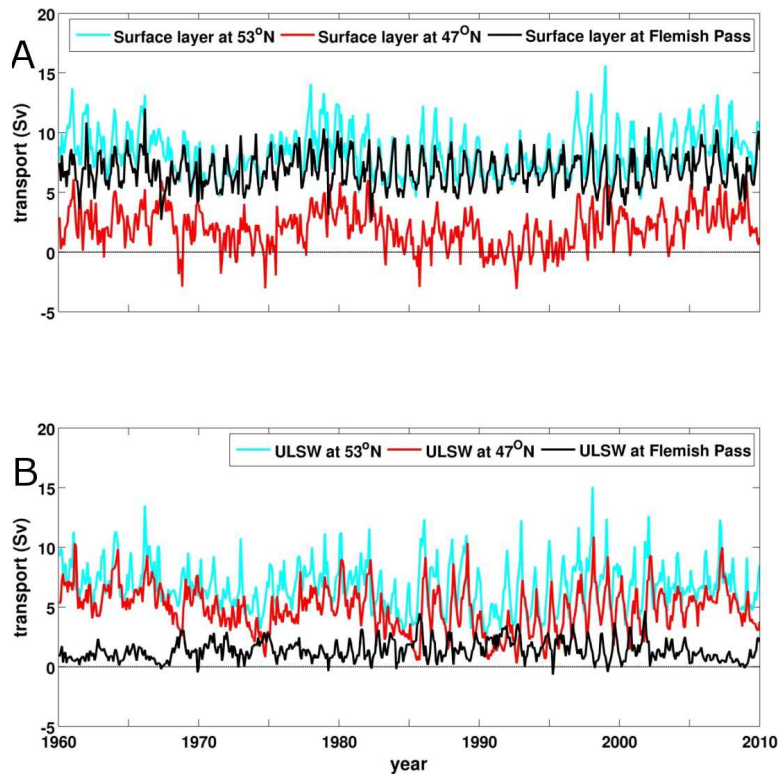


Figure 3.3: Unfiltered volume transport variability A) on the surface layer and B) in the ULSW density layer at the three examined sections

be noted that there is a significant peak at 12 months for all the studied sections. The climatological seasonal cycle of the transport variability is also discussed in the following section. The aim of this study is to investigate the temporal evolution of the volume transport in the surface layer as well as in the density layer of the ULSW at the climatological seasonal cycle.

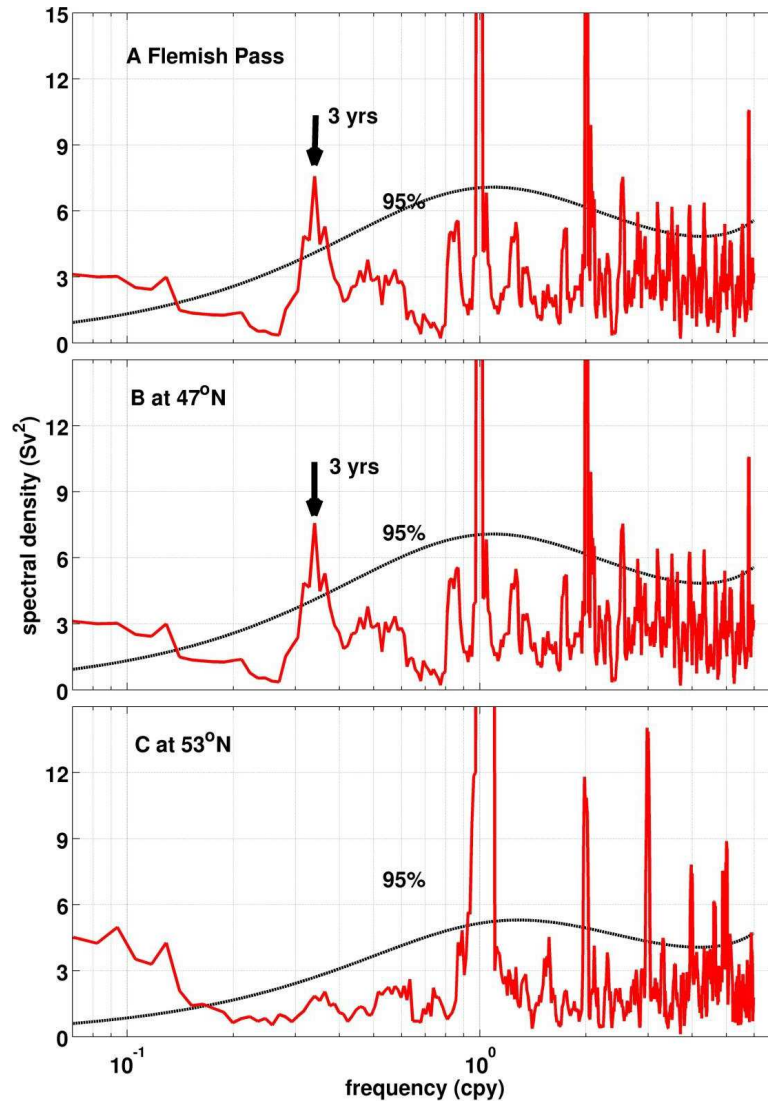


Figure 3.4: Variance preserving power spectra of monthly transports (unfiltered) in Flemish Pass (A) and at 47°N (B) and at 53°N (C) in surface layer ($\sigma_\theta < 27.68 \text{ kg/m}^3$) obtained by a multi-taper method following Ghil et al. [2002]. The significant peak of energy at the three year period is pointed out by the black arrow and the significance level at 95% by the dotted line.

3. GENERAL CIRCULATION OF THE STUDY REGION

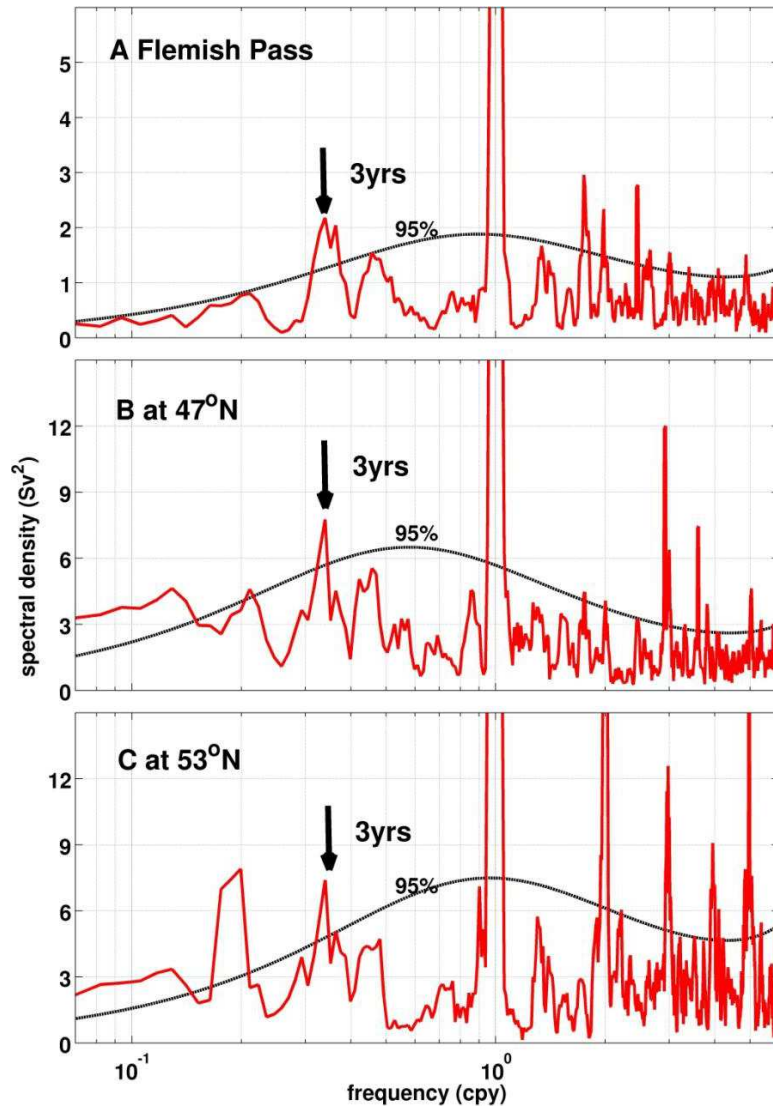


Figure 3.5: Same as Figure 3.4 but for the case of the ULSW transport variability (in the density layer $\sigma_\theta = 27.68 - 27.74 \text{ kg/m}^3$).

3.3 Seasonal cycle

In this section, the climatological seasonal cycle in the surface layer and in the ULSW layer is presented and it is computed by the monthly mean for each month over the study period. The seasonal climatological volume transports for each section in the two different density layers are displayed in Figures 3.6 and 3.8. The seasonal cycle is not shaped as a sinus curve and the strongest transport and amplitude is observed in

the DWBC at 53°N relative to the other sections in both density layers.

An overview of the climatological seasonal cycle in the surface layer (Figure 3.6) shows that the largest amount of the volume transport goes through Flemish Pass relative to the volume transport at the east part of Flemish Cap. Moreover, the transport variability at Flemish Pass appears to follow the transport variability at 53°N . A maximum of the southward volume transport through Flemish Pass coincides with a maximum of the volume transport at 53°N during the winter period, when the zonal wind stress is strong. This coincidence can be explained by the propagation of signals in the Labrador Current, which goes along the Continental Shelf. It should be mentioned that the seasonal amplitude of the volume transport at 47°N is smaller (0.92 Sv) compared to the other two sections (2 Sv at 53°N and 1.49 Sv at Flemish Pass) and the behavior of the volume transport at 47°N is different compared to the variability of the other two sections. Furthermore, a minimum of the southward transport variability at 47°N is presented 3 months after a minimum of the southward transport at 53°N and 5 months after a minimum of the southward transport through Flemish Pass. The

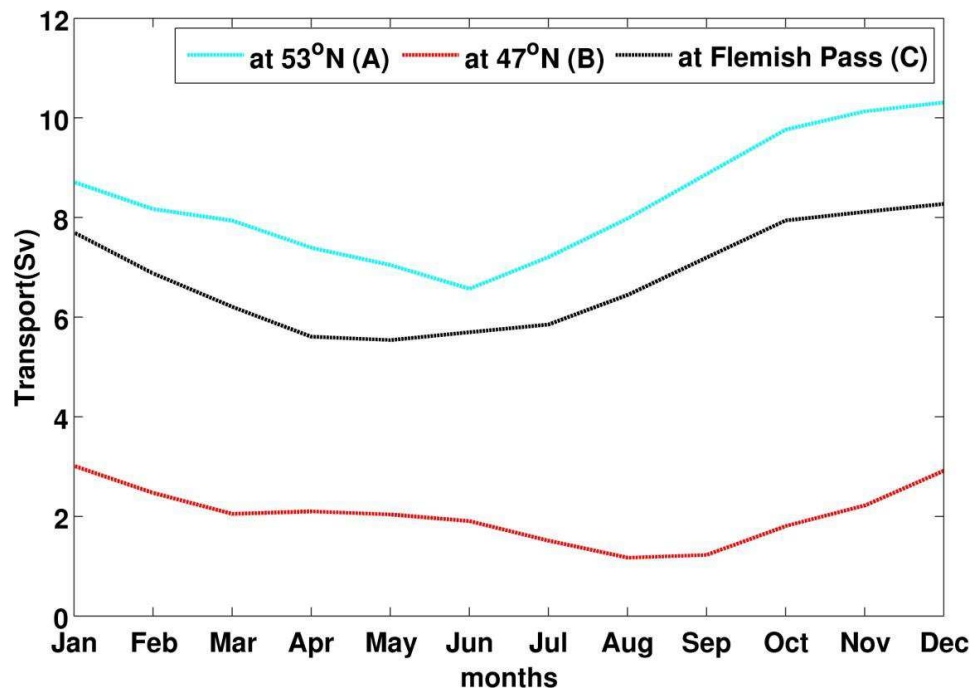


Figure 3.6: Average seasonal cycle of the surface layer volume transports (positive to the south) for each section of the three model sections highlighted in Figure 3.1 and computed over the period 1960-2009.

3. GENERAL CIRCULATION OF THE STUDY REGION

transport variability at each section is correlated positively with the Ekman transport (Figure 3.7) at each section due to the impact of the local atmospheric forcing. The positive correlation can be explained by the strong seasonal cycle of the atmospheric forcing with a maximum of the Ekman transport during the winter period (strong atmospheric forcing) and a minimum of Ekman transport at each section during the summer (mild atmospheric forcing).

On the other hand, when the seasonal cycle in the ULSW density layer is analyzed, the seasonal cycle at Flemish Pass has a different behavior when compared to the seasonal cycle in the DWBC at 53°N and at 47°N (Figure 3.8). A maximum southward transport at 53°N leads by one month the maximum southward transport in the DWBC at 47°N. The correlation coefficient of the two time series is positive ($r=0.8$) and significant.

The amplitude of the volume transport variability at Flemish Pass is weak relative to the amplitude of the volume transport at the other two sections in the DWBC. It is confirmed by the power spectral density, where the peak of the ULSW volume transport at Flemish is weaker than the amplitude of the ULSW volume transport in the DWBC.

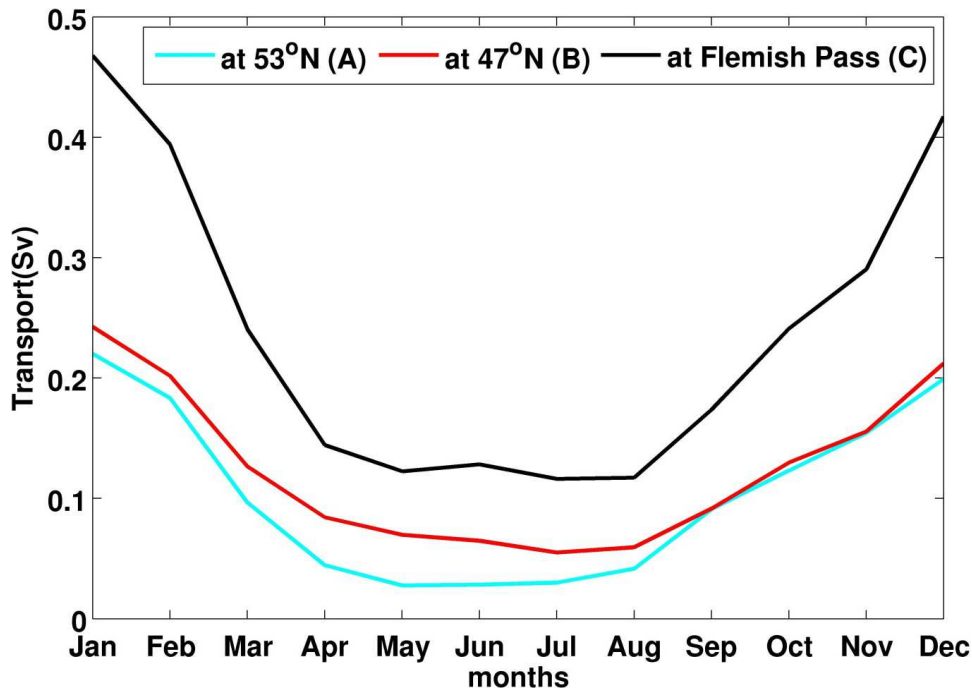


Figure 3.7: Average seasonal cycle of the model's Ekman transport (positive to the south) for each of the three sections over the period 1960-2009.

Nevertheless, the weakened ULSW volume transport through Flemish Pass on seasonal scale shows that a minimum transport at Flemish Pass follows after two months from the maximum southward transport at 47°N in the DWBC. The correlation coefficient is negative $r=-0.88$ and it shows that the variability of volume transports at Flemish Pass with the DWBC at 53°N and 47°N are out of phase. In order to gain further insight into the dependence of the southward transport variability at 47°N from the upstream fluctuations, the lagged by 2 months ULSW transport anomaly at 53°N is subtracted from the anomaly at 47°N , namely as residual part. The climatological seasonal cycle transport variability of the residual does not depict any significant signal with the seasonal cycle of the transport variability at Flemish Pass ($r=0.38$) and at 47°N ($r= -0.52$). A minimum of the residual transport variability is in between the minimum of the volume transport in the DWBC at 47°N and 53°N .

A further examination of the seasonal cycle is provided by the computation of the decomposed transport using the equation 2.1 as described in section 2.2. The climatological seasonal cycle at the examined sections of each term of the equation is presented in Figure 3.9. In Figure 3.9 (A) the volume transport with a constant depth (relative to

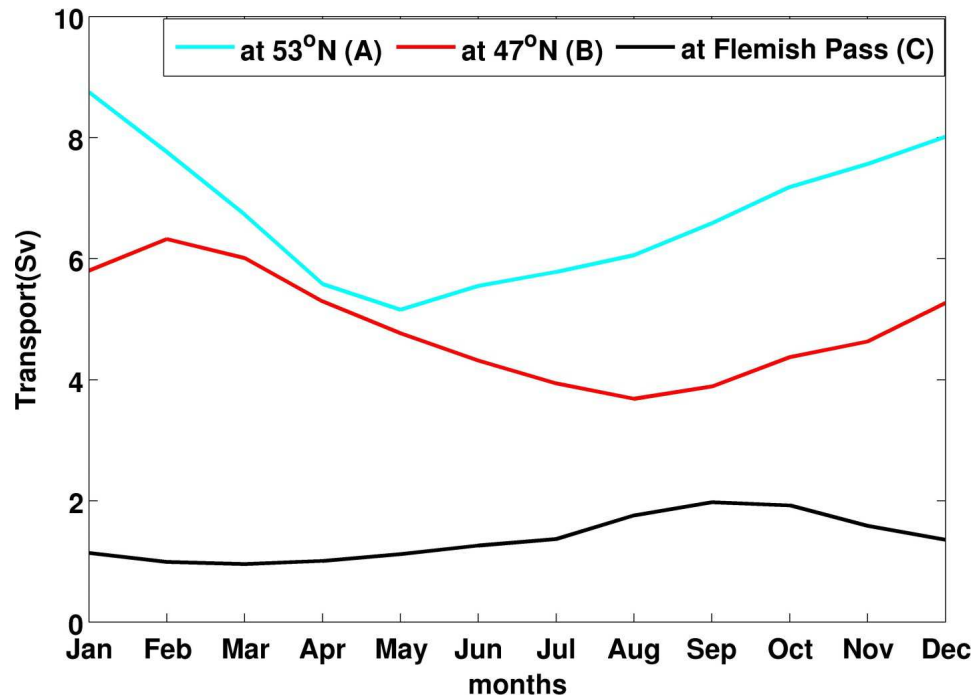


Figure 3.8: Same as Figure 3.6 but for the case of the ULSW transport variability in the density layer ($\sigma_\theta = 27.68 - 27.74 \text{ kg/m}^3$).

3. GENERAL CIRCULATION OF THE STUDY REGION

the velocity's variance) is presented and in Figure 3.9 (B) the volume transport with a constant velocity (relative to the layer thickness variance) is presented. The seasonal cycle of the volume transport with constant velocity coincides with the seasonal cycle of the ULSW volume transport (relative to the dependence from the velocity and layer thickness variance at each section). In contrast, the seasonal cycle of the volume transport with a constant layer thickness at each section, where the velocity varies, does not present a strong amplitude. Consequently, the volume transport variability seems to be influenced by the layer thickness at the seasonal timescale.

The seasonal cycle of the ULSW volume transport in the DWBC at 47°N and 53°N is determined by the seasonal cycle in the surface layer (Figures 3.6 and 3.8) at the same section according to the correlation coefficient between them ($r=0.78$ and $r=0.75$, respectively). The seasonal cycle of the ULSW volume transport at Flemish Pass, on the contrary, is not influenced by the seasonal cycle in the surface layer at Flemish Pass. Consequently, other physical mechanisms contribute to the variability of the ULSW volume transport at Flemish Pass. Prior to the detailed analysis of the temporal evolution the ULSW volume transport variability at interannual timescale, the estimation of the volume transport in the surface layer as well as the contribution of the changes of the layer thickness in the ULSW density layer to the temporal evolution of the ULSW volume transport at the examined sections have been investigated (Chap. 4).

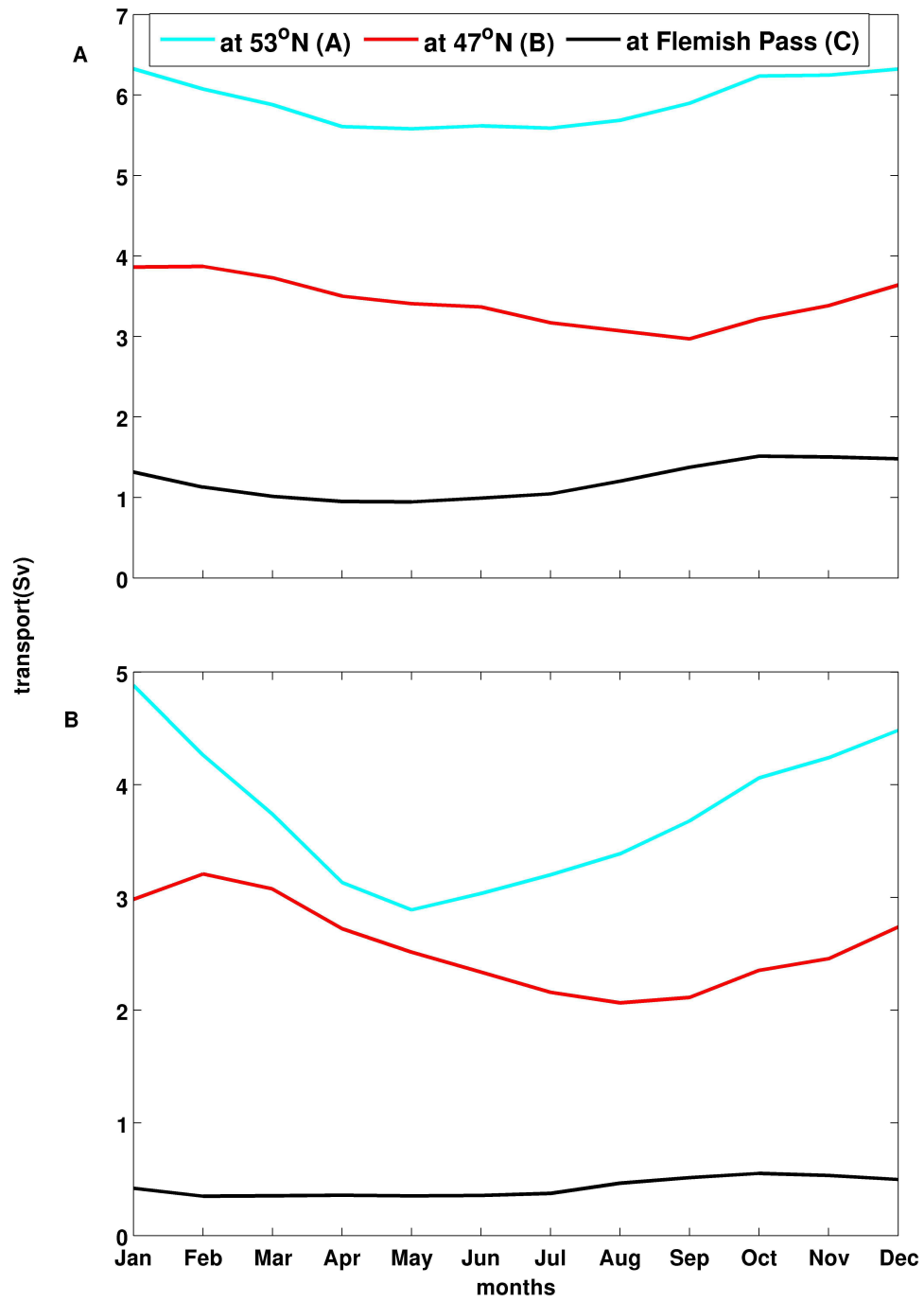


Figure 3.9: Average seasonal cycle of the ULSW volume transports (positive to the south) (A) with constant layer thickness and (B) with constant velocity for each section over the period 1960-2009.

3. GENERAL CIRCULATION OF THE STUDY REGION

Chapter 4

Changes of the transport variability in the surface layer and in the layer thickness variability

In the first part of this chapter, the impacts of the temporal evolution of the volume transports variability at the examined sections in the surface layer to the ULSW volume transport and the effects of the other physical mechanisms in the surface layer on interannual timescale are presented. The quantification and qualification analysis of the results is based on the rcc method; this method has been applied between the transport variability in the surface layer and the other physical mechanisms as well as between the transport variability in the surface layer and the transport variability in the ULSW density layer at interannual timescale. In the second part of this chapter, the contribution of the changes of the layer thickness in the ULSW density layer to the ULSW volume transport variability at the interannual timescale is presented. Due to the unclear contribution of the changes of the layer thickness in the ULSW density layer to the temporal evolution of the ULSW volume transport, the decomposed transport is computed. The decomposed transport variability in the ULSW density layer at interannual timescale has been investigated with respect to the changes of the layer thickness and the changes of the velocity variance.

4. CHANGES OF THE TRANSPORT VARIABILITY IN THE SURFACE LAYER AND IN THE LAYER THICKNESS VARIABILITY

4.1 Volume transport variability in the surface layer at interannual timescale

In order to examine the temporal evolution of the ULSW volume transport variability at the selected sections on interannual timescale (a band-pass filter, centered at 3 years with cut off period of 18-56 months is applied), several physical mechanisms have been taken into consideration. Thus, the effects of the temporal variability in the surface layer on the temporal evolution of the ULSW volume transport are examined. It should be noticed that wind driven ocean circulation is strongest in the surface layer (e.g Ekman transport or NAO). The latter is confirmed in section 3.3, where the strong transport of the water mass in the surface layer at the LC is positively correlated with the Ekman transport on the seasonal timescale at the study sections. The variability of the ULSW volume transport is similar than the variability of the volume transport in the surface layer (Figure 4.1 A, B, C). The low and positive correlation over the whole study period between the transport variability in the surface layer and the transport variability of the ULSW layer at each section at interannual timescale lead me to apply the rcc method between these two transport variabilities. Furthermore, in order to determine the temporal evolution of volume transport variability in the surface layer, the rcc method is also applied between these transports and other physical mechanisms.

The rcc between the transport variability in the surface layer and the other examined parameters is only applied to the three examined sections but a significant correlation is only present at 47°N and at Flemish Pass as shown in Figures 4.2 and 4.3. Due to the high and significant correlation between the variability in the surface layer (for both sections) and the NAO index, it seems that the transport variability in the surface layer is influenced more by the large scale atmospheric forcing (NAO index) than by the local atmospheric forcing (Ekman transport).

The results show that the variability in the surface layer plays a role on the temporal evolution of the ULSW volume transport variability at the interannual timescale. More specifically, during the period from 1965 to 1973, the ULSW transport variability at Flemish Pass coincides (positive correlation, explained by 49 % of the total variance) with the transport variability in the surface layer at Flemish Pass. The contribution of the subpolar average transport variability to the transport variability in the surface layer is presented by the positive correlation between these two parameters. Furthermore, the role of the atmospheric large scale influence (NAO) on the volume transport variability in the surface layer is depicted in Figure 4.2 A. During the period from 1965 to 1973, the rcc between the transport variability in the surface layer and the NAO

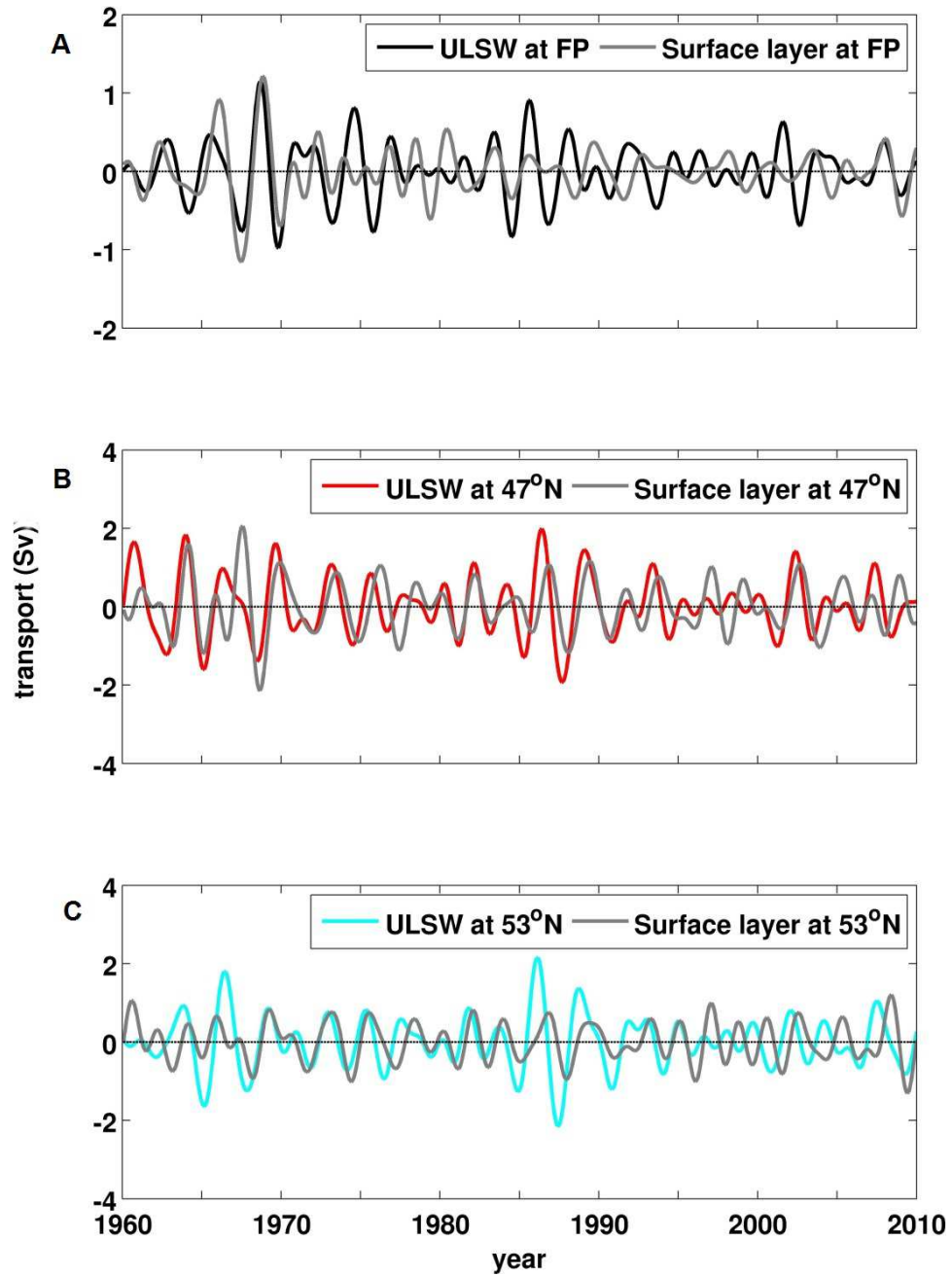


Figure 4.1: Band-pass filtered (from 18 to 54 months) ULSW transport anomalies at the three selected sections A) at Flemish Pass (black), B) at 47°N (red) and C) at 53°N (cyan) at the DWBC and the transport anomalies in the surface layer (gray lines) at the same sections.

4. CHANGES OF THE TRANSPORT VARIABILITY IN THE SURFACE LAYER AND IN THE LAYER THICKNESS VARIABILITY

depicts a negative significant correlation, meaning that enhanced southward transport at Flemish Pass occurs during negative zonal wind anomalies in the Atlantic due to the negative sign of the NAO as shown in Figure 4.2 A. As a conclusion, the transport variability in the surface layer could be dominated by the barotropic structure.

The influence of the local atmospheric forcing (Ekman transport) on the transport variability in the surface layer at Flemish Pass (Figure 4.2 B) is examined. The correlation between the Ekman transport and the volume transport in the surface layer at Flemish Pass gives a positive significant signal for the period from 1970 to 1973. In this period, atmospheric changes govern the transport variability through the Passage. Additionally, the subpolar averaged transport is positively correlated (explained by 49 % of the total variance) with the volume transport in the surface layer during the period from 1965 to 1972, showing a relatively high contribution to the evolution of the volume transport in the surface layer. Consequently, the barotropic mode is primarily responsible for the transport variability in the surface layer during this period.

Meanwhile, the rcc between the variability in the surface layer at 47°N and the NAO index shows a slightly positive correlation most of the time. In order to investigate the behavior of the volume transport in the surface at 47°N , the rcc method between the volume transport in the different density layers and the atmospheric forcing (NAO and Ekman transport, Figures 4.3 A, B) is applied. The large scale atmospheric forcing (NAO) influence (positive correlation) the temporal evolution of the transport variability in the surface layer (Figure 4.3 A, explained by 42 % of the total variance) for the period from 1965 to 1973. At this period (1965-1973), the behavior of the transport variability in the surface layer at 47°N is in agreement with the ULSW volume transport at 47°N (Figure 4.3 D), showing a barotropic mode of the transport variability at 47°N in the surface layer during this period. The subpolar averaged transport has a low contribution to the transport variability at 47°N (25 % of the total variance) during the period from 1972 to 1974.

Another parameter which governs the transport variability in the surface layer is the Ekman transport. The rcc between the Ekman transport and the volume transport variability in the surface layer presents a small negative correlation (Figure 4.3 B) for the period from 1970 to 1975. However, the ULSW formation rate and the variability of the subpolar average transport (as described in section 2.3.1, see also Figure 2.5 C and E) are linked to the atmospheric changes. The correlation between the transport variability in the surface layer and the ULSW formation rate and the subpolar averaged transport is inconclusive, due to the different properties of the water masses. The rccs between the transport variability in the surface layer and the ULSW transport

variability at Flemish Pass and at the east part of Flemsh Cap (at 47°N) (Figures 4.3 and 4.2D) do not depict a high significant signal at interannual timescale.

The ULSW transport variability is not influenced so much by changes in the transport variability in the surface layer at interannual timescale. The explanation of the

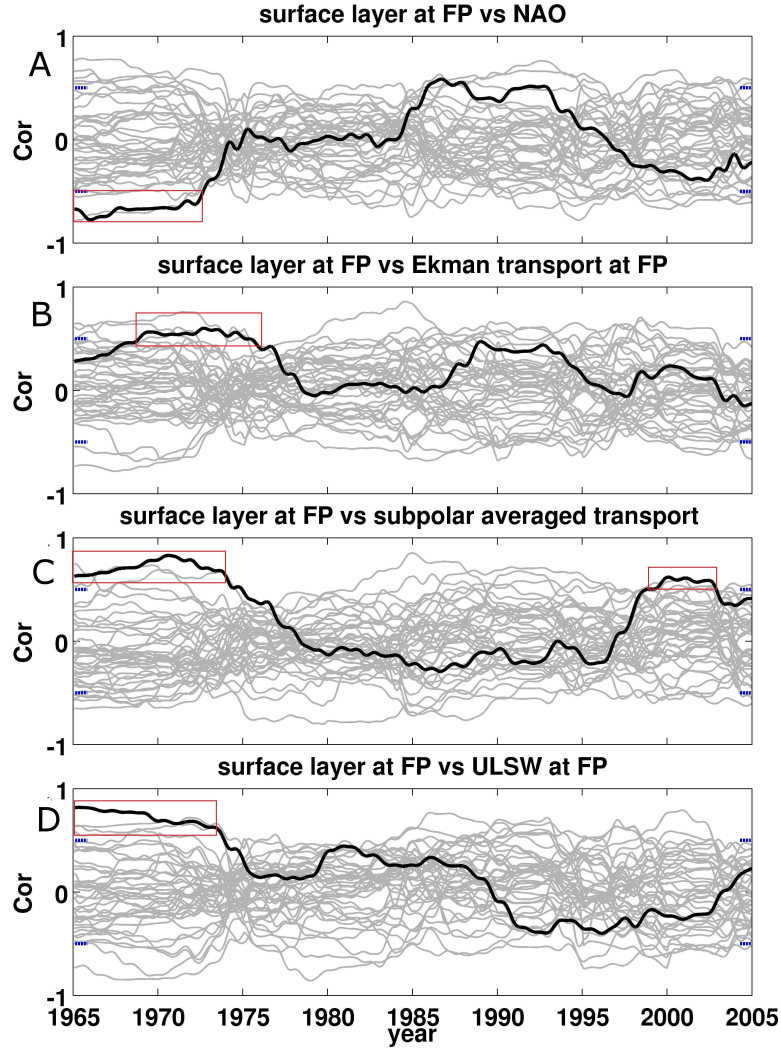


Figure 4.2: Coefficients of the running correlation (Cor; black lines) between the band-pass filtered time series of the NAO index, the Ekman transport at Flemish Pass, the subpolar averaged transport and volume transport in surface layer ($\sigma_\theta < 27.68 \text{ kg/m}^3$) at Flemish Pass. Gray lines correspond to running correlations obtained from the bootstrap method (repeated 20 times). The blue ticks are the significance limits of the correlation according to the p-value ($r=0.5$, 95 % confidence level) and red boxes mark periods of significant correlations between the tested parameters.

4. CHANGES OF THE TRANSPORT VARIABILITY IN THE SURFACE LAYER AND IN THE LAYER THICKNESS VARIABILITY

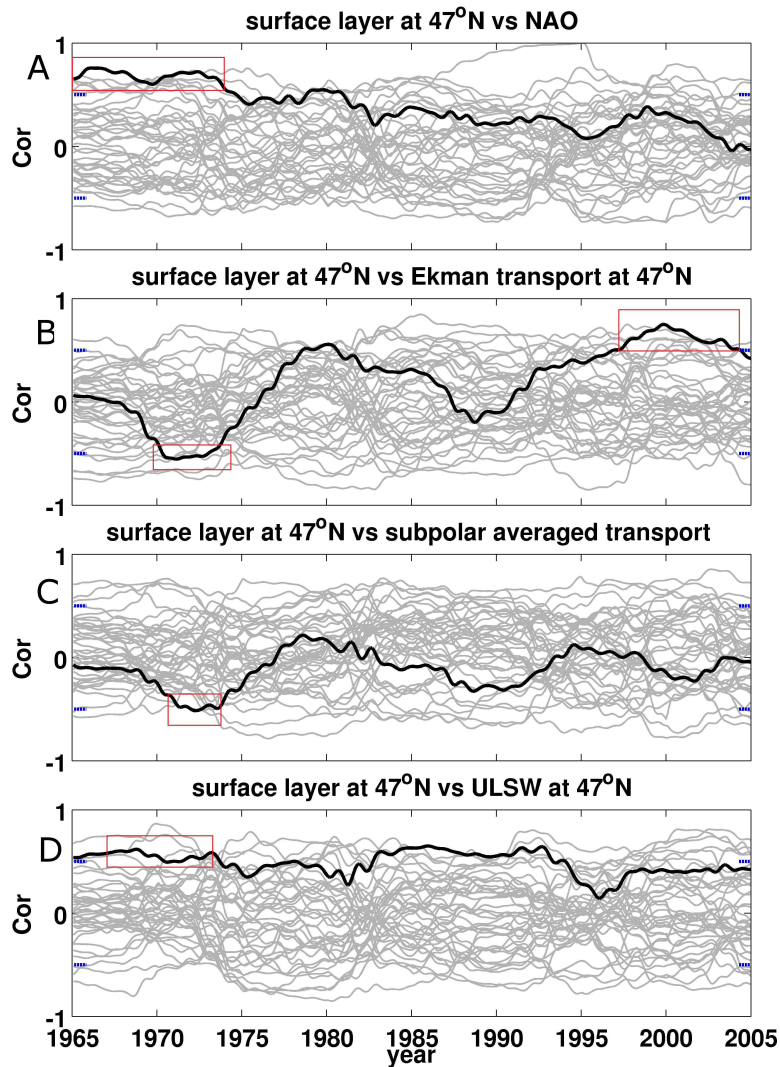


Figure 4.3: Same as Figure 3.4 but for the case of the volume transport in the surface layer at 47°N.

ULSW volume transport evolution is provided by the connection between the ULSW transport variability and other physical mechanisms, which is presented in the following chapter. The same methodology was followed for the analysis of the volume transport variability in the surface layer at 53°N (not shown). The results do not show any significant signal, except for the period from 1965 to 1975, where the ULSW volume transport and volume transport in the surface layer at 53°N present low but positive correlation (approximately 42% of the total variance). The evolution of the volume transport variability in both sections at Flemish Pass and at 47°N can be attributed

to the atmospheric variance, especially during the period from 1965 until 1970.

4. CHANGES OF THE TRANSPORT VARIABILITY IN THE SURFACE LAYER AND IN THE LAYER THICKNESS VARIABILITY

4.2 Relationship between the ULSW layer thickness variability and the ULSW volume transport variability at interannual timescale

As mentioned in section 2.2, the changes of the layer thickness and the changes of the velocity's variance are taken into account for the computation of the volume transport. A study which was based on the comparison between observation estimates and model estimates [Scholz et al., 2014], suggests that the changes of the ULSW layer thickness is associated with the changes of the NAO index variability. Consequently, the transport variability in the ULSW density layer is influenced by the changes of the layer thickness. However, a comparison between the variability of the ULSW layer thickness and the ULSW volume transport at each section in this study does not give any significant signal (low correlation coefficient).

The behavior of the layer thickness at interannual timescale can be explained by the properties of the model used. More specifically, the model is a c-grid model and the u and v velocity components' values, which are used for the volume transport computation, are at the edges of each grid box. Moreover, the values of the temperature and salinity, which are used for the definition of the density layer, are at the center of each grid box. For the computation of the layer thickness, the boundaries on x-axis are based on the position of the maximum of the average velocity. The boundaries on x-axis of the velocity's maximum position do not coincide with the boundaries on x-axis for the computation of the volume transport (as described in section 2.2), due to the properties of the model. As a result, the variability of the layer thickness at each section seems to be similar (Figure 4.4) over the study period, signifying that the ULSW volume transport variability is independent of the variability of the layer thickness at the same timescale (which is not widely accepted).

An alternative approach to investigate the influences of the layer thickness variability on the volume transport in the ULSW density layer is to compute the transports based on the equations 2.1 and 2.2 as described in section 2.2.

In Figure 4.5 A, B and C, the temporal evolution of the volume transports variability (T_{vel} . (2.1) and T_{ρ} (2.2)) as well as the sum of these two transports (A. transport with constant layer and B. transport using the average velocity over the study period and C. the sum of the aforementioned transports) at each section is displayed. In order to examine the transport variability spectral analysis is applied to the transports, showing a significant peak corresponding to seasonal and interannual timescales.

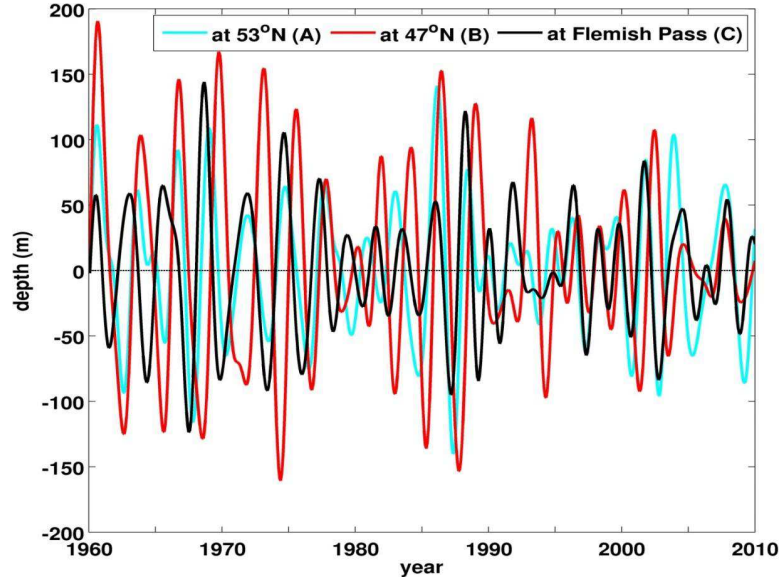


Figure 4.4: Band-pass filtered (from 18 to 54 months) ULSW layer thickness anomalies for the sections A, B, C shown in Figure 3.1: at 53°N (cyan), at the DWBC at 47°N (red) and at Flemish Pass (black).

Subsequently, a band-pass filter (centered at 3 years) is applied to the transports (Figure 4.6) showing the temporal evolution of the anomalies at interannual timescale. The transports $T_{vel.}$ (2.1) and T_{ρ} (2.2)) are compared to the total ULSW volume transport (Figure 4.4) at interannual timescale at the selected sections. The aforementioned transports at 53°N as well as the sum of these transports show the strongest variability (Figure 4.5 C) compared to the sum of the transports variability at the other two sections. The sum of the transports (relative to the layer thickness (Figure 4.6 A) and velocity (Figure 4.6 B)) represents a similar variability with the total ULSW volume transport (relative to the computation of the volume transport as described in section 2.2) at each section (Figure 5.2). A positive and high correlation (approx. $r=0.90$) appears between the transport of the layer thickness variance and the transport of the velocity variance at each section. In order to investigate how the changes of the layer thickness affect the ULSW volume transport variability at each section, a comparison is made between the total ULSW volume transport at Flemish Pass and the volume transport variability with a constant velocity at each section, where the layer thickness varies over the study period. The results show a positive and high correlation of about $r=0.9$. The same positive and high correlation occurs between the total ULSW volume transport and the volume transport with a constant depth, where

4. CHANGES OF THE TRANSPORT VARIABILITY IN THE SURFACE LAYER AND IN THE LAYER THICKNESS VARIABILITY

the velocities vary in time, at each section.

A positive and high correlation appears between the total ULSW volume transport and the volume transport of the transports $T_{vel.}$ and T_{ρ} at Flemish Pass, showing the dependence of the layer thickness as well as of the velocity's variance on the ULSW volume transport. In the DWBC at 47°N and at 53°N , the volume transport relative to the layer thickness variance contribute more to the total ULSW volume transport than the volume transport relative to the velocity's transport. It is remarkable that the correlation coefficient between the sum of the transports $T_{vel.}$ (2.1) and T_{ρ} (2.2) at the Flemish Pass section with the the sum of the transports at 53°N is positive at zero lag, while the correlation coefficient of the sum of the transports between the sections at 47°N and at 53°N shows a lag of 2 months with $r=0.63$. Based on this result, it appears that the propagating signal of the sum of the transports follows the short pathway through Flemish Pass by the water mass transport from the north to the south. The amplitude of the sum of the unfiltered transports is larger at 53°N and at 47°N (9.1 Sv and 8.2 Sv, respectively) compared to the amplitude of the sum of unfiltered transport at the Flemish Pass section (3.6 Sv).

The volume transport with constant layer at each section does not depict strong variability but it presents a strong seasonal cycle as shown in section 3.3, especially from the beginning of the study period until 1985. Thus, the transport variability is not essentially influenced so much by the velocity's variance. However, the volume transport using average velocity presents stronger variability at 53°N (6.75 Sv) and at 47°N (4.5 Sv) than the transport variability at Flemish Pass (1.7 Sv) using the unfiltered timeseries. Thus, the volume transport variability in the DWBC at 53°N and at 47°N in the ULSW layer is mainly influenced by the changes of the layer thickness compared to the volume transport variability through Flemish Pass.

At interannual timescale (Figure 4.6), the amplitude of the volume transport variability in the three examined cases is similar to changes of the variability at each section. The amplitude of the sum of the transports is similar at each section (range: at $53^{\circ}\text{N}=2.4\text{ Sv}$, at $47^{\circ}\text{N}= 2.7\text{ Sv}$ and at Flemish Pass = 1.4 Sv). Additionally, the variability of the volume transport at Flemish Pass (Figure 4.6 C) is stronger than the transport variability in the DWBC at 53°N and at 47°N and vice versa. It is obvious that the strong volume transport variability is maintained by the changes of the layer thickness compared to the changes of the velocity's variance at interannual timescale, but the physical mechanisms which determine the layer thickness changes at each section are not the same. It appears from the high and positive correlation coefficient of the decomposition transports between the sections that the downstream fluctuations

(considering the variability at Flemish Pass) lead by 3 months the upstream fluctuations (considering the variability at 53°N), which is not widely accepted.

The interpretation of the sum of the transports indicates that the effects of the layer thickness variability are not associated directly with the ULSW volume transport variability at interannual timescale. This leads me to turn my attention to other physical mechanisms (e.g. the atmospheric forcing or the rate of the ULSW formation), that contribute to the ULSW volume transport variability at interannual timescale (Chapter 5).

Nevertheless, it is remarkable that during the period from 1963 to 1966 the strongest variability of the decomposed transport is observed in the DWBC at 47°N . In the same period, the volume transports with constant depth and average velocity also present strong variability at 47°N , which can be attributed to the influence of the local or large scale wind forcing. In addition, during the period from 1984 to 1988 a strong variability of the decomposed transport as well as of the transport of the layer thickness variance appears at each section, which is probably due to the NAC's position shifts.

4. CHANGES OF THE TRANSPORT VARIABILITY IN THE SURFACE LAYER AND IN THE LAYER THICKNESS VARIABILITY

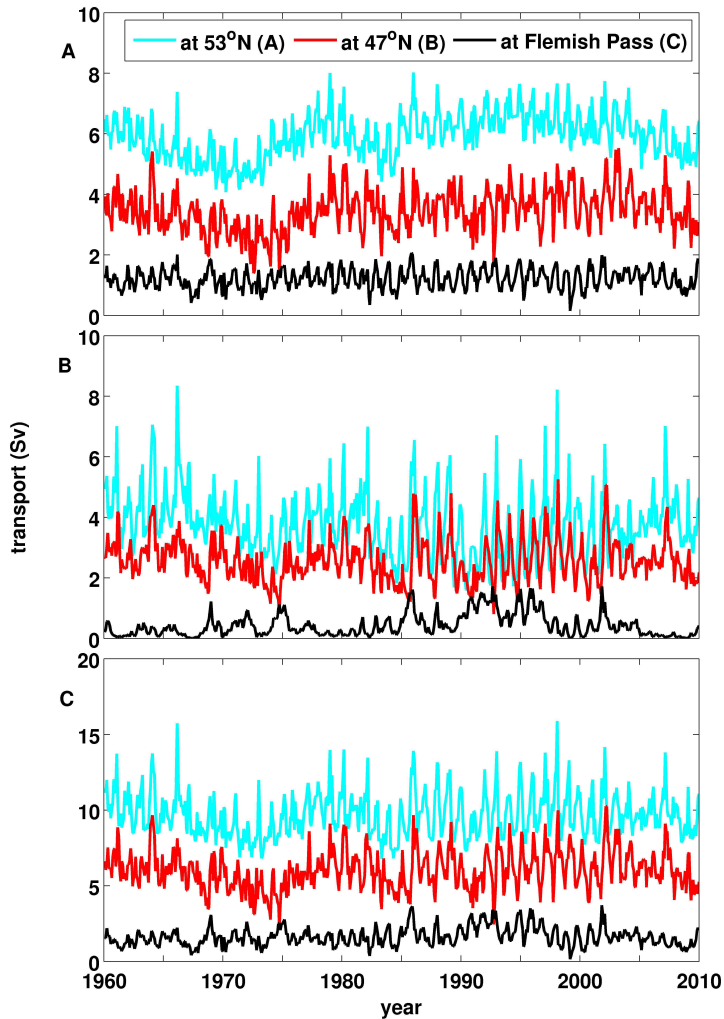


Figure 4.5: Unfiltered ULSW Volume transports for the Sections A, B, C at 53°N (cyan), in the DWBC at 47°N (red) and at Flemish Pass (black) using only the negative velocity. A) (top of the figure) the volume transport ($T_{vel.}$) using constant layer (from the mean depth of the upper boundary to the mean depth of the low boundary of the ULSW density layer) at each section, B) (in the middle of the figure) the volume transport (T_{ρ}) using the average velocity and C) (the bottom of the figure) the sum of A+B at each section over the study period.

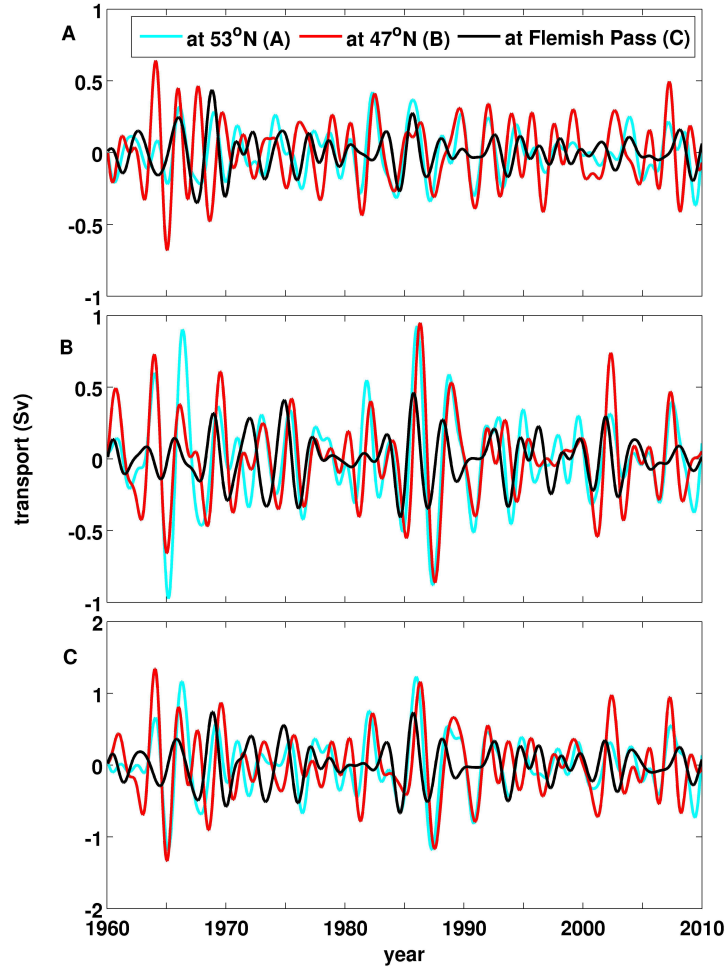


Figure 4.6: Band-pass filtered (from 18 to 54 months) of the volume transport anomalies at 53°N (cyan), at 47°N (red) at the DWBC and at Flemish Pass (black). A) (top of the figure) the volume transport ($T_{vel.}$) using constant layer (from the mean depth of the upper boundary to the mean depth of the low boundary of the ULSW density layer) at each section, B) (in the middle of the figure) the volume transport (T_{ρ}) using the average velocity and C) (the bottom of the figure) the sum of A+B at each section over the study period.

4. CHANGES OF THE TRANSPORT VARIABILITY IN THE SURFACE LAYER AND IN THE LAYER THICKNESS VARIABILITY

Chapter 5

Estimation of the ULSW volume transport

In this chapter, the temporal evolution of the ULSW volume transport at interannual timescale is presented. The main focus is on the export of the ULSW from the north to the south and how the temporal evolution is linked to several physical mechanisms. The results of this chapter are already published by Varotsou et al.,[2015].

5.1 ULSW volume transport variability

For a better understanding of the changes of the ULSW transport variability, the volume transport every 2° (Figure 5.1) from the south to the north is computed using the meridional and the zonal velocity. A first view of the results shows that the similarity of variability along the path of the DWBC is a persistent feature. An analysis of volume transport variability at several sections (every 2° in latitude) in the DWBC between 53°N and 47°N revealed the same behavior of anomalies for all sections.

The correlation coefficient between the anomalies at 53°N and the anomalies around Flemish Cap are depicted in Table 5.1. The propagating signal of the ULSW volume transport follows the long pathway from the section at 53°N to Flemish Pass. For this reason, the analysis of the volume transport at several sections around Flemish Cap is necessary. According to the correlation coefficient (Table 5.1), when the flow reaches at 49°N , it divides into two branches (inshore branch: flow goes through Flemish Pass and the offshore branch: flow goes around Flemish Cap), the area around Flemish Cap is divided into four sections. The further analysis of the ULSW volume transport at the selected sections around Flemish Cap aims to investigate the behavior of the ULSW

5. ESTIMATION OF THE ULSW VOLUME TRANSPORT

volume transport and the physical mechanisms, which contribute to the evolution of the transport variability at the studied sections.

Furthermore, the four sections around Flemish Cap are 1st at the Northern Part of Flemish Cap using the zonal velocity for the volume transports computation, 2nd East of Flemish Cap using the meridional velocity for the volume transports computation, 3rd at the southern part at Flemish Cap using the zonal velocity for the volume transports computation and 4th at Flemish Pass using the meridional velocity for the volume transports computation. It should be mentioned that the transport variability of the

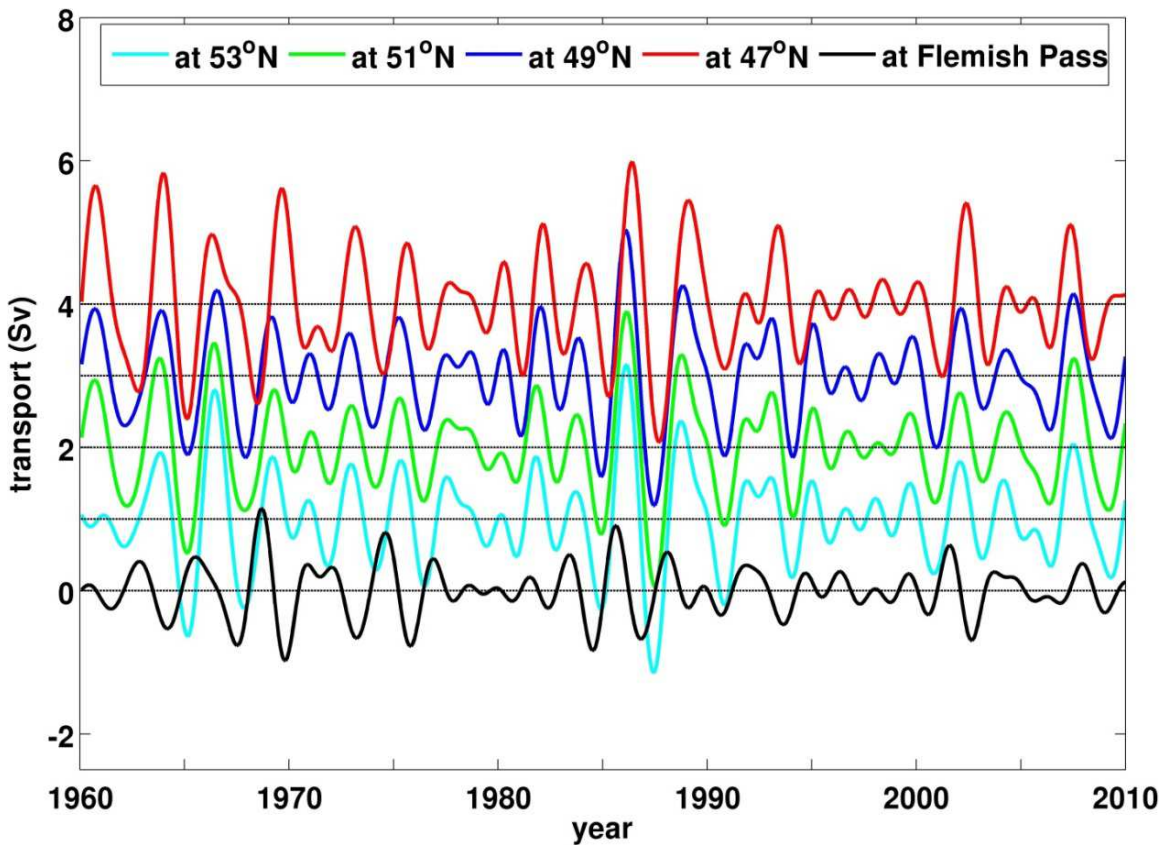


Figure 5.1: Band-pass filtered (from 18 to 54 months) ULSW transport anomalies for the Sections from 53°N (cyan) to 47°N (red) (an offset of +1 Sv, +2 Sv, +3 Sv and +4 Sv was added to the transport anomalies from 53°N to 47°N, respectively) in the DWBC every 2° and at Flemish Pass (black, without adding an offset to the transport anomaly at Flemish Pass). Dashed black lines are the virtual zero line after adding an offset.

sections	47°N	53°N	northern part	southern part
Flemish Pass	R=-0.7 3 months	R=-0.65 8 months	R=-0.8 4 months	R=-0.53 5 months
47°N	x	R=0.78 3 months	R=0.95 0 months	R=0.71 0 months
northern part	x	x	x	R=0.72 0 months

Table 5.1: Correlation coefficient of the band pass filtered ULSW volume transport anomalies between the selected sections

first 3 sections has a similar behavior and the variability at Flemish Pass presents different behavior at interannual timescale.

The band-pass filtered volume transport anomalies are presented in Figure 5.2. Variations in the DWBC at 53°N and at 47°N are of similar magnitude (about 2 Sv in amplitude), whereas the amplitude of the anomalies in Flemish Pass is smaller in general (about 0.7 Sv). The temporal evolution of ULSW transport anomalies in the DWBC at 47°N follows (with a lag of 3 months and correlation $r=0.78$) the evolution of the ULSW transport at 53°N. In contrast, the temporal evolution of the ULSW transport at Flemish Pass has a different behavior; the correlation with the 53°N anomalies is low and out-of-phase at the expected lag of 3 months ($r=-0.3$). Better correlations are found when a lag of 8 months is applied ($r=-0.65$), but the additional 5 months compared to the DWBC pathway lack an advective explanation, as the covered distance is very similar. Additionally, the correlations are negative, therefore not pointing to signal propagation, which must result in positive correlations. Hence, on interannual timescales transport fluctuations propagate downstream along the DWBC path, but the ULSW transport variability in Flemish Pass is obviously governed by different processes. Furthermore, an out-of-phase correlation is apparent between the DWBC at 47°N and Flemish Pass ($r=-0.7$, lag=3 months), indicating delayed flow compensation; when the ULSW transport in the DWBC is strong, the flow in Flemish Pass experiences a delayed minimum in ULSW transport.

The correlations given above are obtained from taking the total time series into account, but when looking closely at Figure 5.2, phase shifts are present, which reduce the correlation. Flemish Pass is mostly out-of-phase with the other two time series, but for some years, the variations are in phase (e.g. 1992). Causes for the different behavior of the anomalies in Flemish Pass as well as the different phases are investigated in the following sections.

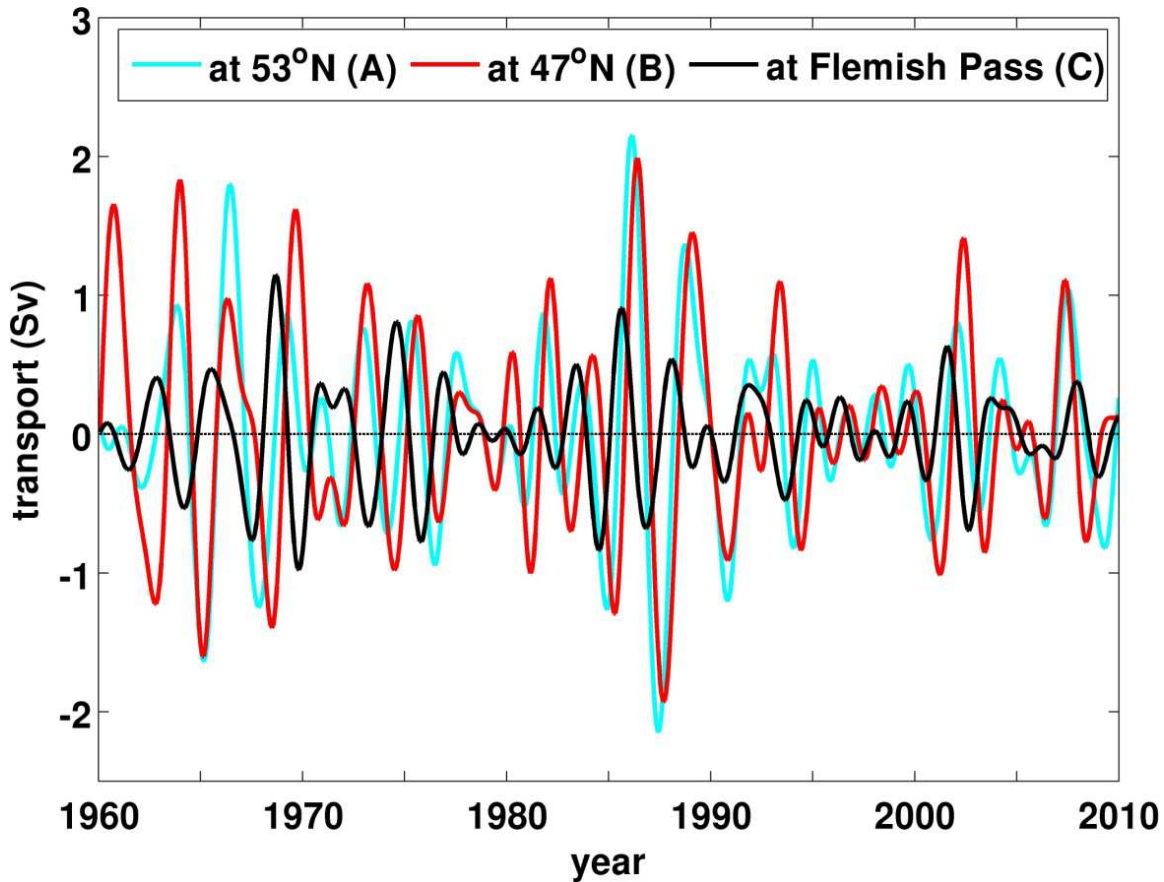


Figure 5.2: Band-pass filtered (from 18 to 54 months) ULSW volume transport anomalies for the Sections A, B, C of Figure 3.1: at 53°N (cyan), in the DWBC at 47°N (red) and at Flemish Pass (black) [Varotsou et al., 2015].

5.2 Causes of the temporal variability of the ULSW transports at 47°N

In order to understand the different behavior of the transport anomalies in Flemish Pass and in the DWBC, the contributions of different processes to the variability on both sections at 47°N (Sections B and C in Figure

Firstly, the running correlations were applied with respect to testing the dependence of ULSW transports at 47°N on upstream fluctuations (Figure 5.4 A). As expected from the results of the classical correlations previously discussed, upstream fluctuations dominate the DWBC flow during the whole period of investigation. When a time lag of 3 months is applied to the transport at 53°N , allowing for the downstream propagation,

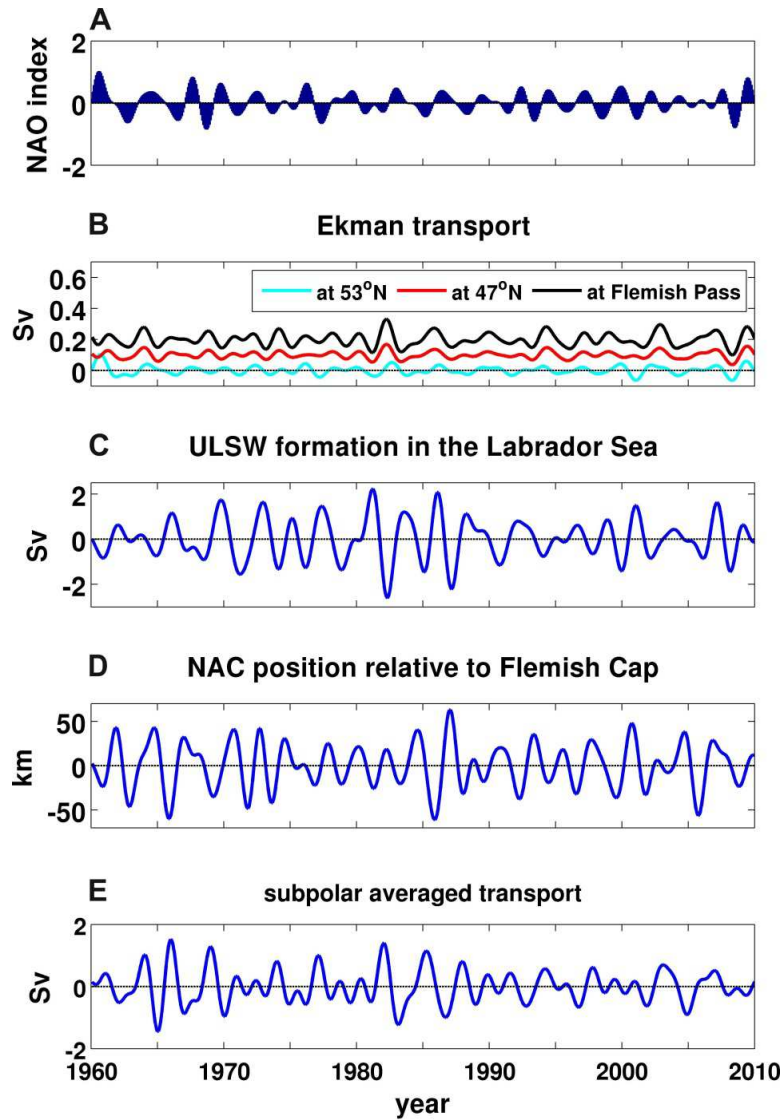


Figure 5.3: Band-pass filtered time series (18-54 months) of the same parameters shown in Figure 2.5: (A) the NAO index; (B) the Ekman transport at 53°N over the slope, at 47°N east of Flemish Cap and at Flemish Pass (an offset of $+0.1\text{ Sv}$ and $+0.2\text{ Sv}$ was added to the latter two for clarity of the subfigure; positive values correspond to southward transport); (C) the rate of the ULSW formation in the Labrador Sea; (D) the NAC position relative to Flemish Cap; and (E) the subpolar gyre averaged transport [Varotsou et al., 2015].

correlations are positive and significant over the study period. The lag corresponds to an average downstream propagation velocity of approximately 7 cm/s . As before, for

5. ESTIMATION OF THE ULSW VOLUME TRANSPORT

Flemish Pass the running correlations with 53°N (not shown) are in anti-phase and only significant for a lag of 8 months.

If the ULSW transport anomaly at 53°N , lagged by 3 months, is subtracted from the respective anomaly at 47°N , the “residual” part of the variability has similar amplitude as the Flemish Pass transport variability. Similarities of this residual with the variability at Flemish Pass occur without a time lag, but they are in anti-phase (Figure 5.4B). Consequently, the part of the DWBC transport at 47°N not related to upstream fluctuations is directly correlated with Flemish Pass, meaning that the apparent different behavior east and west of Flemish Cap is partly a result of dominant ULSW signals travelling along-slope and masking the phase relation east and west of Flemish Cap. The anti-phase between the residual and Flemish Pass points to the possibility of flow compensation; when the DWBC is strong, the flow through Flemish Pass is weak and vice versa. With this connection, changes in the circulation of the Newfoundland Basin (like migrations of the NAC position) can have impacts on the Flemish Pass flow, as will be discussed below.

Figure 5.5 presents the coefficients of the running correlation (at zero lag if not stated otherwise) between the ULSW volume transport anomaly at Flemish Pass and (A) the

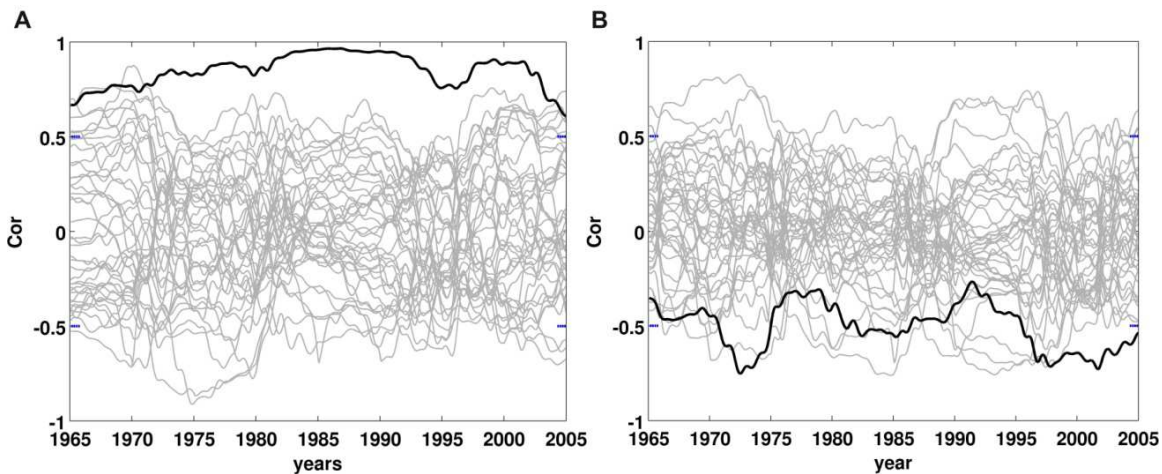


Figure 5.4: Coefficients of the running correlation (Cor; black thick line) between (A) the DWBC band-pass filtered ULSW volume transports at 47°N and at 53°N (the latter lagged by 3 months) and (B) the ULSW transport difference at 47°N minus that at 53°N (the “residual”) and the ULSW transport at Flemish Pass. The grey lines show correlation results from the bootstrap method and the clusters of these depict the areas of non-significant correlation. Blue ticks are the significant correlation limits according to the p-value ($r=0.5$, 95% confidence level) [Varotsou et al., 2015].

NAO index, (B) the Ekman transport, (C) the rate of the ULSW formation lagged by 5 months, (D) the position of the NAC, and (E) the subpolar averaged transport. Figures 5.6 and 5.5 give the corresponding correlations with respect to the transports of ULSW in the DWBC at 47°N and the residual transport at 47°N (calculated as the transport difference $47^{\circ}\text{N} - 53^{\circ}\text{N}$). Significant periods of correlation are highlighted in the figures by red boxes. A time lag was applied to the ULSW formation rate, in order to allow signal propagation by advection towards the latitude of Flemish Cap. Several lags were tested to find the best possible correlation and a lag of 5 months was obtained, corresponding to a reasonable advection time from the central Labrador Sea to the study area.

5. ESTIMATION OF THE ULSW VOLUME TRANSPORT

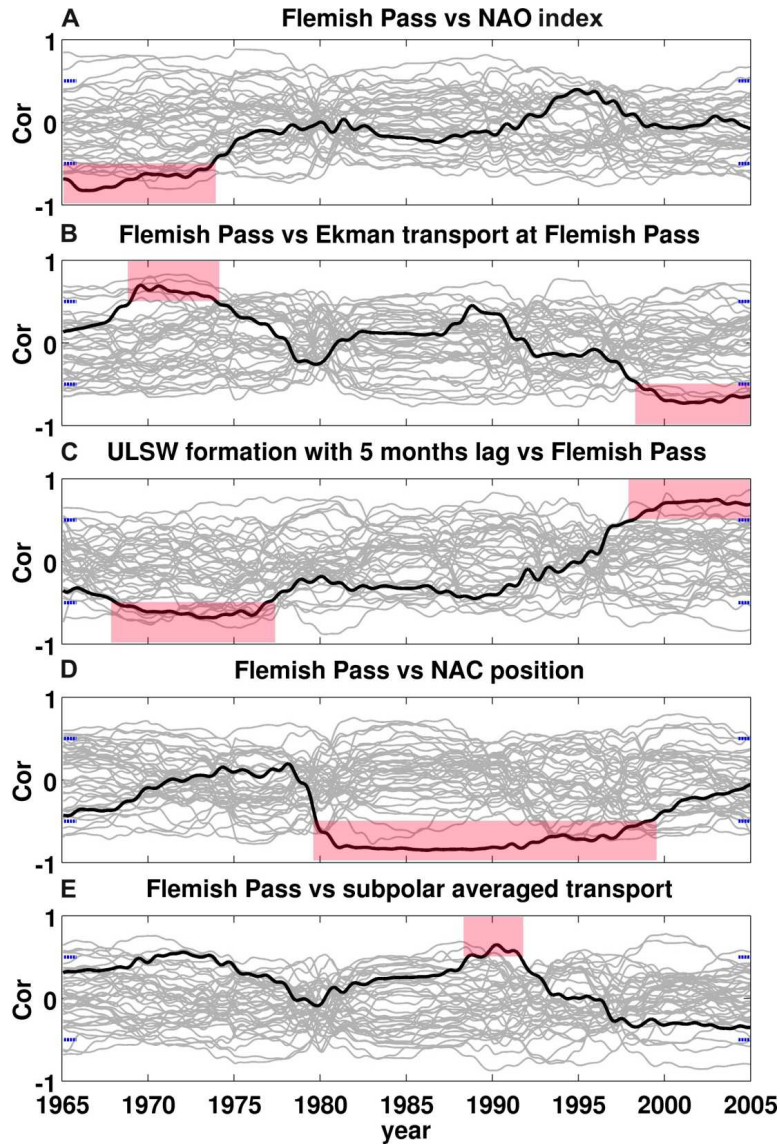


Figure 5.5: Coefficients of the running correlation (Cor; black lines) between the band-pass filtered time series of ULSW volume transport at Flemish Pass and (A) the NAO index, (B) the Ekman transport at Flemish Pass, (C) the rate of ULSW formation in the Labrador Sea (with 5 months lag applied), (D) the NAC's position relative to the Flemish Cap and (E) the subpolar gyre strength index. Gray lines correspond to running correlations obtained from the bootstrap method (20 times repeated). The blue ticks are the significance limits of the correlation according to the p value ($r=0.5$, 95% confidence level). Red boxes mark periods of significant correlations between the ULSW transport at Flemish Pass and the tested parameter [Varotsou et al., 2015].

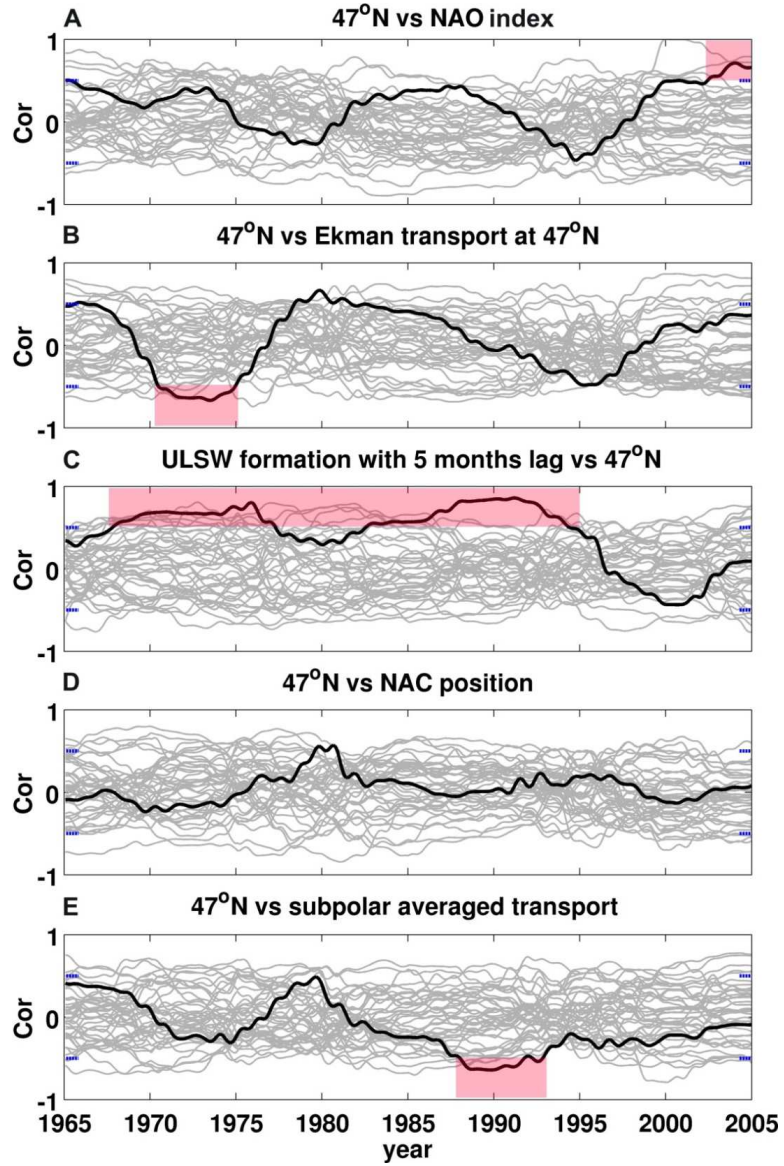


Figure 5.6: Same as Figure 5.5 but for the case of the ULSW transport within the DWBC at 47°N [Varotsou et al., 2015].

5. ESTIMATION OF THE ULSW VOLUME TRANSPORT

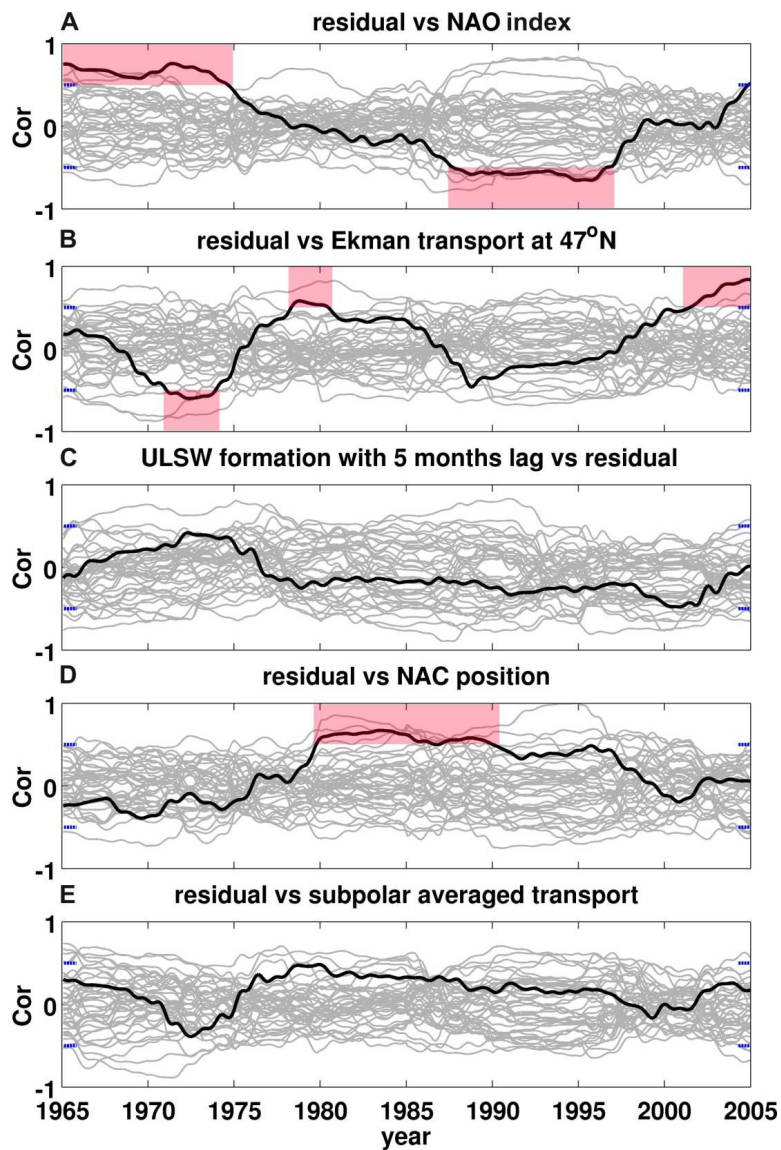


Figure 5.7: Same as Figure 5.5 but for the case of the ULSW transport residual (see text for explanation) within the DWBC at 47°N [Varotsou et al., 2015].

5.3 Processes responsible for ULSW transport variability at Flemish Pass

At the beginning of the study period (from 1965-1973) the effect of large-scale atmospheric changes (represented by the NAO index; explaining 65 % of the total variance) is most important for the fluctuations of the ULSW volume transport at Flemish Pass (Figure 5.5 A). The correlation coefficient between the NAO index and ULSW transport anomalies is negative, meaning that enhanced southward transport at Flemish Pass occurs during negative zonal wind anomalies in the Atlantic (negative events in the filtered NAO, Figure 5.3 A). It is remarkable that the amplitudes of variability at Flemish Pass are highest during this time (Figure 5.2) and that during these years the NAO index is in a persistent negative phase (Figure 5.5 A). In 1968/1969 the impacts of Ekman transport and of the remote forcing from the ULSW production increase above the significance levels as well. In this period the transport variability in the surface layer ($\sigma_\theta < 27.68 \text{ kg/m}^3$) is correlated positively with the transport variability in the ULSW layer. The flow through the passage has a strong barotropic variance. Thus, from the mid-1960s to the mid-1970s atmospheric changes governed the ULSW transport variability at Flemish Pass.

At the end of the study period (1998-2005) the influence of the Ekman transport on the ULSW transport variability in Flemish Pass increases again (Figure 5.5 B), but with an opposite sign (negative correlation). There is less ULSW southward flow through Flemish Pass when the southward Ekman transport is strong. The barotropic transport through the passage is reduced and experiences less variance when compared to the earlier period discussed above. On the other hand, the baroclinic variability is enhanced. The depth of the isopycnal $\sigma_\theta = 27.68 \text{ kg/m}^3$ is now deeper than before and the ULSW transport anomalies are in anti-phase with the surface layer. The negative correlation during this period is consistent with an overall larger importance of the barotropic return flow variability in response to the Ekman transport variability through the whole 47°N section.

Additionally, the remote influence of the varying ULSW formation in the Labrador Sea increased (Figure 5.5 C), but also with opposite sign. This can be explained by the choice of the time lag; 5 months is an average lag, but the actual advection may take a few months more or less. Therefore phase shifts are introduced which are seen in the change of the sign of the correlation. More interestingly, from 1980-1998 the running correlations show a significant contribution of the NAC's position to the transport variability at Flemish Pass ($r=-0.83$, 70 % explained variance). The negative correlation

5. ESTIMATION OF THE ULSW VOLUME TRANSPORT

means that positive transport anomalies occur in Flemish Pass when the NAC is closer to Flemish Cap. Changes in the basin circulation (represented by the subpolar averaged transport) also marginally impact the Flemish Pass variability during this time. In 1998 the influence of the NAC position decreased, and atmospheric forcing again influences Flemish Pass (see above).

5.4 Processes responsible for ULSW transport variability in the DWBC at 47°N

Most of the time during the period 1968-1995 the transport variability at 47°N is determined by the lagged (by 5 months) ULSW formation rate (Figure 5.6 C; explained variance between 40 % and 60 %). Local atmospheric forcing is linked to the transport variability only during a short period from 1970-1975 (Figure 5.6 B). A connection to the band-pass filtered NAO index was found only at the very end of the study period (2003-2005, Figure 5.6 A). The processes representing the circulation (Figure 5.6 D, E) do not depict any strong influence, only for the period from 1988-1993 the subpolar averaged transport has a small contribution (explained variance: 25 %). Remarkably, the effect of the NAC on the DWBC at 47°N is small (no significant correlation) when compared to the upstream variability.

5.5 Residual ULSW transport variability at 47°N

In contrast to the DWBC flow at 47°N the residual variability correlates with similar processes as the transport anomalies in Flemish Pass, but with opposite phase. Firstly, a connection to the NAO is found, but now with positive values (Figure 5.7 A), meaning that positive NAO anomalies induce stronger southward flow. This occurs exactly when at Flemish Pass a reduced southward transport prevails. Secondly, the Ekman transport influences the residual in 1971-1974, when also Flemish Pass is influenced by the local atmosphere.

The residual flow shows the connection with the NAC position as well (Figure 5.7 D). An inshore position of the NAC constrains (reduces) the flow in the DWBC east of Flemish Cap and, therefore, the flow through the Flemish Pass is enhanced. Consequently the volume transport through Flemish Pass increases, giving an anti-phase correlation with the NAC position. This effect is only apparent when considering the residual, not in the total DWBC, which remains correlated with the ULSW formation rate (see above). This is in agreement with Mertens et al. [2014], who also found no

influence of the NAC on the slope part of the DWBC close to Flemish Cap. As a consistency check, the residual transport at 47°N (Figure 5.7 C) does not correlate any more with the ULSW formation rate, which is expected by definition of residual flow (lack of upstream influence).

In order to clarify the role of the NAC's shifts on the ULSW volume transport distribution, the difference of mean eddy kinetic energy in the layer 200 m to 500 m between the period of strong correlation between Flemish Pass and the position of the NAC (1983-1995) and the period when this correlation is absent (1969-1979) is displayed (Figure 5.8). The difference shows an enhancement of the energy levels east of Flemish Cap during the period of large correlation, so it is concluded that eddy activity or strong meandering of the NAC northward flow close to the DWBC reduces the transport in the latter, and the ULSW flow from upstream is "re-directed" into the Flemish Pass, enhancing the transport there. The change of the velocity field between a period of strong NAC influence on Flemish Pass and Cap and weak influence is also illustrated in Figure 5.9, where the difference of the magnitude of the vertically integrated transport in the ULSW layer is shown. Blue colors denote weaker flow in the period of strong NAC influence, while red colors stand for enhanced flow. When the NAC is close to Flemish Cap the DWBC flow is weakened and the flow through Flemish Pass is enhanced.

5. ESTIMATION OF THE ULSW VOLUME TRANSPORT

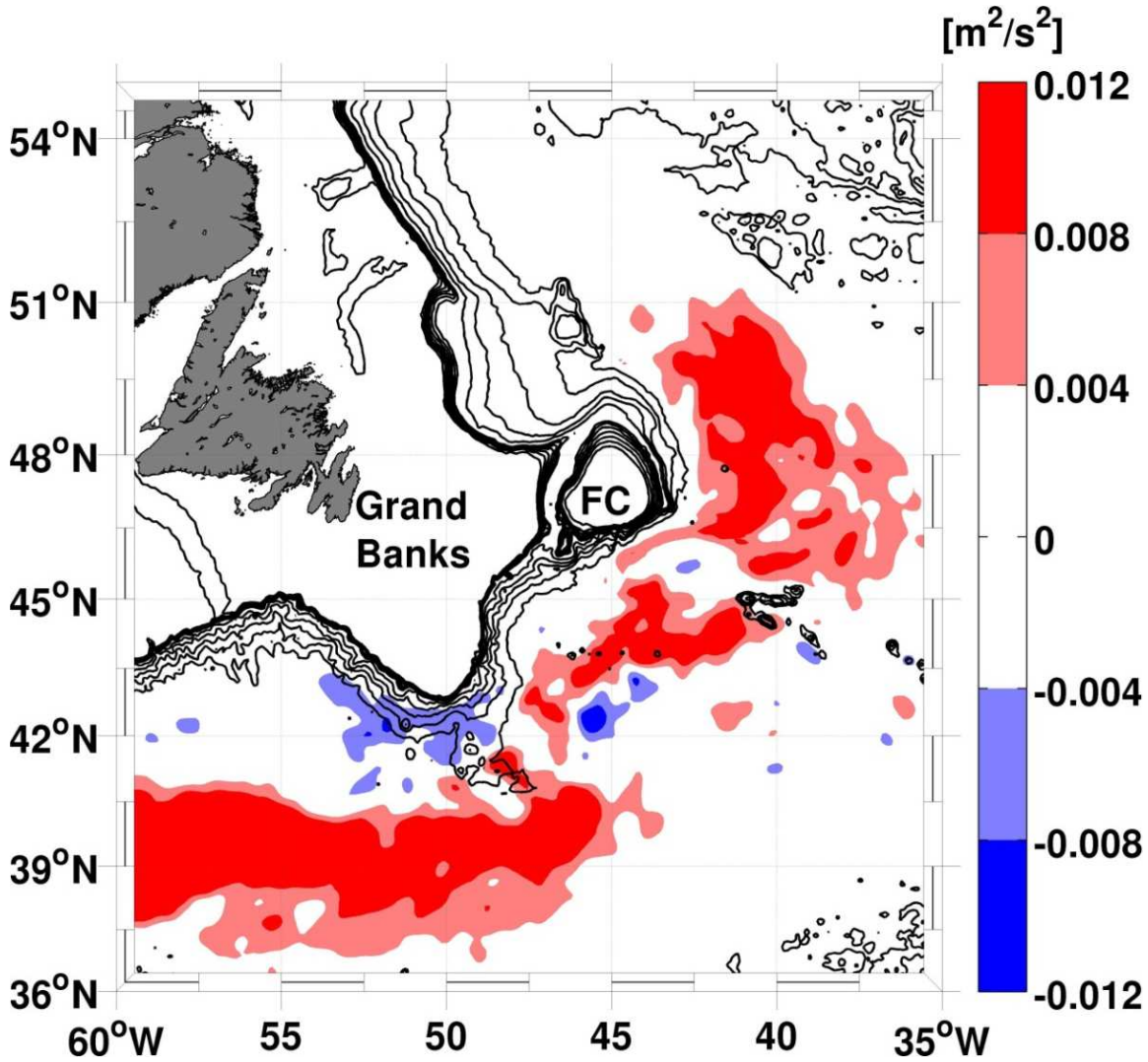


Figure 5.8: Difference in the mean eddy kinetic energy between the periods 1983-1995 and 1969-1979 averaged in the layer 200 m – 500 m, showing stronger variability close to the Flemish Cap (FC) in the latter period associated with the North Atlantic Current path closer to the western margin and featuring a more northward penetration. Isobaths are given every 100 m between 400 m and 1000 m and every 500 m from 1000 m to 3500 m [Varotsou et al., 2015].

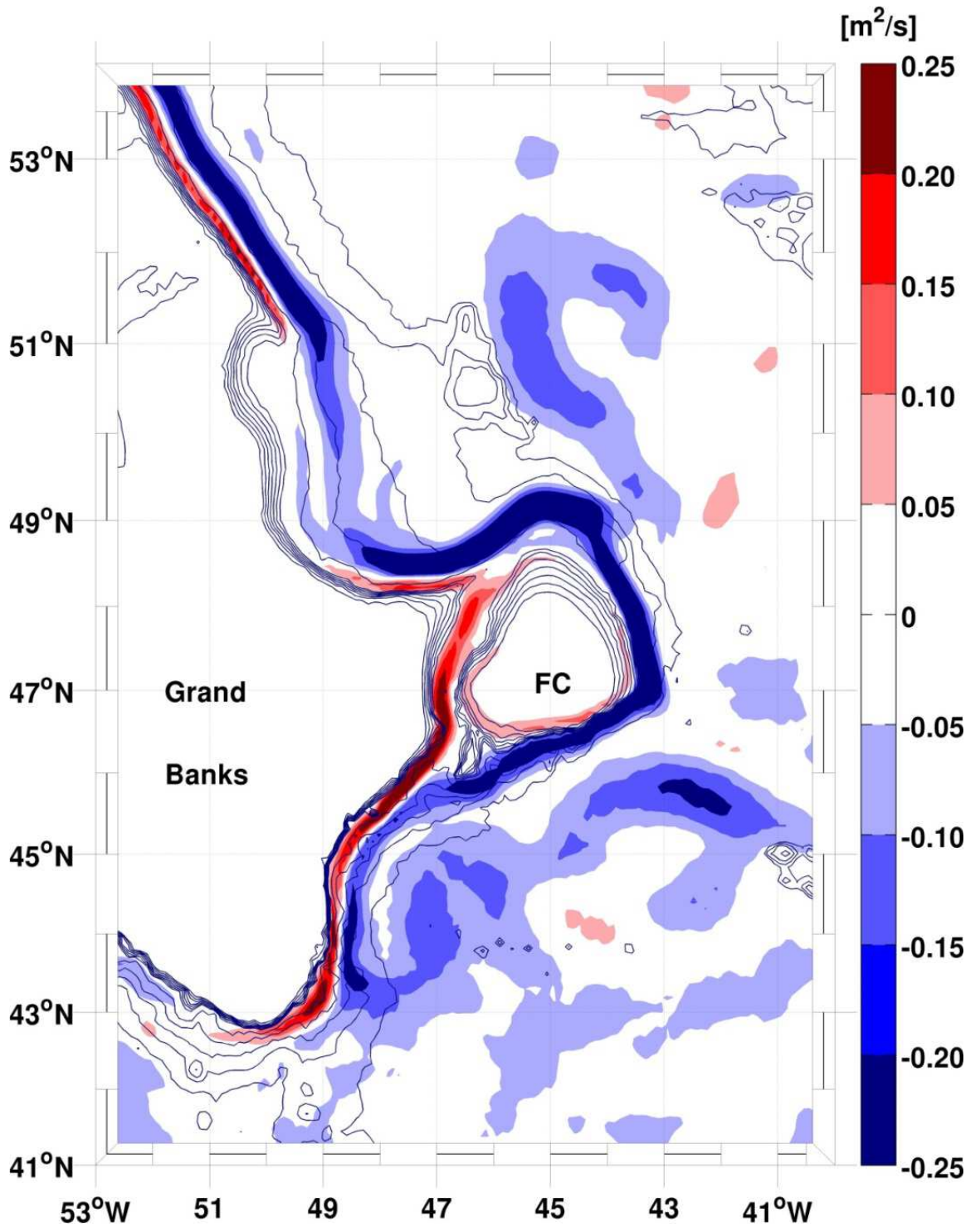


Figure 5.9: Map showing the difference in magnitude of the vertically-integrated volume fluxes in the model ULSW layer between the periods 1983-1995 and 1969-1979. Red colors (positive values) indicate stronger flow in the latter period, while blue colors (negative values) show reduced flow. FC: Flemish Cap [Varotsou et al., 2015].

5. ESTIMATION OF THE ULSW VOLUME TRANSPORT

Chapter 6

High frequency variability

In order to investigate the ULSW southward volume transport in the DWBC along the continental shelf slope (hereafter referred to as topographic slope) at the Grand Banks of Newfoundland at high frequencies, the model daily outputs from 2003 to 2009 were used. Assessing the effects of the topographic features on the ULSW volume transport variability in the DWBC at the Flemish Pass region, the propagating signal along the topographic slope is examined. The estimated results have been compared with the predicted results using a conceptual model as described by Brink-Chapman, 1987.

6.1 Power spectral density of the studied parameters

In order to analyse the propagating wave signal along the topographic slope, an analysis of the power spectral density of the ULSW volume transports at the Flemish Pass section, at 47°N and at 53°N in the DWBC is applied. An overview of the power spectral density shows that the strongest peak corresponds to the annual cycle. There is also much energy at the high frequencies (24 days and 11 days shown in Figure. 6.1) at the selected sections during the investigated period. To get a better understanding of the variability at high frequencies, the peaks of energy of the ULSW volume transport, the U and V velocity components variance and the layer thickness variance are separately examined.

The V velocity's variance and the changes of the ULSW layer thickness are taken into consideration for the computation of the volume transport variability at the examined sections. The ULSW layer thickness is defined either as the outcrop of ULSW layer thickness at the surface or as the outcrop of the DLSW at the surface. The outcrops depend on the intensity of the deep convection which takes place during the winter

6. HIGH FREQUENCY VARIABILITY

period. In order to focus only at the topographic slope in the ULSW density layer, a mask is applied to the layer thickness considering the region from the continental shelf to 80 km eastwards.

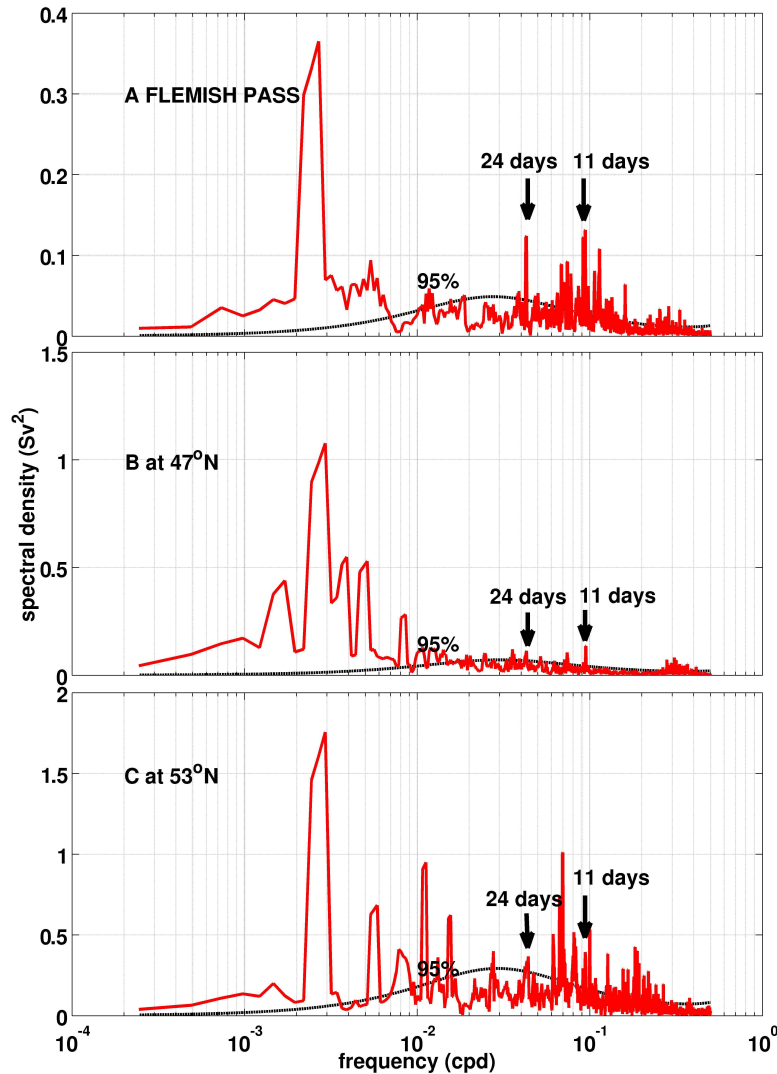


Figure 6.1: Variance preserving power spectra of daily transports (unfiltered) in Flemish Pass (A) and at 47°N (B) and at 53°N (C) in the ULSW density layer obtained by a multi-taper method following Ghil et al. [2002]. The significant peaks of energy at high frequencies are pointed out by the black arrows, the significance level at 95 % by the dotted line.

The power spectral density of U and V components from the model outputs have been compared with the available observations at the center of the Flemish Pass region

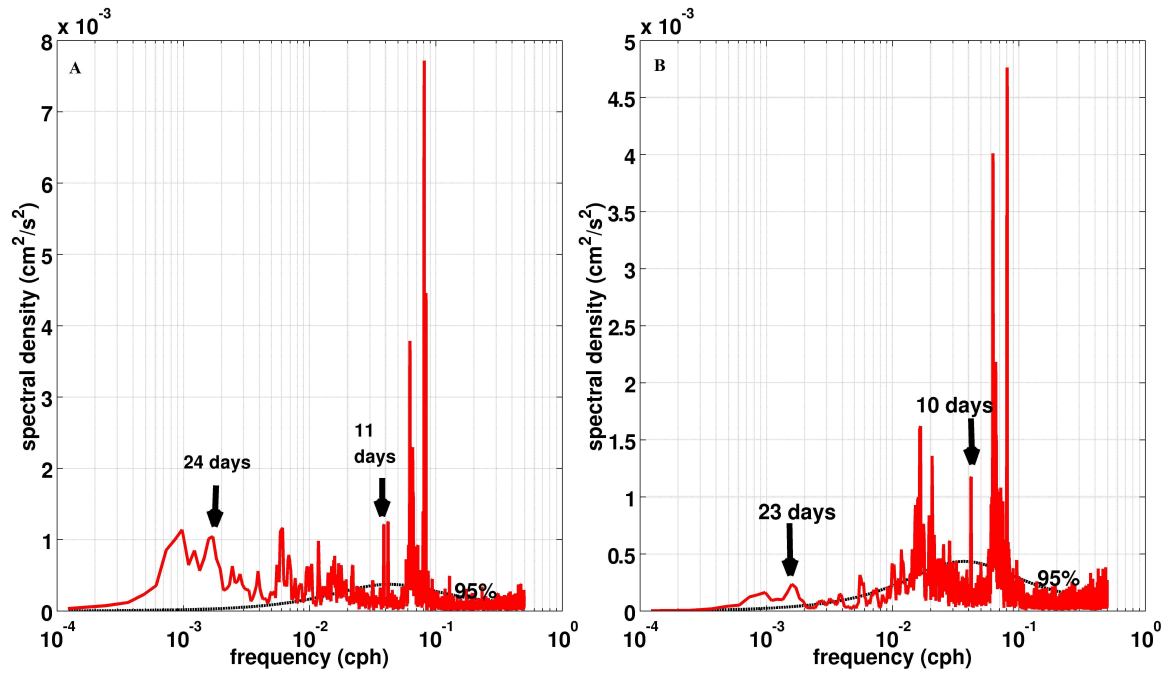


Figure 6.2: Variance preserving power spectra of the observed A) V and B) U velocity at the center of the Flemish Pass area ($47^{\circ}12'N/47^{\circ}10'W$ at 908 m depth for one year from July 2012 to May 2013 obtained by a multi-taper method following Ghil et al. [2002]. The significant peaks of energy at the 24 and 11 (considered to V) days and 23 and 10 days (considered to U) are pointed out by the black arrows, the significance level at 95 % by the dotted line.

($47^{\circ}12'N/47^{\circ}10'W$ at 908 m depth for one year from July 2012 to May 2013 (provided by Linn Schneider, personal communication). The modeled U and V velocity variances at the same position, as the observations, appear to have also a similar strong peak at high frequencies (not shown). The V (Figure. 6.2 A) velocity variance at the center of the Flemish Pass region presents a strong peak of energy at frequencies corresponding to 24 and 11 days period, indicating the strong propagating signal in alongshore direction. The power spectral density has been calculated for the variability of the ULSW layer thickness showing the dominant peaks at the same frequencies as the modeled and observed V velocity. Thus, the ULSW volume transport is influenced by both variances in V velocity and layer thickness. A pronounced propagating wave signal at the same frequencies is depicted in the spectral frequency of the representative observed U velocity's variance (Figure. 6.2 B) at the center of the Passage, associated to the propagating signal in the cross-shore direction. These strong signals at the high frequencies

6. HIGH FREQUENCY VARIABILITY

mentioned may be attributed to coastal trapped waves (CTWs), as will be investigated the following section.

The variability of the ULSW volume transport presents stronger signal at 24 and 11 days at 53°N and at the Flemish Pass region relative to 47°N region in the DWBC, indicating that the variability is stronger close to the topographic slope and decays offshore. Several sensitivity tests of the examined parameters are performed in order to identify the correct cut off periods by using a band-pass filter. The proper band pass filters centred at 24 (with cut off periods 22-26 days) and 11 (with cut off period 9-13 days) days are applied to the examined parameters, providing the information of the propagating signal along the topographic slope.

Subsequently, there are strong indications that the coastal trapped waves are an important mechanism influencing the ULSW volume transport variability and thus a short introduction for the CTWs will be given in the following section.

6.2 Basic Characteristics of the coastal trapped waves

A description of the trapping mechanisms has been presented by Mysak, [1980] and Huthnance, [1975]. Coastal trapped waves are not widely investigated in the deep layer of the ocean so far, comparison with other studies is therefore limited. In general, the CTWs are characterized as a hybrid of the internal kelvin waves and the barotropic shelf waves (Figure. 6.3) with large vorticity and shifting isopycnals [Allen, 1978]. As described by Gill [1982], the CTWs occur on the continental shelf and topographic slope regions in the stratified ocean. The CTWs could be classified according to the stratification parameter based on the equation $\epsilon = \lambda/L$, where λ denotes an internal radius of deformation and L denotes the shelf width [Yosuke et al., 2007]. These CTWs present large amplitudes close to the coast and decay offshore; the signal of the waves propagates parallel to the shoreline. This kind of waves are linked to the stratification of the ocean and the steepness of the bathymetry [Huthnance, 1978]. Topographic waves dominate the variance of the Boundary Current in the Labrador Sea [Fischer et al., 2015].

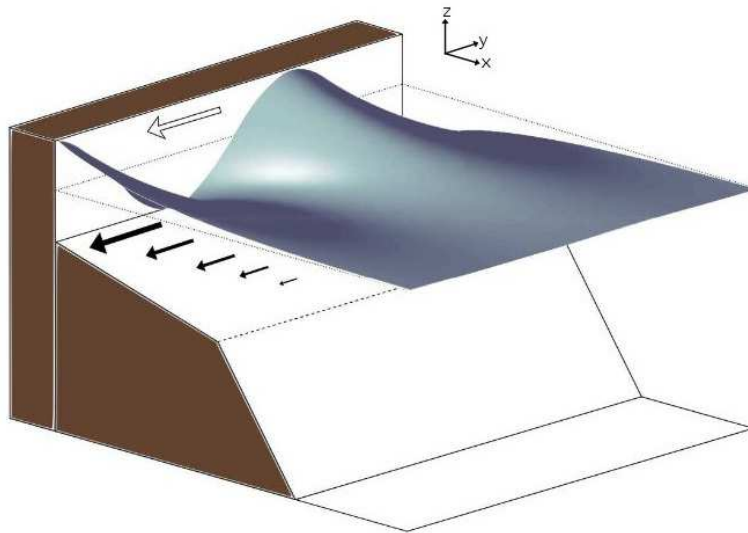


Figure 6.3: A computer assisted conception of a shelf wave from Pearche [2011]. The white arrow shows the phase of propagation in the northern hemisphere and the black arrows over the shelf slope indicate the water velocity under the crest.

In the past, links between the dissipative effect of the bottom friction [Brink, 2006], beta effect, coastline curvature [Grimshaw, 1977] and the influences of the atmospheric forcing [Clarke, 1977] on the CTWs have been investigated. Nevertheless, there is no

6. HIGH FREQUENCY VARIABILITY

so a clear definition of the coastal trapped waves in the literature. For this reason, any wave that is found along the coastline of the shelf has been referred to as this kind of waves.

In the following the possible existence of coastal trapped waves in the working region is demonstrated by propagating signals parallel to the shoreline, which also show an intensification at the surface layer. The wave is characterized by the wave frequency ω , the wavelength λ and the propagation phase speed U_p along the topographic slope. In order to investigate the theoretical approach of the coastal trapped waves, a simplified computer model [Brink and Chapman, 1987] is used, where the dispersion characteristics of a wave at a given topographic shelf slope and stratification is diagnosed.

6.2.1 Investigating the propagating signal at the topographic slope of the Continental shelf at the Grand Banks

An overview of the propagating signal is presented by the spatial distribution of the filtered magnitude of the vertically integrated volume fluxes in the ULSW density layer. An example of how the signal propagates from the north to the south, is depicted in Figure. 6.4. Strong variability is noticed along the topographic slope in the DWBC. Positive and negative anomalies of the ULSW vertically-integrated flux anomaly occur, which show similarities to wave signals. Having specified the region along the topographic slope as the most important region for the examination of the propagating signal, the boundaries of the defined layer thickness, as described above, are applied to the magnitude of the vertically integrated fluxes.

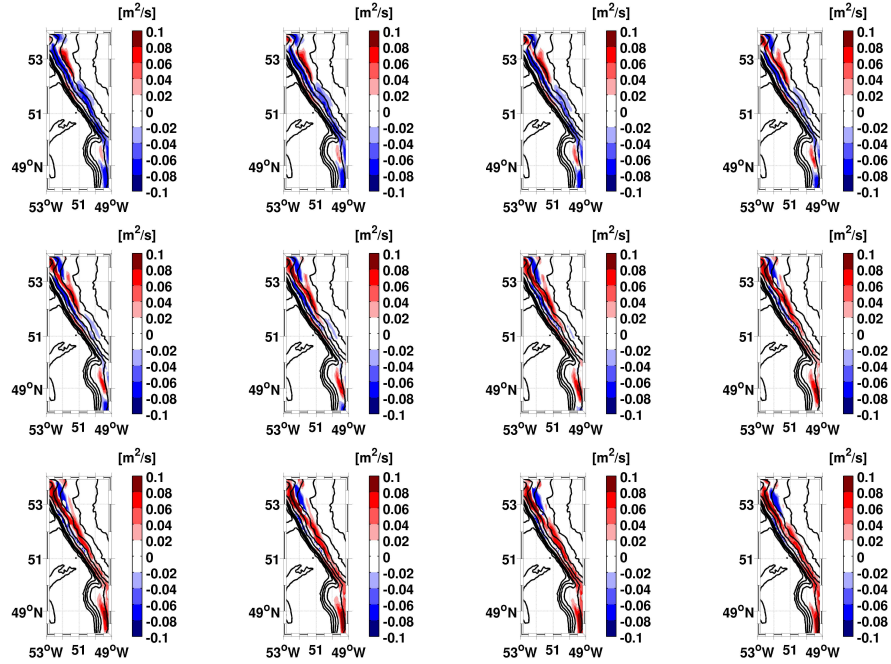


Figure 6.4: Exemplary snapshots maps showing the spatial distribution of the filtered ULSW vertically integrated magnitude in the ULSW density layer (using a band-pass filter centred at 24 days) in the DWBC at the topographic slope along the continental shelf at the Grand Banks during the winter period from 16th to 27th of January 2006. Isobaths are given from 600 m to 1000 m every 200 m.

The propagating signal occurs in the alongshore direction, having the land on the right side in the northern hemisphere, due to the Coriolis effect. The phase speed is computed by the slope of the ULSW layer thickness anomalies and the anomalies of the U and V component of 908 m depth (this depth belongs to the ULSW density layer). The phase speed of the examined anomalies is calculated by using the latitude vs. time diagram Figures 6.5 and 6.6 show the diagram of latitude (from 53°N to 47°N) vs. time (during the winter period January-February-March of each year and during the summer period June-July-August of each year) averaged over the longitudinal range. The filtered layer thickness anomalies depict a banded structure with positive and negative anomalies; a slope in the phase line shows the southward propagating signal. In general, the propagation phase speed is computed by the gradient $\Delta\chi/\Delta t$ of the examined parameters, where $\Delta\chi$ denotes the distance between two points in latitude of the maxima signal and Δt denotes the time difference between these two points in

6. HIGH FREQUENCY VARIABILITY

latitude following the propagating signal. The mean value (\pm standard deviation) of the phase speed of each parameter (Table 6.1) is inferred from various samples for each of them. In the winter period of 2003, the slope of the layer thickness is steeper and the propagating signal is stronger compared to the slope of the layer thickness in winter 2006 at the same latitudes (from 53°N to 52°N). When the slope of the layer thickness is steep then the propagating wave signal is strong and the phase speed higher compared to the smoother slope of the layer thickness during the winter of 2006. At 51°N , the signal propagation seems to be disturbed due to the refraction at the topography.

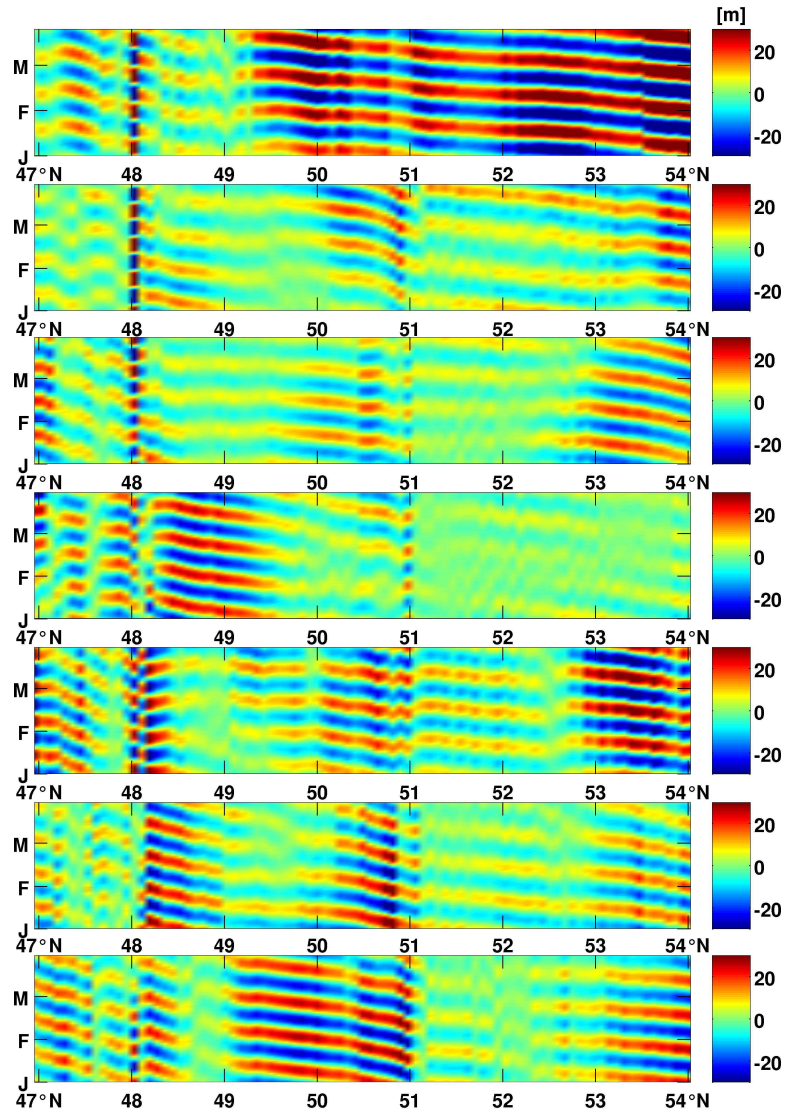


Figure 6.5: Band-pass filtered anomalies (from 22 to 26 days) of the layer thickness (averaged over longitudinal range) in the ULSW density layer latitude vs. time diagram along the topographic slope during the winter period (January-February-March) of each year during the period from 2003 (top) to 2009 (bottom).

6. HIGH FREQUENCY VARIABILITY

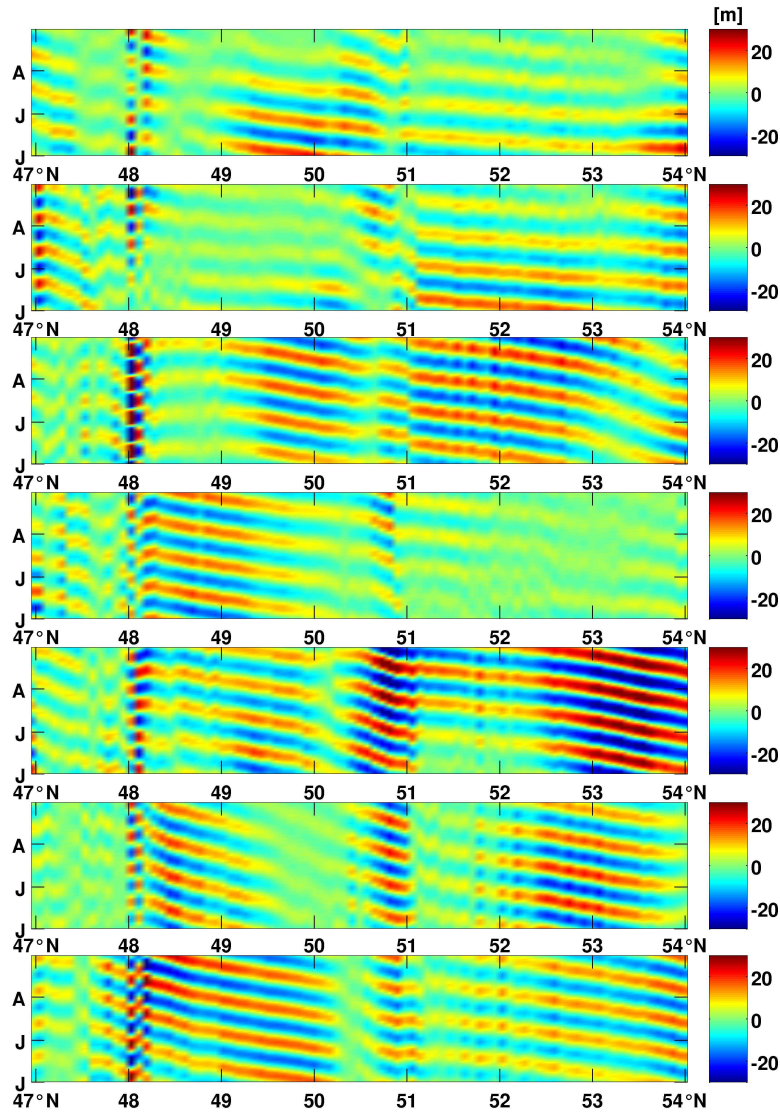


Figure 6.6: Band-pass filtered anomalies (from 22 to 26 days) of the layer thickness (averaged over longitudinal range) in the ULSW density layer latitude vs. time diagram along the topographic slope during the summer period (June-July-August) of each year during the period from 2003 (top) to 2009 (bottom).

The results of the phase speed have been validated by using the software package from Brink-Chapman. This software package gives a solution of the inviscid equations of motion for free wave solutions of linearized coastal trapped waves. By using this package, a theoretical approach of the frequencies at each wavenumber is produced, which is based on the shelf profile and the stratification profile (N^2 , Brunt-Väisälä fre-

Parameters	mean \pm std
Layer thickness	15.9 ± 5 cm/s
U velocity of 908 m depth	15.6 ± 4.7 cm/s
V velocity of 908 m depth	17.9 ± 3 cm/s

Table 6.1: Mean values and standard deviation of the phase speed along the topographic slope from 53°N to 51°N from the latitude vs. time diagram of the band-pass (centered at 24 days) filtered layer thickness, U velocity and V velocity

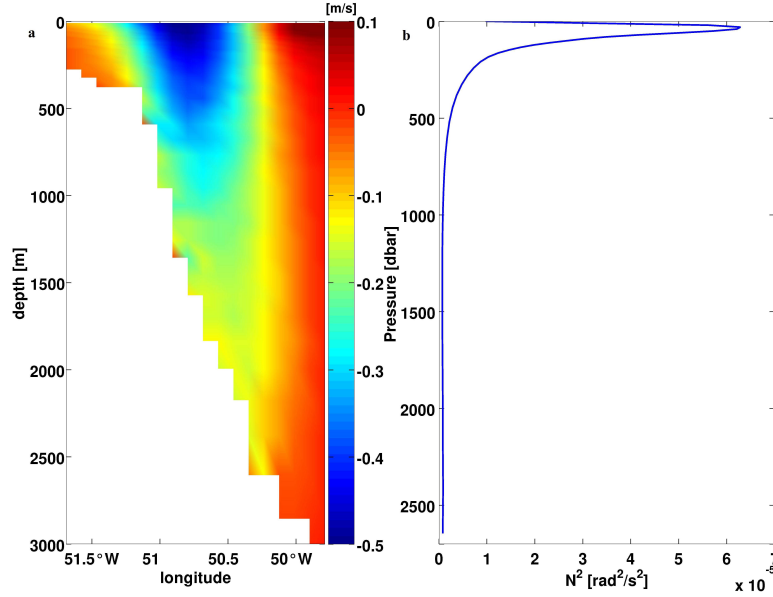


Figure 6.7: a) Velocity (m/s) profile from the shelf to the topographic slope at 52°N and b) Stratification profile at 52°N

quency). The elements of the input array are taken from the MITgcm model outputs.

The bathymetry profile in the cross-shore section at 52°N from the shelf to the slope (Figure. 6.7 a) and the N^2 from the surface to the bottom at 52°N (Figure. 6.7 b) are given as inputs to the programme. In order to provide the first mode of the wave, a first guess frequency $\omega < f$ (Coriolis parameter) and the first alongshore wavenumber should be given. As a first guess frequency $\omega_1 = 3.0301e^{-6} \text{ rad/s}$ is chosen. The alongshore wavenumber is based on the equation $\kappa = 2\pi/\lambda$, where λ denotes the wavelength of the wave in km. The wavelength is the distance between two maxima of the filtered (24 days) vertically integrated volume fluxes anomalies along the topographic slope. In my case, the estimated wavelength is about 284 km from ($53^\circ 99'\text{N}/52^\circ 15'\text{W}$) to ($51^\circ 78'\text{N}/50^\circ 02'\text{W}$) from point A to point B (Figure. 6.8) ,respectively. The predicted

6. HIGH FREQUENCY VARIABILITY

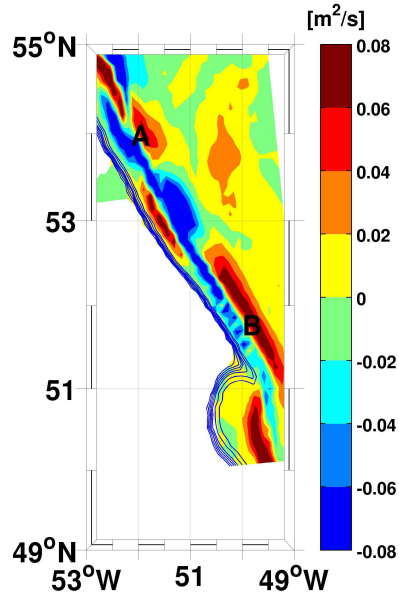


Figure 6.8: Exemplary snapshot map showing the spatial distribution of the filtered ULSW vertically integrated magnitude in the ULSW density layer (using a band-pass filter centred at 24 days) in the DWBC at the topographic slope at the Grand Banks on January 2005. The wavelength of the propagating signal is the distance difference from the point A to the point B ($53^{\circ}99'N/52^{\circ}15'W$) to ($51^{\circ}78'N/50^{\circ}02'W$).

results from the coastal trapped wave programme coincide to the estimated results from the model outputs along the slope of the continental shelf. The predicted wavelength from the programme ranges from 280 to 295 km in 23.1 days and the phase speed is about 14.2 cm/s. These values correspond to 0 cm/s velocity of the mean alongshore flow.

The same process was followed for the computation of the phase speed by using band-pass filtered parameters centred at 11 days. In order to compute the phase speed along the topographic slope by using the filtered layer thickness, U and V velocity anomalies, the latitude vs. time diagram at each year during the winter period (January-February-March) is presented (Figure 6.9). The structure of the layer thickness anomalies seems to be banded in a similar way as for 24 days frequency. By using the band pass filter at 11 days, the slope of the layer thickness anomalies is steeper and the signal is stronger compared to the slope and the intensity of the propagating signal by using the band pass filter in period of 24 days. The estimated mean value of the phase speed of each examined parameter has a high variance (Table 6.2). Therefore, the estimated mean values seem to be in good agreement with the predicted phase

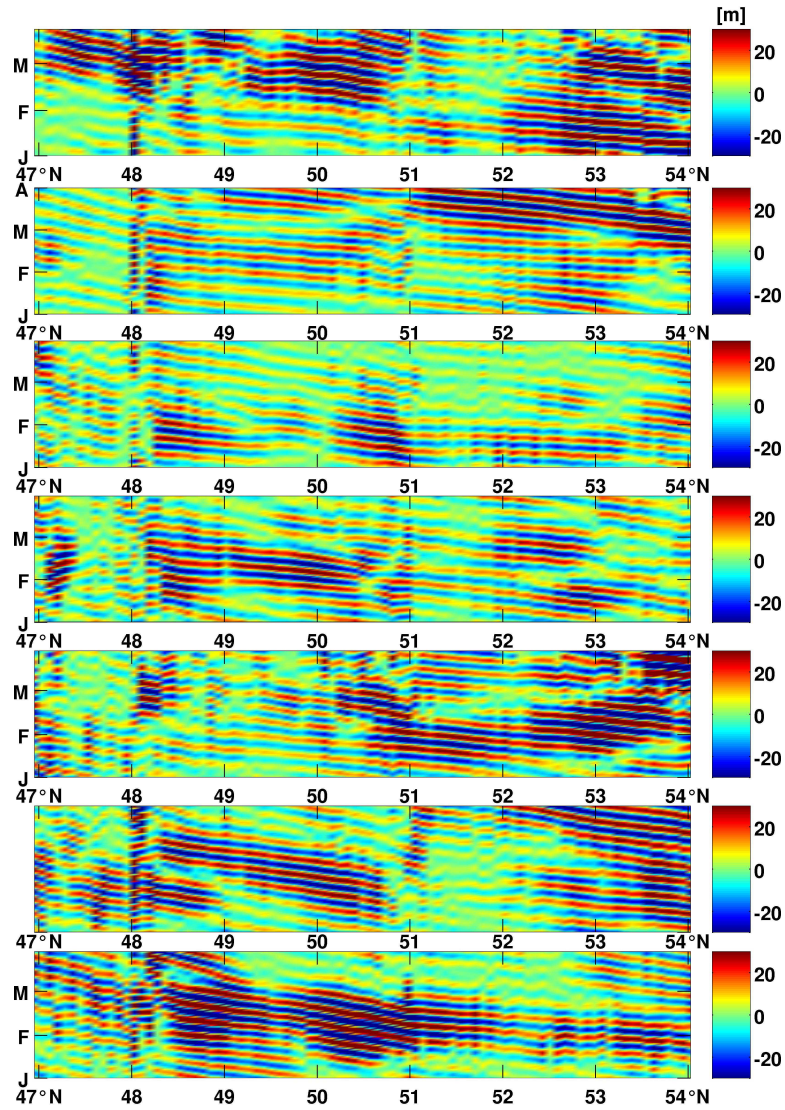


Figure 6.9: Band-pass filtered anomalies (from 11 to 13 days) of the layer thickness (averaged over longitudinal range) in the ULSW density layer latitude vs. time along the continental shelf slope during the winter period (January-February-March) of each year during the period from 2003 (top) to 2009 (bottom).

speed 40.2 cm/s in 11 days and the wavelength varies from 380 to 450 km. In this case, a first guess frequency $\omega_1 = 6.6111e^{-6} \text{ rad/s}$ is selected.

Thus, the ULSW volume transport variability might be primarily associated with the coastal trapped waves along the topographic slope characterized by the periods 24 and 11 days. The strongest perturbation of the volume transport occurs close to the

6. HIGH FREQUENCY VARIABILITY

Parameters	mean \pm std
Layer thickness	31.4 ± 26.3 <i>cm/s</i>
U velocity of 908 m depth	47 ± 27 <i>cm/s</i>
V velocity of 908 m depth	37 ± 23.5 <i>cm/s</i>

Table 6.2: Mean (\pm standard deviation) values of the phase speed along the continental slope from 53°N to 51°N from the latitude vs. time diagramm of the filtered (centered at 11 days) layer thickness, U and V velocity.

topographic slope and decays offshore.

Chapter 7

Conclusions

The aim of this thesis was to investigate the export of the ULSW which is a pathway in the DWBC from the north to the south through Flemish Pass, in the vicinity of the Continental shelf at the Grand Banks of Newfoundland. The spreading of LSW in this region has been examined by e.g using floats trajectories [Bower et al., 2011]. [Bower et al., 2011] show that the largest amount of the LSW around the Flemish Cap region is transferred by the DWBC from the subpolar to the subtropical region and a significant amount enters the subtropical region through interior pathways. In the same study [Bower et al., 2011], the LSW transport from the north to the south was shown to be faster through Flemish Pass than the transport around the Flemish Cap region. Therefore, ULSW volume transport variability from the north to the south through Flemish Pass has been the focus of this thesis. The ULSW volume transport variability through Flemish Pass is compared with upstream fluctuations of the ULSW volume transport at 53°N and at 47°N in the DWBC.

7.1 Summary and discussion

In Chapter 3, a brief overview of the ULSW circulation in the study region is presented by the vertically integrated volume fluxes using model outputs on a monthly basis during the period from 1960 to 2009. The estimates show that the averaged ULSW transport decreases downstream from 6.7 ± 1.9 Sv at 53°N to 4.5 ± 1.3 Sv at 45°N due to loss into the interior ocean (Figure. 3.1). The aforementioned value of the average southward transport at 53°N , is lower than the previous observational results (8.9 ± 1.9 Sv, [Fischer et al., 2010]) but the amplitude of the variability is consistent between the two studies. The average DWBC transports at 47°N in the ULSW layer, as well as its variability agree well to observational estimates (Figure 2.1 [Schneider et al.,2015]).

7. CONCLUSIONS

The contribution of Flemish Pass to the ULSW export, which is not negligible, agrees with estimates based on observations [Schneider et al., 2015]. The important role of the ULSW transport through Flemish Pass is confirmed by using an isolated box (Figure. 3.2) from 47°N to 45°N . By using a closed box the lateral fluxes are isolated and the ULSW volume transport at the 45°N (4.8 Sv) section shows clearly the southward transport component. The contribution of the ULSW volume transport through Flemish Pass to the total amount of the ULSW downstream transport at 45°N is about 10 % more than the ULSW volume transport at 47°N through Flemish Pass. Flemish Pass can therefore be considered as a direct pathway for ULSW to the south.

Investigation of the temporal evolution of the ULSW volume transport at the examined sections shows a dominant peak of energy in periods of 3 years and 1 year (annual cycle). In order to analyse the ULSW volume transport on the interannual timescale from the north to the south, a band pass filter (centered at 3 years) is applied. Although approximately 2.2 Sv of ULSW transport is lost along the southward pathway of the DWBC around the southern Flemish Cap, the variability within the DWBC is consistent when following the continental slope on interannual time scales, with a short time lag of 3 months existing between 53°N and 47°N east of Flemish Cap. However, the variability in Flemish Pass differs either on seasonal timescale (shown in Figure. 3.8 in chapter 3) or at the interannual timescale (shown in Figure. 5.2 in chapter 5) from the eastern pathway, and the amplitude of the variability is smaller.

In the second part of Chapter 3, the averaged (50 years) seasonal cycle is considered in order to show the different behavior of the ULSW volume transport at each section. The seasonal variability is coherent along the path of the DWBC from 53°N southward and around Flemish Cap, with a short time lag. The importance of local atmospheric forcing is highlighted by the seasonal cycle of the transport at Flemish Pass and for the transport variability at 53°N . A minimum transport at Flemish Pass follows after two months from the maximum southward transport at 47°N in the DWBC. The importance of the layer thickness variance and velocity variance on a seasonal timescale has been examined by computing the decomposed transport at each studied section. The results show a significant contribution of the layer thickness variance to the ULSW volume transport at each section at seasonal timescales (Figure. 3.9B).

In the first part of Chapter 4, the contribution of the volume transport variability at the surface layer to the ULSW volume transport on interannual timescale is estimated using the running correlation coefficient method. The effects of the volume transport at the surface layer on the ULSW volume transport at Flemish Pass and at 47°N are presented from 1965 to 1970. During this period, the variability can be explained by

barotropic variance.

The strong anti-correlation between the ULSW and DLSW layer thickness [Stramma et al., 2004; Rhein et al., 2011; Kieke and Yashayaev, 2015] shows that the ULSW mode replaces the DLSW mode. In the observational study of Schneider et al., [2015], the ULSW mode is the dominant mode through Flemish Pass. In order to investigate the influences of the ULSW layer thickness on the volume transport on interannual timescale, the decomposed transport is computed. The results show that the impact of the variability of layer thickness on the ULSW transport variability seems to be stronger than the influence of the velocity variability.

In Chapter 5, the effects of various physical parameters on the ULSW volume transport on interannual timescales are presented [Varotsou et al., 2015]. The behavior of the band-pass filtered ULSW transport anomalies at both Flemish Pass and in the DWBC at 47°N can be attributed to influences of different parameters. Upstream transport fluctuations dominate the variability of the ULSW transport at 47°N at the east part of Flemish Cap. ULSW formation is identified as the main process impacting on the DWBC transport. The propagation time scale of the ULSW formation rate variations from the Labrador Sea to Flemish Cap (5 months) agrees with the rapid export of newly formed ULSW found in a high-resolution model [Brandt et al., 2007] for convection close to or in the boundary current. In the DWBC at 47°N , the influence of the Ekman transport is rarely of any significance; similarly the basin wide circulation changes in the Subpolar Gyre and the large scale NAO forcing only sometimes add variability to this transport.

However, when subtracting the upstream variability from the DWBC transport the residual at 47°N shows a response to local forcing, such as the Ekman transport and the NAC position. The residual is always in anti-phase with the Flemish Pass transport; the flow fluctuations are thus compensating each other.

The independent behavior of the variability at Flemish Pass from the upstream fluctuations was pointed out in the running correlations. Here, the variability is influenced by all considered physical mechanisms over the study period: firstly, the NAO dominates the variance, followed by the Ekman transport and the remote ULSW formation in the late 1970s. These results are not surprising, local and large scale wind forcing and the ULSW formation rate are likely candidates for impacting variability on the ULSW export rate.

In contrast, the pronounced influence of the NAC position on the Flemish Pass transport in the period 1980-1998 is rather surprising. This clear relationship between NAC position changes and transport fluctuations in Flemish Pass is an interesting

7. CONCLUSIONS

result and needs further explanation. When the NAC is close to Flemish Cap the flow at Flemish Pass is enhanced, but the DWBC is not influenced by the NAC position (Figures 5.6 D and 5.5 D). What seems to be counterintuitive at first turns out to be simple to explain when analyzing the part of the DWBC flow at 47°N , which cannot be explained by upstream transport fluctuations (the residual, being sensitive to local forcing). The residual is connected to the NAC position as well, but with an in-phase correlation: when the NAC is close to Flemish Cap, the flow is weaker. Similar shifts of the NAC position (in the order of 150 km) were also shown by Mertens et al. [2014] using sea surface height data (AVISO).

To conclude, I found a non-negligible transport of ULSW through Flemish Pass, which is on interannual time scales (3-years) influenced by various local and remote processes, but not dominated by upstream variations. The amplitude of transport fluctuations in Flemish Pass is smaller when compared to the transport anomalies in the DWBC. Thus, the pathway of ULSW through Flemish Pass may be seen as a more direct export route for ULSW than the DBWC pathway and should be considered when addressing the exchanges between the subpolar and subtropical gyres at 47°N [Varotsou et al., 2015].

In Chapter 6, the analysis of the ULSW volume transport at high frequencies is carried out by using daily model outputs from 2003 to 2009. A comparison of the U and V velocity variance between observations and model outputs shows a substantial energy for periods 23 and 10 days (considered to U variance) and 24 and 11 days (considered to V variance). The pronounced peaks of energy of the ULSW volume transport variability at the examined sections correspond to periods of $T \leq 25$ days. The variability of the ULSW volume transport in the frequency band of 24 and 11 days along the topographic slope may be explained by the presence of coastal trapped waves and is further examined using a conceptual model provided by Brink-Chapman [1987]. This simple model produces the phase speed and the wavelength of coastal trapped waves. The phase speed of the propagating signal along the slope has been estimated from the inclination of the gradient of the layer thickness, and the U and V variance. The wavelength of the signal is defined as the distance between two maxima of flux anomalies along the topographic slope. As a result, the predicted results from the conceptual model agree well with the estimated results from the model outputs for periods of 24 and 11 days. The high frequency variability of ULSW volume transports may thus be attributed to coastal trapped waves.

7.2 Further investigation

The contribution of the transport variability through Flemish Pass to the downstream fluctuations for example at 45°N in the DWBC on interannual timescale has not been widely investigated. Furthermore, the variability of different quantities (e.g. eddy kinetic energy) can provide more information about the crucial role of the Flemish Pass region in the circulation at the western boundary of the subpolar Atlantic.

In terms of the analysis of the propagating signal along the slope of the Continental shelf at the Grand Banks, further research could be focused on the analysis of the propagating signal using other settings in the conceptual model (e.g non zero background velocity). A comparison between the predicted and estimated results could determine the dispersion curve of the wave and define the modes of the waves. Moreover, other properties of the waves can be investigated.

Already published papers in peer reviewed journals

Varotsou E., K. Jochumsen , N. Serra , D. Kieke and L. Schneider, (2015):
Interannual transport variability of Upper Labrador Sea Water at Flemish Cap. *J. of Geophys. Res. : Oceans*, 120 :5074–5089, doi:10.1002/2014JC010632.

Schneider L., D. Kieke, K. Jochumsen, E. Colbourne, I.Yashayaev, R. Steinfeldt, **E. Varotsou**, N. Serra, and M. Rhein, (2015): Variability of Labrador Sea Water transported through Flemish Pass during 1993-2013. *J. Geophys. Res. :Oceans*, 120:5514–5533, doi:10.1002/015JC010939.

Bibliography

- Allen J. S., (1978): Coastal trapped waves in a stratified ocean. *J. Phys. Oceanogr.*, 5, 300–325.
- Böning C. W., A. Dispert, M. Visbeck, S. R. Rintoul and F. U. Schwarzkopf, (2008): The response of the antarctic circumpolar current to recent climate change. *Nat. Geosci.*, 1: 864–869, doi:10.1038/ngeo362.
- Biastoch A., C. W. Böning, J. Getzlaff, J.M. Molines, and G. Madec, (2008): Causes of interannual decadal variability in the meridional overturning circulation of the mid-latitude North Atlantic ocean. *Journal of Climate*, 21 (24): 6599–6615, doi:10.1175/2008JCLI2404.1.
- Boccaletti G., R. Ferrari, A. Adcroft, D. Ferreira, and J. Marshall, (2005): The vertical structure of ocean heat transport. *Geophys. Res. Lett.*, 32 (L10603), doi:10.1029/2005GL022474.
- Bower A. S., M. S. Lozier, S. F. Gary, and C. W. Böning, (2009): Interior pathways of the North Atlantic meridional overturning circulation. *Nature*, 459(7244): 243–247, doi:10.1038/nature07979.
- Bower A., S. Lozier, and S. Gary, (2011): Export of Labrador sea water from the subpolar North Atlantic: A lagrangian perspective. *Deep-Sea Research Part II: Topical Studies in Oceanography*, 58 (17-18): 1798–1818, doi:10.1016/j.dsr2.2010.10.060.
- Boyer T., Levitus, S., Garcia, H., Locarnini, R., Stephens, C., and coauthors, (2005): Objective analyses of annual, seasonal, and monthly temperature and salinity for the world ocean on a 0.25° grid. *Int. J. Climatol.*, 25 (7): 931-945, 14.
- Brandt, P., A. Funk, L. Czeschel, C. Eden, and C. W. Böning, (2007): Ventilation and Transformation of Labrador Sea Water and Its Rapid Export in the Deep Labrador Current. *J. Phys. Oceanogr.*, 37, 946-961, doi:10.1175/JPO3044.1.

BIBLIOGRAPHY

- Brath M., M. G. Scharffenberg, N. Serra, and D. Stammer, (2010): Altimeter-based estimates of eddy variability and eddy transports in the Subpolar North Atlantic. *Mar. Geod.*, **33**, 1, 472–503, doi:10.1080/01490419.2010.488921.
- Brink K. H., and D. C. Chapman, (1987): Programs for computing properties of coastal-trapped waves and wind-driven motions over the continental shelf and slope. *Rep. WHOI.*, 87–24, 46 pp., Woods Hole Oceanographic Institution, WoodsHole, MA.
- Brink K. H., (2006): Coastal-trapped waves with finite bottom friction *Dyn. Atmos. Oceans*, 41 (3-4), 172-190.
- Bubnov V. A, (1994): The North Atlantic Current by the Atlantex 90 experiment data. *Oceanology, Engl. Transl.*, 34(6): 733–737.
- Bullister L. J. , M. Rhein, and C. Mauritzen, (2013): Deep water formation in book Ocean Circulation and Climate, 2nd Ed. A 21st century perspective edited by Siedler (2013). *Academic Press*, Chap: 10, 227–253. ISBN: 978-0-12-391851-2
- Clarke A. J., (1977): Observational and numerical evidence for wind-forced coastal trapped long wave. *J. Phys. Oceanogr.*, 7, 231-247.
- Cohen J., P. Cohen, S.G. West and L.S. Aiken, (2003): Applied Multiple Regression/Correlation Analysis for the Behavioral Sciences. *Mahwah, NJ, Lawrence Erlbaum Associates*, 3rd .
- Colbourne E. B. and K. D. Foote, (2000): Variability of the stratification and circulation on the Flemish cap during the decades of the 1950s-1990s. *Journal of Northwest Atlantic Fishery Science*, 26 (1986): 103–122, doi:10.2960/J.v26.a5.
- Cuny J., P.B. Rhines and R. Kwok, (2005): Davis Strait volume, freshwater and heat fluxes. *Deep-Sea Res. I*, 52: 519–542, doi:10.1016/j.dsr.2004.10.006.
- Curry B., C. M. Lee, and B. Petrie, (2011): Volume, Freshwater, and Heat Fluxes through Davis Strait, 2004-05. *J. Phys. Oceanogr.*, 41 :429–436, doi:10.1175/2010JPO4536.1.
- Delworth T. L. and Dixon K. W., (2006): Have anthropogenic aerosols delayed a greenhouse gas-induced weakening of the north atlantic thermohaline circulation? *Geophys. Res. Lett.*, 33 (2): 3–6, doi:10.1029/2005GL024980.
- Dengler M., J. Fischer, F. Schott and R. Zantopp, (2006): Deep Labrador Current and its variability in 1996-2005. *Geophys. Res. Lett.*, 33 (21): L21S06, doi:10.1029/2006GL026702.

- Dickson R., J. Lazier, J. Meincke, P. Rhines, and J. Swift, (1996): Long-term coordinated changes in the convective activity of the north atlantic. *Prog. in Oceanog.*, 38(3): 241–295, doi:10.1016/S0079-6611(97)00002-5.
- Dmitrenko, A. I., S. A. Kirillov, N. Serra, N., N. V. Koldunov, V. V. Ivanov, U. Schauer, I. V. Polyakov, D. Barber, M. Janout, V. Lien, M. Makhotin, and Y. Aksenov, (2014): Heat loss from the atlantic water layer in the northern kara sea: causes and consequences. *Ocean Science*, 10 (4): 719–730, doi:10.5194/os-10-719-2014.
- Eden C. and J. Willebrand, (2001): Mechanism of interannual to decadal variability of the North Atlantic circulation. *J. of Climate*, 14 (10): 2266–2280, doi:10.1175/1520-0442(2001)014<2266:MOITDV>2.0.CO;2.
- Efron B. and G. Gong, (1983): A Leisurely Look at the Bootstrap, the Jackknife, and Cross-Validation. *American Statistician*, 37: 36–48, doi:10.1080/00031305.1983.10483087.
- Fekete M. B., C. Vörösmarty, and W. Grabs, (2000): Global composite runoff fields on observed river discharge and simulated water balances. *GRDC Rep.*, (22): 115, doi:10.1017/CBO9781107415324.004.
- Ferrari R. and D. Ferreira, (2011): What processes drive the ocean heat transport? *Ocean Modelling*, 38 (3–4): 171–186, doi:10.1016/j.ocemod.2011.02.013.
- Fischer J., F. Schott, and M. Dengler, (2004): Boundary circulation at the exit of the Labrador sea. *J. Phys. Oceanogr.*, 34 (7): 1548–1570.
- Fischer J., M. Visbeck, R. Zantopp, and N. Nunes, (2010): Interannual to decadal variability of outflow from the Labrador Sea. *Geophys. Res. Lett.*, 37 (24), L24610, doi:10.1029/2010GL045321. 22
- Fischer J., J. Karstensen, R. Zantopp, M. Visbeck, A. Biastoch, E. Behrens, C. W. Böning, D. Quadfasel, K. Jochumsen, H. Valdimarsson, S. Jónsson, S. Bacon, N. P. Holliday, S. Dye, M. Rhein, C. Mertens, (2015): Intra-seasonal variability of the DWBC in the western subpolar North Atlantic. *Progress in Oceanography*, 132: 233–249, doi:10.1016/j.pocean.2014.04.002.
- Ghil M., M. R. Allen, M. D. Dettinger, K. Ide, D. Kondrashov, M. E. Mann, A. W. Robertson, A. Saunders, Y. Tian, F. Varadi, and P. Yiou, (2002): Advanced spectral methods for climate time series. *Reviews of Geophysics*, 40 (1): 3.1–3.41, doi:10.1029/2001RG000092.

BIBLIOGRAPHY

- Gil J., R. Sanchez, S. Cerviño and D. Garabana, (2004): Geostrophic circulation and heat flux across the Flemish Cap, 1988-2000. *J. Northw. Atl. Fish. Sci.*, 34: 63–83, doi:10.2960/J.v34.m510.
- Gill, A. E., (1982): Atmosphere-ocean dynamics, International geophysics series. *Academic Press*, San Diego.
- Girton J. B., T. B. Sanford and R. H. Käse, (2001): Synoptic sections of the Denmark Strait overflow. *Geophys. Res. Lett.*, 28 (8): 1619–1622.
- Gouretski V. V. and K. P. Koltermann, (2004): *WOCE Global Hydrographic Climatology*, A Technical report, Bundesamt für Seeschifffahrt und Hydrographie.
- Gregory J. M., K. W. Dixon, R. J. Stouffer, A. J. Weaver, E. Driesschaert, M. Eby, T. Fichefet, H. Hasumi, A. Hu, J. H. Jungclaus, I. V. Kamenkovich, A. Levermann, M. Montoya, S. Murakami, S. Nawrath, A. Oka, A. P. Sokolov, R. B. Thorpe, (2005): A model intercomparison of changes in the Atlantic thermohaline circulation in response to increasing atmospheric CO_2 concentration. *Geophys. Res. Lett.*, 32 (12): 1–5, doi:10.1029/2005GL023209.
- Grimshaw R., (1977): The effects of a variable Coriolis parameter, coastline curvature and variable bottom topography on continental shelf waves. *J. Phys. Oceanogr.*, 7 (4), 547-554.
- Häkkinen S., (1999): Variability of the simulated meridional heat transport in the North Atlantic for the period 1951-1993. *J. of Geophys. Res.*, 104, doi:10.1029/1999JC900034.
- Han G., Z. Lu, Z. Wang, J. Helbig, N. Chen, and B. de Young, (2008): Seasonal variability of the Labrador Current and shelf circulation off Newfoundland. *J. of Geophys. Res.*, 113, C10013, doi:10.1029/2007JC004376.
- Hansen B. and S. Østerhus, (2000): North Atlantic Nordic Seas Exchanges. *Prog. in Oceanogr.*, 45 (2): 109–208, doi:10.1016/S0079-6611(99)00052-X.
- Hansen B. and S. Østerhus, (2007): Faroe Bank Channel overflow 1995–2005. *Progress in Oceanography*, 75 (4): 817–856, doi:10.1016/j.pocean.2007.09.004.
- Hurrell J. W., (1995): Decadal trends in the North Atlantic oscillation: Regional temperatures and precipitation. *Science*, 269 (5224): 676–679, doi:10.1126/science.269.5224.676.
- Huthnance J. M., (1975): On trapped waves over a continental shelf. *J. Fluid Mech.*, 69 (JUN24), 689-704.

- Huthnance J. M., (1978): Coastal trapped waves: Analysis and numerical calculation by inverse iteration. *J. Phys. Oceanogr.*, 8 (1), 74-92.
- Jochumsen J., D. Quadfasel, H. Valdimarsson, and S. Jónsson, (2012): Variability of the Denmark strait overflow: Moored time series from 1996-2011. *J. Geophys. Res.*, 117 (C12): C12003, doi:10.1029/2012JC008244.
- Johannessen J. A., R. P. Raj, J. E. Ø. Nilsen, T. Pripp, P. Knudsen, F. Counillon, D. Stammer, L. Bertino, O. B. Andersen, N. Serra, and N. Koldunov , (2014): Toward improved estimation of the dynamic topography and ocean circulation in the high latitude and arctic ocean: The importance of GOCE. *Surv. in Geophys.*, 35 (3): 661–679, doi:10.1007/s10712-013-9270-y.
- Köhl A. and D. Stammer,(2008): Variability of the Meridional Overturning in the North Atlantic from the 50 years GECCO State Estimation. *J. Phys. Oceanogr.*, 38, 1913-1930.
- Köhl A. and N. Serra, (2014): Causes of Decadal Changes of the Freshwater Content in the Arctic Ocean. *J. of Climate*, 27 (9): 3461–3475, doi:10.1175/JCLI-D-13-00389.1.
- Kalnay E., M. Kanamitsu, R. Kistler, and co authors, (1996): The NCEP/NCAR 40-year reanalysis project. *Bull. Amer. Meteor. Soc.*, 77: 437–470.
- Kieke D., M. Rhein, L. Stramma, w. M. Smethie, D. A. LeBel, and Z. Walter, (2006): Changes in the CFC Inventories and Formation Rates of Upper Labrador Sea Water, 19972001. *J. Phys. Oceanogr.*, 36 (1): 64–86, doi:10.1175/JPO2814.1.
- Kieke D., M. Rhein , L. Stramma , W. M. Smethie, J. L. Bullister and D. A. LeBel, (2007): Changes in the pool of Labrador Sea Water in the subpolar North Atlantic. *Geophys. Res. Lett.*, 34, L06605, doi:10.1029/2006GL028959.
- Kieke D., B. Klein, L. Stramma, M. Rhein, and K. Koltermann, (2009): Variability and propagation of Labrador Sea Water in the southern subpolar North Atlantic. *Deep Sea Res. Part I: Oceanogr. Res. P.*, 56(10): 1656–1674, doi:10.1016/j.dsr.2009.05.010.
- Kieke D., and I. Yashayaev , (2015): Studies of Labrador Sea Water formation and variability in the subpolar North Atlantic in the light of international partnership and collaboration. *Prog. Oceanogr.*, 132 (3), 220-232, doi:10.1016/j.pocean.2014.12.010.
- Koldunov N.V., N. Serra, A. Köhl, D. Stammer, O. Henry, A. Cazenave, P. Prandi, P. Knudsen, O. B. Andersen, Y. Gao and J. Johannessen, (2014): Multi-model simulations of arctic ocean sea surface height variability in the period 1970-2009. *J. of Geophys. Res.* , 119: 8936–8954, doi:10.1002/2014JC010170.

BIBLIOGRAPHY

- Large G. W., J. C. McWilliams, and S. C. Doney, (1994): Oceanic with vertical mixing : A review layer and a model a non local boundary. *Rev. Geophys.*, 32, 363-403.
- Lozier M. S., S. F. Gary and A. S Bower, (2013): Simulated pathways of the overflow waters in the North Atlantic: Subpolar to subtropical export. *Deep Sea Res. Part II: Topical Studies in Oceanography*, 85:147–153.
- Lumpkin R. and K. Speer, (2007): Global Ocean Meridional Overturning. *J. Phys. Oceanogr.*, 37 (10): 2550–2562, doi:10.1175/JPO3130.1.
- Marshall J., A. Adcroft, C. Hill, L. Perelman, and C. Heisey, (1997): A finite-volume , incompressible Navier Stokes model for studies of the ocean on parallel computers. *J. Geophys. Res.* , 102, 5753-5766.
- Mauritzen C. and S. Häkkinen, (1999): On the relationship between dense water formation and the Meridional Overturning Cell in the North Atlantic Ocean. *Deep-Sea Research Part I: Oceanogr. Res. Papers*, 46(5): 877–894, doi:10.1016/S0967-0637(98)00094-6.
- McCarthy G. D., D. A. Smeed, W. E. Johns, E. Frajka-Williams, B. I. Moat, D. Rayner, M. O. Baringer, C. S. Meinen, J. Collins and H. L. Bryden, (2015): Measuring the Atlantic Meridional Overturning Circulation at 26°N. *Prog. in Ocean.* , 130: 91–111, doi:10.1016/j.pocean.2014.10.006.
- Mertens C., M. Rhein, M. Walter, C. Böning, E. Behrens, D. Kieke, R. Steinfeldt, and U. Stöber, (2014): Circulation and transports in the newfoundland basin, western subpolar North Atlantic. *J. Geophys. Res.: Oceans*, 7772–7793, doi:10.1002/2014JC010019.
- Myers P. G. and C. Donnelly, (2008): Water mass transformation and formation in the Labrador Sea, *J. of Climate*, 21: 1622–1638, doi:10.1175/2007JCLI1722.1.
- Mysak L. A., (1980): Topographically trapped waves. *Annu. Rev. Fluid Mech.*, 12, 45-76.
- Pearche M.,(2011): Coastal trapped wave generated by hurricane Andrew on the Texas-Louisiana shelf, master thesis, Texas A & M University.
- Pickart S. R, D. J. Torres, and P. S. Frantoni, (2005): The East Greenland Spill Jet. *J. of Geophys. Ocean.*, 35: 1037–1053, doi:10.1175/JPO2734.1. 6
- Rhein M., J. Fischer, W. M. Smethie, D. Smythe-Wright, R. F. Weiss, C. Mertens, D. H Min , U. Fleischmann and A. Putzka, (2002): Labrador seawater: pathways, CFC inventory and formation rates. *J. Phys. Oceanogr.*, 32 (2): 648–665.

- Rhein M., D. Kieke, S. Hüttl-Kabus, A. Roessler, C. Mertens, R. Meissner, B. Klein, C. W. Böning and I. Yashayaev, (2011): Deep-water formation, the subpolar gyre, and the meridional overturning circulation in the subpolar North Atlantic. *Deep-Sea Research Part II: Topical Studies in Oceanography*, 58(17-18): 1819–1832.
- Rhines P., S. Häkkinen, and S. A. Josey, (2008): Is Oceanic Heat Transport Significant in the Climate System? in book Arctic Subarctic Ocean Fluxes edited by Dickson. *Springer*, Chap:4, 87–109, doi:10.1007/978-1-4020-6774-7.
- Roessler A., M. Rhein, D. Kieke and C. Mertens, (2015): Long-term observations of North Atlantic Current transport at the gateway between western and eastern Atlantic. *J. Geophys. Res. : Oceans*, 120: 4003–4027, doi:10.1002/2014JC010662.
- Ross K C., (1981): Drift of satellite-tracked buoys on Flemish Cap, 1979-80. *NAFO Scientific Council Studies*, 1 (1): 47–50.
- Russell, J. L., K. W. Dixon, A. Gnanadesikan, R. J. Stouffer, and J. R. Toggweiler, (2006): The Southern hemisphere westerlies in a warming world: Propping open the door to the deep ocean. *Journal of Climate*, 19: 6382–6390, doi:10.1175/JCLI3984.1.
- Schneider L., D. Kieke, K. Jochumsen, E. Colbourne, I. Yashayaev, R. Steinfeldt, E. Varotsou, N. Serra, and M. Rhein, (2015): Variability of Labrador Sea Water transported through Flemish Pass during 1993-2013. *J. Geophys. Res. : Oceans*, 120: 5514–5533, doi:10.1002/2015JC010939.
- Scholz P., D. Kieke, G. Lohmann, M. Ionita and M. Rhein, (2014): Evaluation of Labrador Sea Water formation in a global Finite-Element Sea-Ice Ocean Model setup, based on a comparison with observational data. *J. of Geoph. Res. Oceans*, 119, 1644-1667, doi:10.1002/2013JC009232.
- Serra N., R. H Käse, A. Köhl, D. Stammer, and D. Quadfasel, (2010): On the low-frequency phase relation between the Denmark Strait and the Faroe-Bank Channel overflows, *Tellus A*, 62 (4): 530–550, doi:10.1111/j.1600-0870.2010.00445.x.
- Sigman D. M. and E. A. Boyle, (2000): Glacial/Interglacial Variations In Atmospheric Carbon Dioxide. *NATURE*, 407(6806): 859–869, doi:10.1038/35038000.
- Smith, T., Reynolds, R., Peterson, T., and Lawrimore, J, (2008): Improvements to noaa's historical merged land-ocean surface temperature analysis (1880–2006). *J. Climate*, 21: 22832296, 14.
- Stein M., (1996): Flemish Cap – A Review on Research Activities With Focus on Oceanographic Conditions, *NAFO Sci. Coun*, 25: 1–24.

BIBLIOGRAPHY

Stramma L., D. Kieke, M. Rhein, F. Schott, I. Yashayaev and K.P. Koltermann, (2004): Deep water changes at the western boundary of the subpolar North Atlantic during 1996 to 2001. *Deep-Sea Res. Part I: Oceanog. Res. Papers*, 51 (8): 1033–1056, 10.1016/j.dsr.2004.04.001.

Talley D. L., (2003): Shallow, Intermediate, and Deep Overturning Components of the Global Heat Budget. *J. Phys. Oceanogr.*, 33(3): 530–560

Thorpe R. B., J. M. Gregory, T. C. Johns, R. A. Wood, and J. F. B. Mitchell, (2001): Mechanisms determining the atlantic thermohaline circulation response to greenhouse gas forcing in a non-flux-adjusted coupled climate model. *J. of Climate*, 14(14): 3102–3116, doi:10.1175/1520-0442(2001)014;3102:MDTATC;2.0.CO;2.

Tomczak M., (1999): Some historical, theoretical and applied aspects of quantitative water mass analysis. *J. of Mar. Res.*, 27(2): 275–303.

Varotsos V. K., M. Tombrou, and C. Giannakopoulos, (2013): Statistical estimations of the number of future ozone exceedances due to climate change in Europe. *J. of Geophys. Res.: Atmospheres*, 118 (12): 6080–6099, doi:10.1002/jgrd.50451.

Varotsou E., K. Jochumsen , N. Serra , D. Kieke and L. Schneider, (2015): Interannual transport variability of Upper Labrador Sea Water at Flemish Cap. *J. of Geophys. Res.: Oceans*, 120: 5074–5089, doi:10.1002/2014JC010632.

Yashayaev I., N. Penny Holliday, M. Bersch, and H. M. van Aken, (2008): The history of the Labrador Sea water Production, Spreading, Transformation and Loss in book Arctic- Subarctic Ocean Fluxes edited by Dickson (2008). *Springer*, Chap: 24, 569–612, doi:10.1007/978-1-4020-6774-7.

Yashayaev I. and J. W. Loder , (2009): Enhanced production of Labrador Sea Water in 2008. *Geophys. Res. Lett.*, 36 (1), L01606, doi:10.1029/2008GL036162.

Yosuke I., Y. Kitade and M. Matsuyama, (2007): Characteristics of Coastal-Trapped Waves Induced by Typhoon along the Southeast Coast of Honshu, Japan. *J. of Oceanog.*, 63, 745–760.

Zhang J. and D. Rothrock, (2000): Modeling Arctic sea ice with an efficient plastic solution. *J. of Geophys. Res.*, 105, C2, 3325–3338.

Zhao, J., Y. Cao, and J. Shi , (2006): Core region of Arctic oscillation and the main atmospheric events impact on the Arctic. *Geophys. Res. Lett.*, 33, L22708, doi:10.1029/2006GL027590.

Zheng Y. and B. S Giese, (2009): Ocean heat transport in Simple Ocean Data Assimilation: Structure and mechanisms. *J. of Geophys. Res.*, 114 (C11), C11009, doi:10.1029/2008JC005190.